Developments in THz Polaritonics:
Towards Integrated Nonlinear THz Spectroscopy

by

Eric Rueyhao Sung

B.S. Chemistry (2017), Rice University

Submitted to the Department of Chemistry
in partial fulfillment of the requirements for the degree of

Doctor of Philosophy in Chemistry

at the

MASSACHUSETTS INSTITUTE OF TECHNOLOGY

February 2024

© 2024 Eric Rueyhao Sung. All rights reserved.

Author . . . .
Department of Chemistry
Jan. 12, 2024

Certified by. . . . .
Keith A. Nelson
Haslam and Dewey Professor of Chemistry
Thesis Supervisor

Accepted by . . . .
Adam P. Willard
Professor of Chemistry
Graduate Officer

This doctoral thesis has been examined by a Committee of the Department of Chemistry as follows:

Professor Moungi G. Bawendi . . . .
Chairman, Thesis Committee
Lester Wolfe Professor of Chemistry

Professor Keith A. Nelson . . . .
Thesis Supervisor
Haslam and Dewey Professor of Chemistry

Professor Gabriela S. Schlau-Cohen . . . .
Member, Thesis Committee
Associate Professor of Chemistry

Developments in THz Polaritonics:

Towards Integrated Nonlinear THz Spectroscopy

by

Eric Rueyhao Sung

Submitted to the Department of Chemistry
on Jan. 12, 2024, in partial fulfillment of the
requirements for the degree of
Doctor of Philosophy in Chemistry

Abstract

The terahertz (THz) polaritonics platform is a compact, waveguide-based platform for the generation, manipulation, and detection of THz waves. The platform uses thin ($<100\,\mu\mathrm{m}$) lithium niobate ($LiNbO_3$, LN) and lithium tantalate ($LiTaO_3$, LT) slabs, which can be patterned to control THz propagation. One of the unique features of the platform is that the THz fields can be imaged directly within the slab with subwavelength spatial resolution and subcycle temporal resolution. Both the amplitude and phase of the fields are recorded, which allows the full spatiotemporal evolution of the fields to be visualized. This makes the platform appealing for compact, waveguide-based THz experiments. The work in the thesis aims to develop tools to enable robust, compact THz spectroscopy using the polaritonics platform.

The first phase of my research aims to develop methods for enhanced THz generation in the waveguides. In a typical polaritonics experiment, the optical pump light is focused to a single line which launches THz fields with electric field strengths of approximately $10\,\mathrm{kV/cm}$. Although the fields are sufficiently strong for THz imaging, any nonlinear spectroscopic applications would require the use of much larger THz fields so that the much weaker THz transients that result from multiple interactions with the sample could be reliably detected. To this end, I developed two methods. The first method uses thin LN waveguides with a beveled edge for enhanced narrowband THz generation. The optical pump light is focused onto the bevel, after which it refracts and becomes confined within the waveguide by total internal reflection. This allows the pump beam to repeatedly drive the generated THz field during its multiple back-and-forth traversals within the LN slab. Using this method, we observe a 10-fold enhancement of the THz spectral amplitude at the velocity-matched frequency. The second method combines the tilted pulse front geometry with THz focusing to generate a strong THz field in the time domain. A circular stair-step "echelon" mirror is used to shape the pump pulse into a conical tilted pulse front composed of a series of concentric rings of pump light. When the pump rings are imaged onto a thin LT waveguide, coherent superposition of the focusing THz fields excited individually by each pump ring results in a dramatically enhanced THz field

at the focus. When optimized, the method generates THz fields with electric field strengths up to $175\,\mathrm{kV/cm}$, which is roughly $20\times$ larger than what is generated by a single line of pump light.

The second phase of my research focuses on methods for expanding the polaritonics toolset for spectroscopic applications. Previous experiments coupling the THz phonon-polaritons in a LN waveguide to the quasi-antiferromagnetic magnon mode in an adjacent slab of $ErFeO_3$ took advantage of the fact that both materials have similar refractive indices. Furthermore, the $ErFeO_3$ layer complicates THz imaging because it strongly absorbs the optical probe light. I investigated two experimental geometries to address these concerns. The first geometry uses a high-reflecting coating sandwiched between the LN slab and the sample material. The coating is designed to reflect the optical probe light, which enables THz imaging in LN by preventing the probe light from entering the sample and greatly expands the range of possible samples. The second geometry uses a slot waveguide to localize the THz field within a low-index slot region, which results in much stronger interactions between the THz fields and a sample inserted into the slot. Using this geometry, the linear THz absorption spectrum of a test sample was measured with good sensitivity and the complex dielectric function was recovered.

The work presented here describes methods for enabling robust integrated THz spectroscopy in the polaritonics platform. The methods, when combined, should also form the basis for future polaritonics experiments that interrogate the nonlinear THz responses of materials.

Thesis Supervisor: Keith A. Nelson
Title: Haslam and Dewey Professor of Chemistry

Acknowledgments

This thesis would never have been possible without the help and support of many people.

First are foremost, I want to thank my thesis advisor Prof. Keith Nelson. Keith has been an amazing mentor and role model throughout the course of my Ph.D. Through my many interactions with him, he showed me how to think critically and how to communicate scientific ideas precisely and clearly. He is patient and open-minded and is always willing to discuss anything from big ideas to the smallest experimental details. His infectious enthusiasm and optimism kept me motivated even when experiments hit a roadblock. Keith, thank you so much for your guidance and for believing in me!

I would also like to thank my thesis committee members, Prof. Moungi Bawendi and Prof. Gabriela Schlau-Cohen. They both gave me invaluable advice both about research and career development.

Throughout my many years in the Nelson Group, I have had the pleasure of working with many bright and talented people. When I joined the group, I worked with Dr. Andreas Steinbacher and Dr. Blake Dastrup. The two of them were key in helping me navigate the lab. Blake especially was a great help when I was learning about THz for the first time. He was always willing to bounce ideas around and discuss anything from basic optics to THz waveguides and more. Dr. Alex Maznev always asked insightful questions that deepened my understanding of my research. Nadia Berndt and Dr. David Rohrbach recently joined Team Polaritonics. They are bringing some really cool ideas to the subgroup and I look forward to seeing what they accomplish in the future. I also met many other talented Nelson Group members: Dr. David Veysset, Dr. Ievgeniia Chaban, Dr. Yun Kai, Dr. Leora Dresselhaus-Cooper, Dr. Yoseob (Joseph) Yoon, Dr. Doug Shin, Dr. Yaqing Zhang, Dr. Xian Li, Dr. Yu-Hsiang Cheng, Dr. Ryan Duncan, Dr. Dmitro Martynowych, Dr. Frank Gao, Dr. Jiaojian (Tristan) Shi, Dr. Yuchen Sun, Dr. Jet Lem, Jude Deschamps, Zhuquan Zhang, Zi-Jie (Jack) Liu, Peter Miedaner, Man Tou Wong, and Yu-Che (Ben) Chien.

Thank you to all of you for making the lab a fun, wonderful place to learn.

Thanks to Li Miao, the administrative assistant for the Nelson Group. Li was an never-ending source of logistical support for all things ranging from organizing meetings with my thesis committee to small things like helping me find the right sized box to mail something. Her advice saved me a lot of trouble numerous times.

Some of the work in this thesis would not have been possible without support from the staff at many lab facilities at MIT. Shaymus Hudson at the DMSE Metlab taught me how to polish and thin crystalline samples. Mark Belanger at the Edgerton Machine Shop helped make custom mounts for optics and sample preparation. The staff at MIT.nano (namely Kurt Broderick, Dennis Ward, Scott Poesse, Gary Riggott, Dave Terry, Bob Bicchieri, Donal Jamieson, and Mark Mondol) trained me on various nanofabrication techniques that were used to process the LN waveguides and helped troubleshoot any problems that arose.

Last but not least, I would like to thank my family for their undying love and support. My mother, Chin Fong Pau, and my father, Chung Shin Sung, were there through all of my successes and failures. My sisters, Angela and Cynthia, were always there to cheer me on. I dedicate this thesis to them.

To my family.

Contents

List of Figures

List of Tables

Chapter 1

Introduction

The terahertz (THz) region of the electromagnetic spectrum, loosely defined as the frequency range between 0.1-10 THz (vacuum wavelength $= 30\,\mu m$ to $3\,mm$), is home to a wide range of interesting physical phenomena. The vibrational and rotational transitions of many molecules and the collective modes (e.g. phonons, magnons, etc.) of solid state materials have frequencies in the few THz range, making it a good fingerprinting region [1–5]. THz radiation is also an appealing choice for non-invasive, non-destructive imaging applications because of its large penetration depth and non-ionizing nature [6–9].

Despite the rich physics and wide array of potential applications in the THz frequency range, the technologies operating at THz frequencies are immature compared to other portions of the electromagnetic spectrum. The lack of reliable THz sources and detectors, historically called the "THz gap," resulted from the fact that THz frequencies are too fast for conventional electronics (which typically operate at GHz or lower frequencies) and are two orders of magnitude slower than visible light frequencies which makes nonlinear optical processes generally inefficient. In the early years of THz spectroscopy, studies were restricted primarily to spectroscopy of simple gas molecules and crystals using thermal sources and detectors [10]. After many decades of technological advances, THz spectroscopy took on its modern form due to the development of the picosecond photoconductive switch (also called the Auston switch) as a THz source and detector [11]. This led to the development of THz time-domain
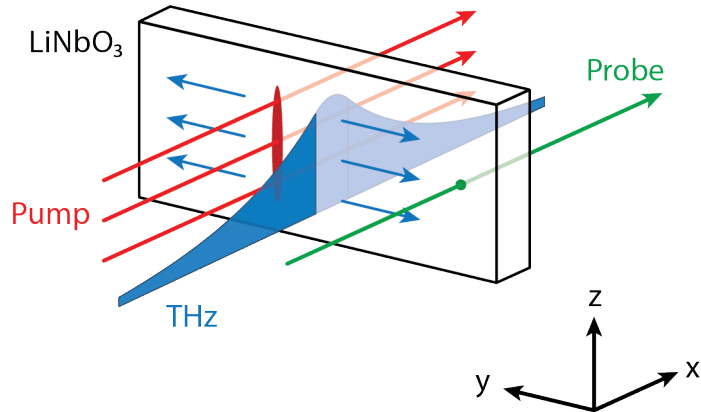
Figure 1-1: **Schematic illustration of the polaritonics platform.** A femtosecond pump pulse (shown in red) is focused into a thin LN crystal. The pump launches a THz wave (shown in blue), which propagates away from the excitation region. The THz wave is confined to the LN slab, but can interact with materials deposited on the slab surface through its evanescent field. A time-delayed probe pulse (shown in green) is focused into the slab to read out the time-dependent THz field directly inside the LN slab.

spectroscopy (THz-TDS) [12] which has proven to be a reliable method to extract amplitude and phase information of a THz field after interaction with a sample, yielding the real and imaginary components of the THz frequency-dependent refractive index of the sample. Around the same time, electro-optic crystals such as lithium niobate ($LiNbO_3$, LN) and lithium tantalate ($LiTaO_3$, LT) were shown to enable reliable THz generation through optical rectification [13, 14]. With the development of tilted-pulse front excitation in lithium niobate [15], THz field strengths in the 1-MV/cm range have been routinely generated [16, 17]. This has enabled many nonlinear spectroscopic studies in gases [18–20], liquids [21, 22], and solids [23–25]. Furthermore, the strong THz fields have been used for control over the states of condensed matter including recent examples of ferroelectric phase transitions [26, 27], magnetic domain reorientations [28, 29], and electronic/structural phase transitions [30].

The Nelson group has developed the THz polaritonics platform, shown in Fig. 1-1, in order to enable compact THz spectroscopy and photonics. The platform uses thin ($10\,\mu m$–$100\,\mu m$) LN and LT slab waveguides for the generation, manipulation, and

detection of THz fields. It is named in reference to the phonon-polaritons that are formed as a result of strong coupling between THz-frequency electromagnetic waves and the polar lattice vibrations in LN and LT [31]. THz fields are generated using a femtosecond laser pulse that is focused into the waveguide to launch THz waves that propagate away from the pumping region. Various strategies have been used to provide control over the THz waveform through the use of spatial and temporal shaping of the pump light [32–35]. An ultrafast optical pulse can be used to directly monitor the THz waveform within the slab with subwavelength spatial resolution and subcycle temporal resolution [36]. Because the thickness of the slab is comparable to the THz wavelength, the slab acts as a dielectric waveguide and modifies the dispersion of the THz waves. The THz waves can interact with structures integrated into the slab through chemically-assisted femtosecond laser machining [37, 38] or couple to structures deposited on a slab surface [39–42] through the evanescent field that extends outside of the slab. This allows studies of THz field interactions with photonic crystals [43–46], cavities [47–49], topological defects [46, 50], metamaterial structures [42, 51–53], and various other integrated photonics structures [39, 41, 53–56]. There has also been some success coupling the THz fields to samples deposited on top of the waveguide for spectroscopic applications [48, 57].

In this thesis, I discuss my work on expanding the polaritonics toolset. Although many successful polaritonics experiments have already been performed, further developments are needed for the platform to realize its full potential for integrated THz spectroscopy. One limitation is that the THz fields generated by a single line of pump light reach up to $10 \, \text{kV/cm}$ amplitudes [31]. Although these field strengths are sufficient for THz imaging, any nonlinear spectroscopic applications would require the use of much larger THz fields so that the much weaker THz transients that result from multiple field interactions with a sample could be reliably detected. Various pumping schemes have been proposed to increase the generated THz field strength [58, 59], but only modest improvements in the THz field strength have been achieved. Another major hurdle is that there are difficulties imaging the THz fields while they are coupled to a general sample. The simplest strategy would be to simply deposit

the sample of interest directly onto the waveguide. This approach was successful in coupling the THz fields in LN to the quasi-antiferromagnetic magnons in erbium orthoferrite (ErFeO$_3$). However, due to the strong absorption of visible light in ErFeO$_3$, imaging the THz fields within the waveguide suffered from a poor signal-to-noise ratio. Furthermore, it relied on the fact that LN and ErFeO$_3$ have similar THz refractive indices ($n \approx 5$ in both materials) so that the THz fields could easily penetrate into the ErFeO$_3$ slab [48]. In most other samples, there would be some refractive index mismatch that makes the coupling much weaker. The work presented in this thesis attempts to address these issues in order to enable robust linear spectroscopy of general samples in a compact waveguided geometry and potentially enable some compact nonlinear spectroscopic studies.

Chapter 2 introduces the classical electromagnetic theory for describing light-matter interactions. Starting from Maxwell's equations in the form of an eigenequation, the planewave solution is derived and a simple model for describing linear light-matter interactions is developed. Electric and magnetic field interactions are considered using simple toy models. The electric field interaction with charged particles is described using the damped driven harmonic oscillator model. The magnetic field interaction with spins is described using the Landau-Lifshitz-Gilbert equation. In both cases, the form for the susceptibility is derived. Lastly, two tools for computing approximate numerical solutions to Maxwell's equations are discussed. The first tool is perturbation theory which takes the solution for a simple, exactly-solvable geometry and extrapolates to a more complex geometry. The dielectric waveguides used in polaritonics are simple enough that the mode profiles and dispersion are easily solved analytically. Perturbation theory provides a simple way to quantitatively describe how the mode profiles and dispersion change upon perturbations to the waveguide or the surrounding cladding. It is also a useful tool for treating material absorption in the waveguides, since calculation of the mode profiles and dispersion typically only use the real part of the refractive index and neglect material absorption. The other tool is numerical simulation using the finite-difference time-domain (FDTD) method. This method propagates Maxwell's equations in the time domain so that the full

evolution of the THz fields can be calculated. This allows us to run simulations to optimize the experiments and gain insight into the various physical processes present in the system.

Chapter 3 focuses on the details of the polaritonics platform. The THz fields generated in LN and LT are not simply described as electromagnetic waves that propagate through the slab. Rather, they strongly couple to the polar lattice vibrations in the ferroelectric crystal to form phonon-polaritons. Furthermore, the polaritonics platform uses ferroelectric slabs with thicknesses comparable to the THz wavelength, so the slabs act like dielectric waveguides. The mode profiles and dispersion curves for both the transverse electric (TE) and transverse magnetic (TM) modes of the structure are calculated. THz generation occurs through the second-order nonlinear optical process called optical rectification. During this process, the THz fields are radiated from the nonlinear polarization in the ferroelectric crystal which follows the intensity profile of the optical pump beam, subject to bandwidth limitations that are discussed subsequently. For a femtosecond optical pump pulse, this excites a bandwidth of a few THz. THz detection takes advantage of the electro-optic properties of LN and LT, so an optical probe beam passing through the slab can be used to directly read out the fields within the slab. The electric field component of the phonon-polaritons modifies the local birefringence in the ferroelectric crystal which can be encoded as a change in polarization in a linearly polarized optical probe pulse. A spatially-expanded probe beam can be used to sample the THz fields over a large area with subwavelength spatial resolution and subcycle temporal resolution. Images of the THz fields can be captured using a charge-coupled device (CCD) camera to construct movies and directly visualize how the fields evolve over time.

In a typical polaritonics experiment, the optical pump beam is focused into a LN waveguide, generates a THz field, and leaves the waveguide. Because the interaction length is so small ($<100\,\mu m$), most of the pump light remains unused. Chapter 4 discusses enhanced narrowband THz generation using a beveled LN waveguide. The beveled edge allows an optical pump beam to refract and "bounce" back-and-forth within the slab while being confined by total internal reflection. This allows for a
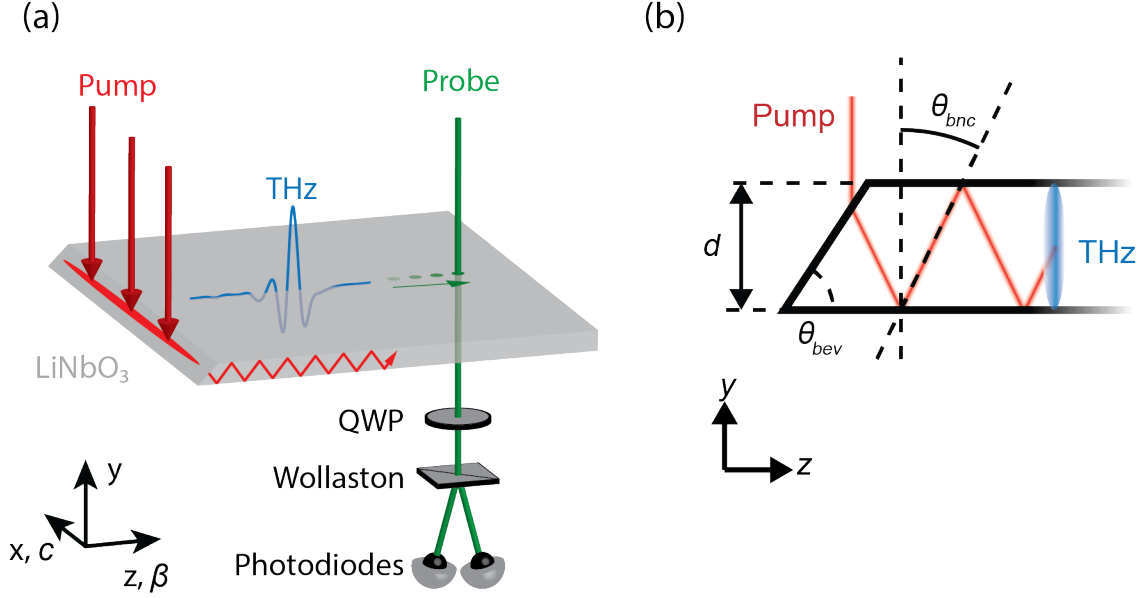
Figure 1-2: **Schematic illustration of THz generation using a beveled LN slab.** (a) The pump beam polarized along the LN c-axis enters the LN slab through the beveled edge. The pump beam refracts and "bounces" back-and-forth within the slab. The THz field is built up as the pump traverses the LN slab. A probe beam is used to read out the THz field amplitude, which is recorded using balanced photodiodes after passing through a quarter-wave plate (QWP) and Wollaston prism. (b) Schematic illustration of a beveled LN slab with thickness d. The beveled edge has angle θ_{bev}. Pump light (shown in red) enters through the bevel and refracts into the crystal at the "bounce" angle θ_{bnc}. The pump beam continually drives the THz field (shown in blue) as it propagates through the LN slab.

much longer interaction length for THz generation and allows the pump light to be used more efficiently. The optical pump travels laterally through the waveguide with the excited THz field and builds it up. When the lateral group velocity of the pump beam matches the THz phase velocity, we observe 10× enhancement of the peak THz spectral amplitude. Due to waveguide dispersion, the THz phase velocity has a moderate frequency dependence. Thus, the center frequency of the THz buildup can be selected by appropriate choice of the bevel angle. We perform FDTD simulations of the THz fields including several pump depletion mechanisms to determine what factors limit THz generation. These results suggest that beveled LN waveguides provide a relatively simple method for generating larger THz spectral amplitudes

(a) Input: Gaussian pulse

Circular echelon mirror

(b) Output: spatio-temporally shaped pulse

(c)

Pump rings

THz

LiTaO₃

x

z, c

y
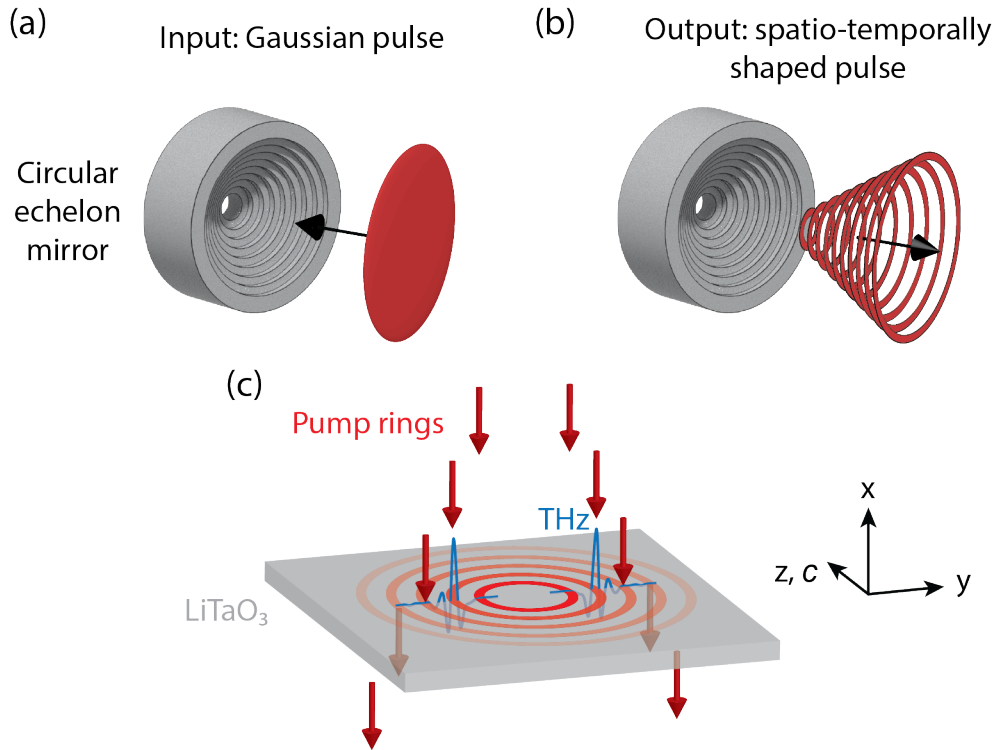
Figure 1-3: **Schematic illustration of the TREx scheme.** (a,b) The circular "echelon" mirror takes an input Gaussian pump pulse and shapes it into a discrete conical tilted pulse front made up of a series of concentric rings of pump light. (c) The pump rings are imaged onto a LT slab waveguide. The largest ring arrives first and excites a weak, focusing THz field. The later pump rings arrive at the LT slab in timed sequence and repeatedly drive the focusing THz field. This results in a dramatic increase in the THz field at the focus.

within the waveguide, which could be useful for integrated spectroscopic applications in cases where only a small THz bandwidth is needed.

Various strategies for enhanced THz generation have been demonstrated that do not rely on recycling the pump light. One method is the well-known tilted pulse front geometry commonly used for THz generation in bulk LN prisms [15]. Another method is to shape the pump light into a ring using a conical "axicon" lens, which launches THz fields in a focusing geometry [58]. Chapter 5 introduces the THz Ring Excitation (TREx) method, illustrated in Fig. 1-3, for generating strong THz fields in the time domain. The TREx method combines these two ideas by using a circular stair-step "echelon" mirror to shape the pump pulse into a series of concentric rings of pump light

25

which is imaged onto a thin LT waveguide. The pump rings arrive in timed sequence such that the weak THz field excited by the largest pump ring (which arrives first) is repeatedly driven by the subsequent pump rings as it focuses. When the lateral scan speed of the pump rings matches the THz phase velocity, the THz generation process is optimized and electric field strengths up to $175\,\mathrm{kV/cm}$ are observed at the focus. This represents a roughly 20-fold increase over the $10\,\mathrm{kV/cm}$ field strengths routinely generated by a single line of pump light and approaches the regime where materials begin to exhibit a nonlinear response. An interesting detail about the TREx method is that while the electric field components constructively interfere at the focus, the magnetic field components destructively interfere. This means that the strong THz electric field at the focus is accompanied by an extremely weak magnetic field, in contrast to the typical behavior of an electromagnetic wave where the electric and magnetic field components are always in phase with a ratio determined by the wave impedance. Constructive interference of the magnetic field, along with destructive interference of the electric field, could also be achieved by including a temporal delay between the two sides of the optical pump light equal to half of the THz period. This could have potential applications for selectively delivering a strong electric field or magnetic field to a sample without the use of field enhancement structures.

The last chapter of this thesis focuses on methods for expanding the polaritonics toolset for spectroscopic applications. Chapter 6 describes two experimental geometries for monitoring the THz fields as they interact with a sample. The first geometry, illustrated in Fig. 1-4a, uses a high-reflecting (HR) coating sandwiched between a thin LN slab and the sample material to enable THz imaging in cases where the sample would strongly absorb or scatter the probe light. The HR coating is designed to reflect the probe light so that it picks up the THz signal in LN without entering the sample region. Using this method, THz imaging is demonstrated in a hybrid waveguide slab made of LN and $ErFeO_3$. The avoided crossing at $0.67\,\mathrm{THz}$ in the polariton dispersion, indicating strong coupling between the THz phonon-polaritons in LN and the quasi-antiferromagnetic magnon mode in $ErFeO_3$, is reproduced [48]. The HR-coated LN slabs are also used to perform compact THz spectroscopy on the THz standard
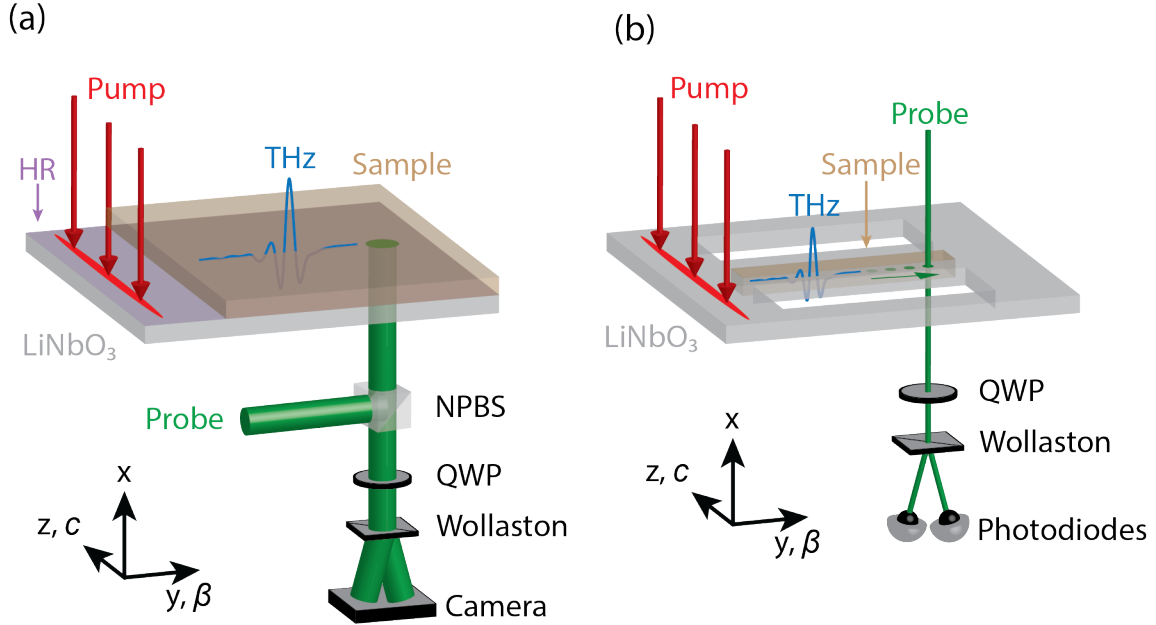
Figure 1-4: **Schematic illustrations of experimental geometries for coupling the waveguided THz fields to a sample.** (a) Schematic illustration of the reflective imaging geometry. Sample is deposited directly onto a thin LN slab. There is a dielectric high-reflecting (HR) coating between the LN and sample layers. Pump light is focused onto the LN, which launches a THz field that can penetrate through the HR coating and interact with the sample. An expanded probe beam enters the LN slab from the uncoated side, reflects off the HR coating, and exits the slab through the uncoated side. The probe beam passes through a non-polarizing beam splitter (NPBS), quarter-wave plate (QWP), and Wollaston prism and is recorded using a CCD camera. (b) Schematic illustration of the slot waveguide geometry. A pump beam is used to launch a THz field that propagates through the slot waveguide and interacts with a sample inserted into the slot. A probe beam is focused into one of the thin LN strips around the slot, and then passes through a quarter-wave plate (QWP) and Wollaston prism and the intensity is recorded using balanced photodiodes.

α-lactose monohydrate, which was deposited directly onto the HR coating. Although the sensitivity is poor, the technique is able to resolve the $0.53\,\mathrm{THz}$ absorption peak characteristic of lactose. This configuration enables experiments looking at the behavior of THz fields coupled to an adjacent material as they interact with structures integrated into the waveguide. The second experimental geometry, illustrated in Fig. 1-4b, uses a slot waveguide which is composed of two parallel strips of high-index material separated by a low-index slot. The slot waveguide is laser-machined into a LN planar waveguide, and a thin slab of sample is inserted into the slot. As the THz fields

travel through the slot waveguide, the structure localizes the electric field within the low-index slot region and dramatically increases the coupling to the sample. Using this technique, the absorption spectrum of the test sample α-lactose monohydrate was measured with good sensitivity and the complex dielectric function was recovered. This method opens up possibilities for waveguide-based THz spectroscopy with much better sensitivities than before.

The results of this work provide methods to enable robust integrated THz spectroscopy in the polaritonics platform. They open up possibilities for compact THz experiments, especially in cases where the sample is placed inside a specialized environment (e.g. inside an XFEL chamber or inside the bore of a cryomagnet) where accommodating a traditional free-space THz-TDS setup would be cumbersome. I hope that this work helps form the basis for future Nelson group members and others to routinely perform THz spectroscopy using thin LN waveguides and also provides a foundation for future work to enable waveguide-based nonlinear THz spectroscopy.

Chapter 2

Classical electromagnetic theory

One of the greatest advances in optics is the development of classical electromagnetism. In 1862, James Clerk Maxwell wrote a manuscript that contained what would eventually become Maxwell's equations, a set of partial differential equations that summarize the electromagnetic phenomena known at the time [60]. Among the various predictions that the equations made, one of the most striking at the time was that light is an electromagnetic wave that propagates with speed $c = 1/\sqrt{\epsilon_0 \mu_0}$, where ϵ_0 is the vacuum permittivity and μ_0 is the vacuum permeability. The calculated value agreed very well with previous experiments to determine the speed of light [61, 62], which solidified the idea that light is an electromagnetic wave. Since then, Maxwell's Equations continue to be very successful in describing the behaviors of electromagnetic systems and let us gain insight into the physical processes at play.

In this chapter, we use Maxwell's equations to develop a mathematical framework for describing electromagnetic radiation and derive a few basic properties. We also introduce simple models to describe the interactions of an electromagnetic wave with a point charge or a spin in order to develop a classical model for linear light-matter interactions. Finally, we describe two computational tools (perturbation theory and the finite-difference time-domain method) for obtaining approximate numerical solutions to Maxwell's equations.

2.1 Maxwell's equations

The modern form of Maxwell's equations, as formulated by Oliver Heaviside in 1912 [63], for describing the electric field $\mathbf{E}$ and magnetic field $\mathbf{H}$ in macroscopic media is given below

$$\nabla \cdot \mathbf{D} = \rho \tag{2.1}$$

$$\nabla \cdot \mathbf{B} = 0 \tag{2.2}$$

$$\nabla \times \mathbf{E} = -\frac{\partial \mathbf{B}}{\partial t} \tag{2.3}$$

$$\nabla \times \mathbf{H} = \frac{\partial \mathbf{D}}{\partial t} + \mathbf{J} \tag{2.4}$$

where ρ is charge density and $\mathbf{J}$ is current density. The constitutive relations for expressing the displacement field $\mathbf{D}$ and the magnetic field $\mathbf{B}$ in terms of $\mathbf{E}$ and $\mathbf{H}$ are given by

$$\mathbf{D} = \epsilon_0 \varepsilon \mathbf{E} \tag{2.5}$$

$$\mathbf{B} = \mu_0 \mu \mathbf{H} \tag{2.6}$$

where ϵ_0 and μ_0 are the electric permittivity and magnetic permeability, respectively, in a vacuum. ε and μ are the relative permittivity and permeability tensors that describe the material response to an electric or magnetic field, respectively. In general, ε and μ are described by the susceptibility tensors $\chi_{\mathrm{e,m}}$ by the following relationship.

$$\varepsilon = 1 + \chi_{\mathrm{e}} \tag{2.7}$$

$$\mu = 1 + \chi_{\mathrm{m}} \tag{2.8}$$

The form of $\chi_{\mathrm{e,m}}$ is determined by the equation of motion used to describe the light-matter interaction in a particular system.

2.2 Eigenproblem form of Maxwell's equations

To solve Maxwell's equations in the frequency domain, it is convenient to recast the equations as an eigenvalue problem in terms of electric field profile $|\mathbf{E}_n\rangle$ and the mode frequency ω_n. We assume that there are no free charges $\rho = 0$ nor currents $\mathbf{J} = \mathbf{0}$ and that the relative permittivity ε and relative permeability μ are time-independent. Starting with Faraday's law (Eq. 2.3), we take the curl of both sides and then substitute in Ampere's law (Eq. 2.4) to get the following second-order linear partial-differential equation.

$$\nabla \times \nabla \times |\mathbf{E}_n\rangle = -\epsilon_0 \mu_0 \varepsilon \mu \frac{\partial^2}{\partial t^2} |\mathbf{E}_n\rangle \tag{2.9}$$

From here on, we assume that any materials under consideration are nonmagnetic ($\mu = 1$), which is true for most materials. We also assume that $|\mathbf{E}_n\rangle$ is time-harmonic with frequency ω_n, so $\frac{\partial^2}{\partial t^2} |\mathbf{E}_n\rangle = \omega_n^2 |\mathbf{E}_n\rangle$. This gives us the eigenvalue equation

$$\nabla \times \nabla \times |\mathbf{E}_n\rangle = \left(\frac{\omega_n}{c}\right)^2 \varepsilon |\mathbf{E}_n\rangle \tag{2.10}$$

We have substituted in the vacuum speed of light $c = 1/\sqrt{\epsilon_0 \mu_0}$. To calculate the magnetic field profile $|\mathbf{H}_n\rangle$ from the $|\mathbf{E}_n\rangle$, we use Faraday's law (Eq. 2.3), which when written in the frequency domain is

$$|\mathbf{H}_n\rangle = -\frac{i}{\omega \mu_0 \mu} \nabla \times |\mathbf{E}_n\rangle \tag{2.11}$$

Alternatively, the eigenvalue problem could be formulated in terms of the magnetic field $|\mathbf{H}_n\rangle$ following a similar procedure. Doing so gives the eigenequation

$$\nabla \times \left(\frac{1}{\varepsilon} \nabla \times |\mathbf{H}_n\rangle\right) = \left(\frac{\omega}{c}\right)^2 |\mathbf{H}_n\rangle \tag{2.12}$$

The electric field profile $|\mathbf{E}_n\rangle$ could be extracted using Ampere's law (Eq. 2.4).

$$|\mathbf{E}_n\rangle = \frac{i}{\omega \epsilon_0 \varepsilon} \nabla \times |\mathbf{H}_n\rangle \tag{2.13}$$

For the rest of this thesis, we will choose Eq. 2.10 when using the eigenproblem form of Maxwell's equations. Here, we will assume that ε is diagonal for simplicity (i.e. all materials are either isotropic or have their principle axes aligned with the lab axes), which means that both ε and ε^{-1} are Hermitian. We can derive several basic properties of the eigenmodes and eigenvalues, following the proofs outlined in Ref. [64]. The first step is to show that the operator $\hat{\Theta} = \varepsilon^{-1}\nabla \times \nabla \times$ is Hermitian. This can be shown by taking two vectors $\mathbf{F}$ and $\mathbf{G}$ and showing that

$$\langle \mathbf{F}|\hat{\Theta}\mathbf{G}\rangle = \langle \hat{\Theta}\mathbf{F}|\mathbf{G}\rangle \tag{2.14}$$

is true. Using integration by parts and the vector identity

$$\nabla \cdot (\mathbf{A} \times \mathbf{B}) = (\nabla \times \mathbf{A}) \cdot \mathbf{B} - \mathbf{A} \cdot (\nabla \times \mathbf{B}) \tag{2.15}$$

the braket can be evaluated as follows.

$$
\begin{aligned}
\langle \mathbf{F}|\hat{\Theta}\mathbf{G}\rangle &= \int dV \ \mathbf{F}^* \cdot \varepsilon^{-1}\nabla \times \nabla \times \mathbf{G} \\
&= \int dV \ \varepsilon^{-1}\left[(\nabla \times \mathbf{F}^*) \cdot \nabla \times \mathbf{G} - \cancel{\nabla \cdot (\mathbf{F}^* \times \nabla \times \mathbf{G})}\right] \\
&= \int dV \ \varepsilon^{-1}\left[(\nabla \times \nabla \times \mathbf{F}^*) \cdot \mathbf{G} - \cancel{\nabla \cdot (\nabla \times \mathbf{F}^* \times \mathbf{G})}\right] \\
&= \langle \hat{\Theta}\mathbf{F}|\mathbf{G}\rangle
\end{aligned}
$$

We made use of the Divergence Theorem and assumed that the eigenmodes must decay to 0 when infinitely far away from the origin (which must be true for any bound mode) in order to cancel some of the terms. Because the operator $\hat{\Theta} = \varepsilon^{-1}\nabla \times \nabla$ is Hermitian, we expect the eigenvalues to be real-valued and the eigenmodes to form an orthonormal basis set. A brief proof of these properties is given below.

To show that the eigenvalues are real-valued, we return to Eq. 2.10. For an eigenmode $|\mathbf{E}_n\rangle$, it is trivial to show that

$$\left(\frac{\omega_n^2}{c^2}\right)^* \langle \mathbf{E}_n|\mathbf{E}_n\rangle = \langle \hat{\Theta}\mathbf{E}_n|\mathbf{E}_n\rangle = \langle \mathbf{E}_n|\hat{\Theta}\mathbf{E}_n\rangle = \left(\frac{\omega_n^2}{c^2}\right) \langle \mathbf{E}_n|\mathbf{E}_n\rangle \tag{2.16}$$

and therefore ω_n^2 is real-valued. Note that this is not sufficient to deduce that ω_n is real-valued because ω_n^2 could be negative. To show that ω_n^2 is positive semidefinite (and therefore ω_n is real), we evaluate the braket

$$
\begin{aligned}
\left(\frac{\omega_n}{c}\right)^2 \langle \mathbf{E}_n | \mathbf{E}_n \rangle = \langle \mathbf{E}_n | \hat{\Theta} \mathbf{E}_n \rangle &= \int dV \ \mathbf{E}_n^* \cdot \varepsilon^{-1} \nabla \times \nabla \times \mathbf{E}_n \\
&= \int dV \ \varepsilon^{-1} \left(\nabla \times \mathbf{E}_n^* \right) \cdot \left(\nabla \times \mathbf{E}_n \right) \\
&= \int dV \ \varepsilon^{-1} \left| \nabla \times \mathbf{E}_n \right|^2
\end{aligned}
$$

The integral is positive semidefinite given that ε^{-1} is positive semidefinite, which is true in most real systems. Therefore, ω_n^2 and ω_n are both real and positive semidefinite.

In order to show that the eigenmodes are orthogonal, we take two modes $|\mathbf{E}_n\rangle$ and $|\mathbf{E}_m\rangle$ and evaluate the braket

$$
\left(\frac{\omega_m}{c}\right)^2 \langle \mathbf{E}_m | \mathbf{E_n} \rangle = \langle \hat{\Theta} \mathbf{E}_m | \mathbf{E}_n \rangle = \langle \mathbf{E}_m | \hat{\Theta} \mathbf{E}_n \rangle = \left(\frac{\omega_n}{c}\right)^2 \langle \mathbf{E}_m | \mathbf{E_n} \rangle \tag{2.17}
$$

which gives us the condition

$$
\frac{\omega_m^2 - \omega_n^2}{c^2} \langle \mathbf{E}_m | \mathbf{E_n} \rangle = 0 \tag{2.18}
$$

This condition is only satisfied if the two modes are degenerate ($\omega_m = \omega_n$) or if the two modes are orthogonal ($\langle \mathbf{E}_m | \mathbf{E_n} \rangle = 0$). Note that degenerate modes are not guaranteed to be orthogonal. However, we can find linear combinations of the degenerate modes that are orthogonal using the Gram-Schmidt orthogonalization procedure.

To normalize the eigenmodes, we scale the amplitude of the eigenmodes so that the physical energy is equal to some unit value. The energy density u_n of the electromagnetic mode $|\mathbf{E}_n\rangle$ is given by

$$
u_n = \frac{1}{2} \epsilon_0 \varepsilon \left| \mathbf{E}_n \right|^2 \tag{2.19}
$$

so to normalize the mode, we require

$$\int dV \ \frac{1}{2}\epsilon_0\varepsilon \left|\mathbf{E}_n\right|^2 = 1\,\mathrm{J} \tag{2.20}$$

For propagating modes (e.g. in a waveguide), it is sometimes convenient to normalize by the power carried by the mode. The power flux density is given by the Poynting vector $\mathbf{S} = \mathbf{E} \times \mathbf{H}$ and the normalization condition is given by

$$\left|\int dV \ \mathbf{E} \times \mathbf{H}\right| = 1\,\mathrm{W} \tag{2.21}$$

2.2.1 Planewave solutions to Maxwell's equations

One of the main achievements of Maxwell's equations was the prediction of electromagnetic waves. Although the planewave solution in vacuum is treated in undergraduate textbooks, it is still instructive to reproduce the calculation here because the general conclusions are highly applicable to the work presented in this thesis. We can start from Eq. 2.9 (rewritten here for convenience)

$$\nabla \times \nabla \times \mathbf{E}\left(\mathbf{r}, t\right) = -\epsilon_0\mu_0 \frac{\partial^2}{\partial t^2}\mathbf{E}\left(\mathbf{r}, t\right)$$

Here we assume vacuum, so $\varepsilon = 1$ and $\mu = 1$. We apply the vector identity

$$\nabla \times \left(\nabla \times \mathbf{A}\right) = \nabla\left(\nabla \cdot \mathbf{A}\right) - \left(\nabla \cdot \nabla\right)\mathbf{A} \tag{2.22}$$

The first term on the right-hand side is 0 due to Gauss's law (Eq. 2.1). This allows us to rewrite Maxwell's equations in a form reminiscent of the wave equation.

$$\nabla^2\mathbf{E}\left(\mathbf{r}, t\right) - \epsilon_0\mu_0 \frac{\partial^2}{\partial t^2}\mathbf{E}\left(\mathbf{r}, t\right) = 0 \tag{2.23}$$

This equation has planewave solutions of the form

$$\mathbf{E}\left(\mathbf{r}, t\right) = E_0 \exp\left[i\left(\mathbf{k} \cdot \mathbf{r} \pm \omega t\right)\right]\hat{\mathbf{e}} \tag{2.24}$$

where E_0 is the electric field amplitude, $\hat{\mathbf{e}}$ is the electric polarization unit vector, $\mathbf{k}$ is the wavevector, and ω is the angular frequency. The polarization vector $\hat{\mathbf{e}}$ is perpendicular to $\mathbf{k}$ due to Gauss's law (Eq. 2.1). The wave speed c is given by

$$c = \frac{1}{\sqrt{\epsilon_0 \mu_0}} = \frac{\omega}{k} \tag{2.25}$$

The magnetic field accompanying the electric field can be calculated using Faraday's law (Eq. 2.11), which gives a solution of the form

$$\mathbf{H}(\mathbf{r}, t) = H_0 \exp\left[i\left(\mathbf{k} \cdot \mathbf{r} \pm \omega t\right)\right] \hat{\mathbf{h}} \tag{2.26}$$

The magnetic field polarization $\hat{\mathbf{h}}$ fulfills the relationship $\hat{\mathbf{e}} \times \hat{\mathbf{h}} = \hat{\mathbf{k}}$ (where $\hat{\mathbf{k}}$ is the unit vector along $\mathbf{k}$) and the magnetic field oscillates in phase with the electric field. The amplitude H_0 is given by the wave impedance Z defined as

$$Z \equiv \frac{E_0}{H_0} = \sqrt{\frac{\mu_0}{\epsilon_0}} = \mu_0 c \tag{2.27}$$

To include electric field interactions with a material, we define the electric polarization $\mathbf{P}(\mathbf{r}, t)$ which describes the electric dipole induced in the material. The polarization field is defined as

$$\mathbf{P}(\mathbf{r}, t) = \epsilon_0 \chi_e \mathbf{E}(\mathbf{r}, t) \tag{2.28}$$

For now we assume we only have a linear polarization response. The case where a nonlinear polarization is used to generate a THz field is treated in Section 3.3. Furthermore, we treat the electric susceptibility χ_e as a scalar for simplicity. $\mathbf{P}(\mathbf{r}, t)$ and $\mathbf{E}(\mathbf{r}, t)$ together make up the electric displacement field $\mathbf{D}(\mathbf{r}, t)$ through the constitutive relation

$$\mathbf{D}(\mathbf{r}, t) = \epsilon_0 \mathbf{E}(\mathbf{r}, t) + \mathbf{P}(\mathbf{r}, t) \tag{2.29}$$

This allows us to explicitly separate out $\mathbf{P}(\mathbf{r}, t)$ to give the driven wave equation

below.

$$\nabla^2 \mathbf{E}\left(\mathbf{r}, t\right) - \frac{1}{c^2} \frac{\partial^2}{\partial t^2} \mathbf{E}\left(\mathbf{r}, t\right) = \frac{1}{\epsilon_0 c^2} \frac{\partial^2}{\partial t^2} \mathbf{P}\left(\mathbf{r}, t\right) \tag{2.30}$$

The term on the right-hand side acts as a source term that generates a signal field $\mathbf{E}_{\mathrm{sig}}\left(\mathbf{r}, t\right)$. Assuming a polarization field $\mathbf{P}\left(\mathbf{r}, t\right) = \mathbf{P}_0\left(z, t\right) \exp\left[-i\left(kz - \omega t\right)\right]$, we get a signal field $\mathbf{E}_{\mathrm{sig}}\left(\mathbf{r}, t\right) = \mathbf{E}_{\mathrm{sig}}\left(z, t\right) \exp\left[-i\left(k_{\mathrm{sig}} z - \omega t\right)\right]$. Under the slowly-varying envelope approximation $\frac{\partial^2}{\partial z^2} \mathbf{E}_{\mathrm{sig}}\left(z, t\right) \ll ik \frac{\partial}{\partial z} \mathbf{E}_{\mathrm{sig}}\left(z, t\right)$, Eq. 2.30 becomes [65]

$$\frac{\partial}{\partial z} \mathbf{E}_{\mathrm{sig}}\left(z, t\right) = \frac{i\omega}{\epsilon_0 c} \mathbf{P}_0\left(z, t\right) \tag{2.31}$$

The signal field is emitted 90° out of phase of the polarization field. Using the damped driven harmonic oscillator model (with resonance frequency ω_0) described in Section 2.3.1 to model the polarization field, we can get a better idea of what happens when light interacts with a material. We consider the following three cases.

- If $\omega \ll \omega_0$, then $\mathbf{P}\left(z, t\right)$ oscillates in phase with the driving field and emits a signal field delayed by a quarter-cycle relative to the driving field. The net effect is that the phase velocity of the electric field is effectively decreased. Additionally if $\omega_0 \gg \Gamma$, the imaginary component of χ_{e} is negligibly small, so χ_{e} can be approximated as a positive real number.

- If $\omega \gg \omega_0$, then $\mathbf{P}\left(z, t\right)$ oscillates out of phase with the driving field and emits a signal field that leads the driving field by a quarter-cycle. The net effect is that the phase velocity of the electric field is effectively increased. Note that if ω is far higher than all resonance frequencies in a medium (e.g. x-rays), then this effect results in a phase velocity that is slightly faster than the vacuum speed of light.

- If $\omega = \omega_0$, then $\mathbf{P}\left(z, t\right)$ oscillates 90° out of phase of the driving field. The emitted signal field is 180° out of phase with the driving field, which results in the apparent decrease in field amplitude due to destructive interference. This is the classical description for linear absorption in a material.

For a mathematical description of the above phenomena, we can plug in the definition for the polarization field (Eq. 2.28) into Eq. 2.30 get the following equation.

$$\nabla^2 \mathbf{E}\left(\mathbf{r}, t\right) - \frac{\varepsilon}{c^2}\frac{\partial^2}{\partial t^2}\mathbf{E}\left(\mathbf{r}, t\right) = 0 \tag{2.32}$$

where $\varepsilon = 1 + \chi_{\mathrm{e}}$. The solution to this equation is the same planewave solution from before, but with the wave speed $v = c/\sqrt{\varepsilon}$. (A similar conclusion can be drawn for interactions with a magnetic field by introducing the magnetization $\mathbf{M}\left(\mathbf{r}, t\right) = \chi_{\mathrm{m}}\mathbf{H}\left(\mathbf{r}, t\right)$ and defining the relative permeability $\mu = 1 + \chi_{\mathrm{m}}$.) The wave speed is typically reported using the refractive index n, defined as $n = ck/\omega = \sqrt{\varepsilon\mu}$. Note that, in general, $n = n_{\mathrm{r}} + in_{\mathrm{i}}$ is complex-valued. The physical interpretation of the real and imaginary parts of n can be deduced directly from Eq. 2.24.

$$\begin{aligned}\mathbf{E}\left(z, t\right) &= E_0\hat{\mathbf{e}}\exp\left[i\left(kz - \omega t\right)\right] \\ &= E_0\hat{\mathbf{e}}\exp\left[i\left(\frac{n_{\mathrm{r}}\omega}{c}z - \omega t\right)\right]\exp\left(-\frac{n_{\mathrm{i}}\omega}{c}z\right)\end{aligned}$$

The real part n_{r} determines the wave speed $v = c/n_{\mathrm{r}}$. The imaginary part n_{i} describes how quickly the wave amplitude decreases. n_{i} is often converted to the absorption coefficient $\alpha = 4\pi n_{\mathrm{i}}/\lambda_0$, where λ_0 is the vacuum wavelength of the EM wave, which describes the attenuation rate of the wave intensity.

2.3   Linear light-matter interactions

Here, we describe toy models for light-matter interactions. We treat interactions with the electric field using the Drude-Lorentz oscillator model, which is typical for describing charges (e.g. electrons, atomic nuclei) in an approximately parabolic potential. For interactions with the magnetic field, we derive an approximate solution to the Landau-Lifshitz-Gilbert equation in order to determine the trajectory of a spin subject to a driving magnetic field.

2.3.1 Electric field interactions

The interaction between a charged particle and an electric field is described by a damped driven harmonic oscillator. The equation of motion for this system is as follows.

$$\frac{\partial^2}{\partial t^2}x\left(t\right) - \Gamma\frac{\partial}{\partial t}x\left(t\right) + \omega_0^2 x\left(t\right) = \frac{q}{m}E\left(t\right) \tag{2.33}$$

Here, $x\left(t\right)$ is the normalized displacement, ω_0 is the resonance (angular) frequency, Γ is a phenomenological damping constant, and q and m are the charge and reduced mass of the oscillator. Assuming a sinusoidal driving field at frequency ω, i.e. $E\left(t\right) = E_0\exp\left(i\omega t\right)$, and that the resulting displacement is also sinusoidal at the same frequency, i.e. $x\left(t\right) = x_0\exp\left(i\omega t\right)$, the steady-state solution can be found in the frequency domain to be

$$-\omega^2 x_0 - i\omega\Gamma x_0 + \omega_0^2 x_0 = \frac{q}{m}E_0 \tag{2.34}$$

From here, it is simple to determine the frequency-dependent response of the system due to the electric field. We define the electric susceptibility $\chi_{\rm e} \equiv x_0/E_0$. For a simple harmonic oscillator, this gives the familiar Lorentzian susceptibility

$$\chi_{\rm e}\left(\omega\right) = \frac{q}{m}\frac{1}{\omega_0^2 - \omega^2 - i\omega\Gamma} \tag{2.35}$$

In general, $\chi_{\rm e}$ is complex-valued. The modulus of $\chi_{\rm e}$ gives the amplitude of the response and the argument gives the phase difference between the response and the driving field, in this case ranging from 0 ($\omega \to 0$) to π ($\omega \to \infty$). When $\omega = \omega_0$, then $\chi_{\rm e}$ is purely imaginary.

Although we assumed that $\chi_{\rm e}$ is a scalar, in general $\chi_{\rm e}$ is a rank-2 tensor that couples a driving field with arbitrary polarization to motion along the x, y, and z axes. In addition, if the driving field couples to multiple independent oscillators, we can invoke the superposition principle to write $\chi_{\rm e}$ as the sum of the individual contributions from each oscillator. Using this, we can build up the susceptibility tensor for a material by considering interactions between the driving field and the

various degrees of freedom in the material.

2.3.2   Magnetic field interactions

The magnetic field interacts with a material typically by coupling to the spins in the lattice. The dynamics of a spin interacting with a magnetic field are described by the Landau-Lifshitz-Gilbert (LLG) equation [66–68]

$$\frac{\partial}{\partial t}\mathbf{S}\left(t\right) = -\frac{\gamma}{1+\alpha^2}\left[\mathbf{S}\left(t\right)\times\mathbf{B}_{\text{eff}}\left(t\right) + \frac{\alpha}{\left|\mathbf{S}\left(t\right)\right|}\mathbf{S}\left(t\right)\times\left[\mathbf{S}\left(t\right)\times\mathbf{B}_{\text{eff}}\left(t\right)\right]\right] \qquad (2.36)$$

where $\mathbf{S}\left(t\right)$ is a vector describing the spin orientation, $\mathbf{B}_{\text{eff}}\left(t\right)$ is the effective magnetic field experienced by the spin (including interactions with neighboring spins, static magnetic anisotropy, an external magnetic field, etc.), γ is the gyromagnetic ratio, and α is the small phenomenological Gilbert damping parameter ($\alpha \ll 1$). $\mathbf{B}_{\text{eff}}$ can be calculated from the spin Hamiltonian $\hat{\mathbf{H}}$ using the equation

$$\mathbf{B}_{\text{eff}} = -\frac{1}{\gamma}\frac{\partial}{\partial\mathbf{S}}\hat{\mathbf{H}} \qquad (2.37)$$

The linear susceptibility χ_{m} can be calculated by introducing a weak time-harmonic magnetic field $\mathbf{b}\left(t\right) = \left(b_x\hat{\mathbf{x}} + b_y\hat{\mathbf{y}} + b_z\hat{\mathbf{z}}\right)\exp\left(i\omega t\right)$ and solving for the resulting spin deflections from equilibrium $\delta S_{x,y,z} \propto \exp\left(i\omega t\right)$. Here, we will assume that $\mathbf{B}_{\text{eff}}$ is time-independent and oriented along the z-axis for simplicity, i.e. $\mathbf{B}_{\text{eff}} = B_0\hat{\mathbf{z}}$. After adding $\mathbf{b}\left(t\right)$ to $\mathbf{B}_{\text{eff}}$, the LLG equation in the frequency domain near equilibrium becomes (keeping only first-order terms)

$$\begin{aligned}
i\omega\delta S_x &= -\gamma'\left[\delta S_y B_0 - \left|\mathbf{S}\right|b_y - \alpha\left(-\delta S_x B_0 + \left|\mathbf{S}\right|b_x\right)\right]\\
i\omega\delta S_y &= -\gamma'\left[-\delta S_x B_0 + \left|\mathbf{S}\right|b_x + \alpha\left(\delta S_y B_0 - \left|\mathbf{S}\right|b_y\right)\right] \qquad (2.38)\\
i\omega\delta S_z &= 0
\end{aligned}$$

where we defined $\gamma' \equiv \gamma/\left(1+\alpha^2\right)$. Using a bit of algebra, it is straightforward to

decouple δS_x and δS_y to get the following equations.

$$\delta S_x = \gamma' \left| \mathbf{S} \right| \frac{\omega_0 + i\alpha\omega}{\omega_0^2 - \omega^2 + i\Gamma\omega} b_x - \gamma' \left| \mathbf{S} \right| \frac{\Gamma - i\omega}{\omega_0^2 - \omega^2 + i\Gamma\omega} b_y$$
$$\delta S_y = \gamma' \left| \mathbf{S} \right| \frac{\Gamma - i\omega}{\omega_0^2 - \omega^2 + i\Gamma\omega} b_x + \gamma' \left| \mathbf{S} \right| \frac{\omega_0 + i\alpha\omega}{\omega_0^2 - \omega^2 + i\Gamma\omega} b_y$$

$$(2.39)$$

where $\omega_0 = \gamma' B_0$ and $\Gamma = \alpha\gamma' B_0 = \alpha\omega_0$. This allows us to read off tensor elements of the magnetic susceptibility χ_{m}.

$$\chi_{\mathrm{m}} = \begin{bmatrix} \chi_\perp & i\eta & 0 \\ -i\eta & \chi_\perp & 0 \\ 0 & 0 & 0 \end{bmatrix} \tag{2.40}$$

where $\chi_\perp$ and η are given by

$$\chi_\perp = \gamma' \left| \mathbf{S} \right| \frac{\omega_0 + i\alpha\omega}{\omega_0^2 - \omega^2 + i\Gamma\omega}$$
$$\eta = \gamma' \left| \mathbf{S} \right| \frac{\omega + i\Gamma}{\omega_0^2 - \omega^2 + i\Gamma\omega}$$

$$(2.41)$$

This is the linear susceptibility tensor for the gyrotropic saturated dipole model. Note the strong resemblance to the harmonic oscillator model. As a crude approximation, the gyrotropic saturated dipole model can be thought of as two coupled harmonic oscillators along perpendicular axes where motion along one axis drives motion along the other.

2.4 Perturbation theory

Perturbation theory is a powerful tool that generates approximate solutions to complex problems by extrapolating from the exact solution to a similar, much simpler problem. The technique was first applied to celestial mechanics where it was used to provide approximate solutions to the three-body problem [69]. The prototypical example is the Sun-Earth-Moon system, where the exactly solvable problem is the Sun-Earth two-body problem and the Moon is treated the third body that perturbs

the orbit of the Earth (hence the name "perturbation" theory). Since then, it has been applied to quantum mechanics [70] as well as many other fields of study [71].

Perturbation theory, when applied to Maxwell's equations, is a powerful tool to investigate how a small change $\delta\varepsilon$ added to the dielectric map ε results in changes to an electromagnetic mode $|\mathbf{E}_n\rangle$ and its frequency ω_n. To calculate the first-order corrections, we start from Eq. 2.10 and include a perturbation to the electric permittivity, i.e. $\varepsilon \to \varepsilon + \delta\varepsilon$. We also expand the eigenmode $|\mathbf{E}_n\rangle \to |\mathbf{E}_n^{(0)}\rangle + |\mathbf{E}_n^{(1)}\rangle$ and frequency $\omega_n \to \omega_n^{(0)} + \omega_n^{(1)}$. In the notation used here, the superscript $^{(0)}$ denotes the unperturbed value and $^{(1)}$ denotes the first-order correction. Inserting these into Eq. 2.10 gives

$$\nabla \times \nabla \times \left(|\mathbf{E}_n^{(0)}\rangle + |\mathbf{E}_n^{(1)}\rangle\right) = \left(\frac{\omega_n^{(0)} + \omega_n^{(1)}}{c}\right)^2 (\varepsilon + \delta\varepsilon)\left(|\mathbf{E}_n^{(0)}\rangle + |\mathbf{E}_n^{(1)}\rangle\right) \tag{2.42}$$

Collecting the first-order terms gives the following equation.

$$\nabla \times \nabla \times |\mathbf{E}_n^{(1)}\rangle = \frac{2\omega_n^{(0)}\omega_n^{(1)}}{c^2}\varepsilon\,|\mathbf{E}_n^{(0)}\rangle + \left(\frac{\omega_n^{(0)}}{c}\right)^2 \delta\varepsilon\,|\mathbf{E}_n^{(0)}\rangle + \left(\frac{\omega_n^{(0)}}{c}\right)^2 \varepsilon\,|\mathbf{E}_n^{(1)}\rangle \tag{2.43}$$

To solve for $\omega_n^{(1)}$, we left-multiply by $\langle\mathbf{E}_n^{(0)}|$ and assume quasinormalization $\langle\mathbf{E}_n|\varepsilon|\mathbf{E}_n^{(0)}\rangle = 1 \to \langle\mathbf{E}_n^{(1)}|\varepsilon|\mathbf{E}_n^{(0)}\rangle = 0$. This gives us

$$\omega_n^{(1)} = -\frac{\omega_n^{(0)}}{2}\frac{\langle\mathbf{E}_n^{(0)}|\delta\varepsilon|\mathbf{E}_n^{(0)}\rangle}{\langle\mathbf{E}_n^{(0)}|\varepsilon|\mathbf{E}_n^{(0)}\rangle} \tag{2.44}$$

Note that contributions to the braket $\langle\mathbf{E}_n^{(0)}|\delta\varepsilon|\mathbf{E}_n^{(0)}\rangle$ are only nonzero within the perturbed volume V_{pert}. Assuming that both $\delta\varepsilon$ and ε can be treated as scalars within V_{pert}, we can rewrite $\omega_n^{(1)}$ as

$$\omega_n^{(1)} = -\frac{\omega_n^{(0)}}{2}\frac{\delta\varepsilon}{\varepsilon}f \tag{2.45}$$

where the fill fraction f is defined as

$$f = \frac{\langle\mathbf{E}_n^{(0)}|\varepsilon|\mathbf{E}_n^{(0)}\rangle_{V_{\text{pert}}}}{\langle\mathbf{E}_n^{(0)}|\varepsilon|\mathbf{E}_n^{(0)}\rangle_V} \tag{2.46}$$

The subscripts denote integration over all space (V) or over the perturbed region only (V_{pert}). Physically, f represents the fraction of the mode's integrated electric energy density that is contained within the perturbed region. This equation predicts several intuitive behaviors. If the permittivity is increased ($\delta\varepsilon > 0$), then the mode frequency decreases. The relative change in frequency is proportional to the relative change in permittivity, i.e. $\omega_n^{(1)}/\omega_n^{(0)} \propto \delta\varepsilon/\varepsilon$. In addition, a larger fill fraction corresponds to a larger shift in frequency. Note that while ε must be Hermitian, $\delta\varepsilon$ does not have the same requirement. Thus, one could use an imaginary-valued perturbation to calculate an imaginary-valued frequency shift which would correspond to attenuation ($\text{Im}\,(\delta\varepsilon) > 0$) or gain ($\text{Im}\,(\delta\varepsilon) < 0$). Perturbation theory is also useful for calculating the effect of weak nonlinearities such as a Kerr nonlinearity where $\delta\varepsilon \propto \mathbf{E}^2$ [64].

It is sometimes convenient to convert $\omega_n^{(1)}$ to a shift in wavevector $k_n^{(1)}$. By Taylor expanding k_n about $\omega = \omega_n^{(0)}$, it is simple to relate $k_n^{(1)}$ to $\omega_n^{(1)}$ using

$$k_n^{(1)} = -\frac{\partial k}{\partial \omega}\omega_n^{(1)} \tag{2.47}$$

This equation holds for both real and imaginary $\omega_n^{(1)}$ due to the Cauchy-Riemann equations. Note the minus sign, which appears because a decrease in frequency corresponds to an increase in wavevector. Recalling that the group velocity $v_{\text{gr}} = \partial\omega/\partial k$, we get the equation for $k_n^{(1)}$.

$$k_n^{(1)} = -\frac{1}{v_{\text{gr}}}\omega_n^{(1)} = \frac{\omega_n^{(0)}}{2v_{\text{gr}}}\frac{\delta\varepsilon}{\varepsilon}f \tag{2.48}$$

Note that unperturbed value for v_{gr} should be used for this calculation.

Assuming that $\delta\varepsilon$ is imaginary-valued and that ε is real-valued, Eq. 2.48 gives the rate of amplitude attenuation of an electromagnetic wave propagating through a structure with permittivity map ε. This can be converted to an effective absorption coefficient α_n of an electromagnetic wave propagating through a structure.

$$\alpha_n = 2k_n^{(1)} = \frac{\omega_n^{(0)}}{v_{\text{gr}}}\frac{\delta\varepsilon}{\varepsilon}f \tag{2.49}$$

The extra factor of 2 comes from the fact that $k_n^{(1)}$ describes how quickly the amplitude of the wave decays while α_n describes how quickly the intensity (which is proportional to the amplitude squared) decays.

We can recover the usual definition for the absorption coefficient in a bulk material with permittivity $\varepsilon_r + i\varepsilon_i$ using the perturbative solution. In the weak absorption limit, we can set $\varepsilon = \varepsilon_r \approx n_r^2$ and $\delta\varepsilon = \varepsilon_i \approx 2n_r n_i$. Also, because the we are treating ε_i as the perturbation, we can treat ε as a real constant in order to satisfy the Kramers-Kronig relations. Therefore, the unperturbed v_{gr} is equal to $v_{ph} = c/n_r$. Using these approximations, we get the following equation.

$$\alpha = \frac{4\pi n_i}{\lambda_0} \tag{2.50}$$

where $\lambda_0 = 2\pi c/\omega$ is the vacuum wavelength of the electromagnetic wave.

To solve for $|\mathbf{E}_n^{(1)}\rangle$, we return to Eq. 2.43 and left-multiply by $\langle\mathbf{E}_m^{(0)}|$ and invoke the orthonormal property of the modes $\langle\mathbf{E}_m^{(0)}|\varepsilon|\mathbf{E}_n^{(0)}\rangle = \delta_{mn}$.

$$\langle\mathbf{E}_m^{(0)}|\varepsilon|\mathbf{E}_n^{(1)}\rangle = \frac{\langle\mathbf{E}_m^{(0)}|\delta\varepsilon|\mathbf{E}_n^{(0)}\rangle}{\left(\dfrac{\omega_m^{(0)}}{\omega_n^{(0)}}\right)^2 - 1} \tag{2.51}$$

This equation shows that the mode $|\mathbf{E}_n^{(0)}\rangle$ mixes with the other modes $|\mathbf{E}_m^{(0)}\rangle$ and that the magnitude of the mixing is determined by the overlap between the modes mediated by the perturbation as well as the relative frequencies (stronger mixing occurs when the frequencies are closer together).

Qualitatively, the mathematics and results described here are very similar to those derived for quantum mechanics [64, 72]. However, there is one important difference. While the wavefunctions used in quantum mechanics are complex-valued, the electric and magnetic fields used in electromagnetic theory are classical fields so they must be real-valued. This results in some interesting behavior when using imaginary-valued perturbations. Consider Eq. 2.51. Given an imaginary-valued perturbation and that the eigenmodes are real-valued, the left-hand side evaluates to a real number while

the right-hand side evaluates to an imaginary number. The only way that this could be true is if both sides equal 0, so to first order an imaginary-valued perturbation does not affect the mode profile $|\mathbf{E}_n\rangle$. This makes intuitive sense because $|\mathbf{E}_n\rangle$ should be determined by the real part of the refractive index map $n = \sqrt{\varepsilon}$. Writing out n_r in terms of ε_r and ε_i gives the equation (assuming $\varepsilon_i < \varepsilon_r$).

$$n_r = \sqrt{\varepsilon_r} \left[1 + \frac{1}{8} \left(\frac{\varepsilon_i}{\varepsilon_r} \right)^2 + O\left(\left(\frac{\varepsilon_i}{\varepsilon_r} \right)^4 \right) \right] \qquad (2.52)$$

Note that the lowest order term in $\varepsilon_i/\varepsilon_r$ is quadratic. This agrees with our previous conclusion that to first oder $|\mathbf{E}_n\rangle$ is unaffected by an imaginary-valued perturbation.

2.5 Finite-difference time-domain schemes

In most geometries, Maxwell's equations cannot be solved analytically. However, very good approximate solutions can be found using numerical methods. A common approach is to propagate Maxwell's equations in the time domain using a finite-difference scheme. The simulation space is discretized on a Yee cell [73], shown in Fig. 2-1, and stepped through time. We approximate the partial derivatives in Eq. 2.3 and 2.4 using finite differences. For a function $f(x)$, the first derivative at $x = x_0$ can by approximated by Taylor expanding the function about two nearby points $x = x_0 \pm \Delta x/2$.

$$f\left(x_0 \pm \frac{\Delta x}{2} \right) = f(x_0) \pm f'(x_0) \left(\frac{\Delta x}{2} \right) + \frac{1}{2} f''(x_0) \left(\frac{\Delta x}{2} \right)^2 + \mathcal{O}\left(\Delta x^3 \right) \qquad (2.53)$$

Taking the difference $f(x_0 + \Delta x/2) - f(x_0 - \Delta x/2)$ and isolating $f'(x_0)$ gives the following equation.

$$f'(x_0) = \frac{f(x_0 + \Delta x/2) - f(x_0 - \Delta x/2)}{\Delta x} + \mathcal{O}\left(\Delta x^3 \right) \qquad (2.54)$$

This equation gives accuracy up to second order, which is usually sufficient for an electromagnetic simulation. If higher-order accuracy is needed, the appropriate finite
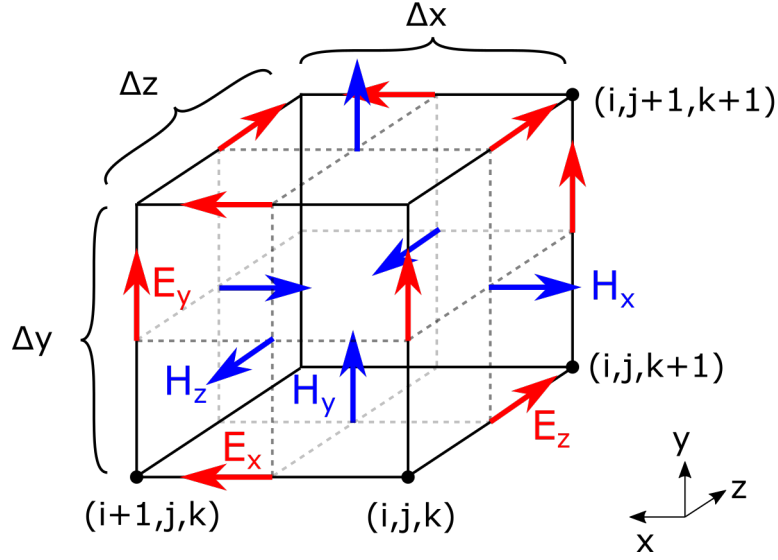
Figure 2-1: **Diagram of the Yee cell.** The simulation space is discretized into voxels with dimensions $\Delta x \times \Delta y \times \Delta z$. The electric field components (red) are placed on the edges of the unit cell while the magnetic field components (blue) are centered on the faces of the unit cell.

difference equation can easily be derived by including more nearby points in the calculation.

We use a leapfrog scheme to step the fields through time, alternating between updating $\mathbf{E}(t)$ at each time n and $\mathbf{H}(t)$ at each time $n + 1/2$. Applying the finite-differencing scheme to Eq. 2.3 and 2.4, we get update equations

$$
\begin{aligned}
E_x^{n+1}\left(i + \frac{1}{2}, j, k\right) = {} & E_x^n\left(i + \frac{1}{2}, j, k\right) \\
& + \frac{\Delta t}{\epsilon_0 \varepsilon}\left[\frac{H_z^{n+1/2}\left(i + \frac{1}{2}, j + \frac{1}{2}, k\right) - H_z^{n+1/2}\left(i + \frac{1}{2}, j - \frac{1}{2}, k\right)}{\Delta y}\right. \\
& \left. - \frac{H_y^{n+1/2}\left(i + \frac{1}{2}, j, k + \frac{1}{2}\right) - H_y^{n+1/2}\left(i + \frac{1}{2}, j, k - \frac{1}{2}\right)}{\Delta z}\right] \\
& + J_x^n\left(i + \frac{1}{2}, j, k\right)
\end{aligned}
$$

$$(2.55)$$

$$H_x^{n+1/2}\left(i, j+\frac{1}{2}, k+\frac{1}{2}\right) = H_x^{n-1/2}\left(i, j+\frac{1}{2}, k+\frac{1}{2}\right)$$
$$-\frac{\Delta t}{\mu_0 \mu}\left[\frac{E_z^n\left(i, j+1, k+\frac{1}{2}\right) - E_z^n\left(i, j, k+\frac{1}{2}\right)}{\Delta y}\right.$$
$$\left. -\frac{E_y^n\left(i, j+\frac{1}{2}, k+1\right) - E_y^n\left(i, j+\frac{1}{2}, k\right)}{\Delta z}\right] \tag{2.56}$$

plus cyclic permutations. In the notation used here, the superscript on the field variable denotes the time index, the subscript denotes the field component, and the indices within parenthesis denote spatial indices. Δx, Δy, and Δz are the grid spacings along the x, y, and z axes, respectively, and Δt is the time step. For simplicity, we will assume that the grid spacing is the same in all directions, i.e. $\Delta x = \Delta y = \Delta z$. For the simulation to be numerically stable, over the entire simulation space Δt must fulfill the Courant-Friedrichs-Lewy condition [74]

$$\frac{c}{\sqrt{\varepsilon \mu}}\Delta t \leq \Delta x \tag{2.57}$$

where c is the vacuum speed of light. In addition, Δx must be small enough to resolve the smallest wavelength λ in the simulation. A general rule of thumb is that at least 10 voxels/wavelength should be used.

$$\Delta x \leq \frac{\lambda}{10} \tag{2.58}$$

In order to include the material response, we follow a similar methodology as was done in Section 2.2.1. We introduce the polarization field $\mathbf{P}(t)$ and magnetization field $\mathbf{M}(t)$ and propagate them together with $\mathbf{E}(t)$ and $\mathbf{H}(t)$. These fields are updated according to their own equations of motion, determined by the model used for the light-matter interactions. For $\mathbf{P}(t)$, typically the damped driven oscillator model (Eq. 2.33) is used. For the equation of motion

$$\frac{\partial^2}{\partial t^2}\mathbf{P}(t) + \Gamma\frac{\partial}{\partial t}\mathbf{P}(t) + \omega_0^2\mathbf{P}(t) = \sigma\omega_0^2\mathbf{E} \tag{2.59}$$

46

the corresponding update equations are

$$\mathbf{P}^{n+1} = \mathbf{P}^n + \Delta t \dot{\mathbf{P}}^n \tag{2.60}$$

$$\dot{\mathbf{P}}^{n+1} = (1 - \Gamma \Delta t) \dot{\mathbf{P}}^n - \omega_0^2 \Delta t \left(\mathbf{P}^n - \sigma \mathbf{E}^n \right) \tag{2.61}$$

where $\dot{\mathbf{P}} = \partial \mathbf{P} / \partial t$, ω_0 is the resonance frequency, Γ is a phenomenological damping parameter, and σ is the oscillator strength. Both $\mathbf{P}$ and $\dot{\mathbf{P}}$ have the same spatial discretization as $\mathbf{E}$ and get updated simultaneously with $\mathbf{E}$. The polarization couples back into Ampere's law (Eq. 2.4) by generating a polarization current $\mathbf{J}_\mathrm{P}$ given by

$$\mathbf{J}_\mathrm{P} = \frac{\partial}{\partial t} \mathbf{P} \tag{2.62}$$

For $\mathbf{M}(t)$ the Landau-Lifshitz-Gilbert (LLG) equation is typically used to model the magnetic field interactions with atomic spins. The LLG equation is given by

$$\frac{\partial}{\partial t} \mathbf{M}(t) = -\frac{\gamma}{1 + \alpha^2} \left[\mathbf{M}(t) \times \mathbf{B}_\mathrm{eff}(t) + \frac{\alpha}{|\mathbf{M}(t)|} \mathbf{M}(t) \times [\mathbf{M}(t) \times \mathbf{B}_\mathrm{eff}(t)] \right] \tag{2.63}$$

where $\mathbf{B}_\mathrm{eff}$ is the effective magnetic field experienced by the magnetic moments. $\mathbf{B}_\mathrm{eff}$ can be calculated from the magnetic dipole Hamiltonian $\hat{\mathbf{H}}$ using the equation

$$\mathbf{B}_\mathrm{eff} = -\frac{1}{V_\mathrm{M}} \frac{\partial}{\partial \mathbf{M}} \hat{\mathbf{H}} \tag{2.64}$$

where V_M is the volume of the magnetic unit cell. A common strategy for solving the LLG equation is to apply a finite-difference scheme and propagate it in the time domain. However, this approach requires a very fine time step $\Delta t \leq \gamma' B_\mathrm{eff} / 100$ for the scheme to converge properly, which drastically increases the computational cost of a multiphysics simulation where the LLG equation is coupled to Maxwell's equations. Alternatively, we can derive an approximate closed-form solution to the LLG equation using perturbation theory for propagating in the time domain. We take inspiration from the variation of parameters procedure commonly used in Celestial mechanics for calculating the planetary orbits [75, 76]: First, calculate the Kepler

orbit for an idealized system. Then, determine how a small perturbation modifies the trajectory. Lastly, propagate the system through time using the modified trajectory while updating the parameters during every time step. For the LLG equation, we solve for the trajectory of $\mathbf{M}(t)$ assuming a time-independent magnetic field $\mathbf{B}_{\text{eff}}$ and treat the damping as the perturbation ($\alpha \ll 1$). To find the trajectory for a general system, we propagate the solution using a time-independent magnetic field and update $\mathbf{B}_{\text{eff}}$ at every time step.

To solve the unperturbed case, we set $\alpha = 0$. Without loss of generality, we define our coordinate axes so that $\mathbf{B}_{\text{eff}}$ is aligned along the z-axis, i.e. $\mathbf{B}_{\text{eff}} = B_0 \hat{z}$. To 0th order, the equation of motion becomes

$$\frac{\partial}{\partial t}\mathbf{M}(t) = -\gamma B_0 \mathbf{M}(t) \times \hat{z} \tag{2.65}$$

The solution to this set of coupled differential equations is given by

$$
\begin{aligned}
M_x(t) &= M_r \cos(\omega_0 t + \phi) \\
M_y(t) &= M_r \sin(\omega_0 t + \phi) \\
M_z(t) &= \sqrt{|\mathbf{M}|^2 - M_r^2}
\end{aligned}
\tag{2.66}
$$

These equations describe spin precession about the z-axis at angular frequency $\omega_0 = \gamma B_0$. ϕ is a phase constant determined by the initial conditions.

Now we include the perturbation $\alpha \ll 1$, substitute $\gamma/(1 + \alpha^2) \to \gamma'$, and solve the equation of motion to 1st order. Evaluating the cross-products, Eq. 2.63 becomes

$$
\begin{aligned}
\frac{\partial}{\partial t}M_x(t) &= -\gamma' B_0 \left[M_y(t) - \frac{\alpha M_z(t)}{|\mathbf{M}|}M_x(t) \right] \\
\frac{\partial}{\partial t}M_y(t) &= -\gamma' B_0 \left[-M_x(t) + \frac{\alpha M_z(t)}{|\mathbf{M}|}M_y(t) \right] \\
\frac{\partial}{\partial t}M_z(t) &= \gamma' B_0 \frac{\alpha}{|\mathbf{M}|} \left[M_x^2(t) + M_y^2(t) \right]
\end{aligned}
\tag{2.67}
$$

We take the 0th order solution given in Eq. 2.66 and plug into the equation of motion

48

given by Eq. 2.63. For $M_x(t)$ and $M_y(t)$, we get the matrix equation

$$\frac{\partial}{\partial t}\begin{bmatrix} M_x(t) \\ M_y(t) \end{bmatrix} = \gamma' B_0 \begin{bmatrix} \dfrac{\alpha M_z}{|\mathbf{M}|} & -1 \\ 1 & -\dfrac{\alpha M_z}{|\mathbf{M}|} \end{bmatrix} \begin{bmatrix} M_x(t) \\ M_y(t) \end{bmatrix} \tag{2.68}$$

It is straightforward to show that unperturbed solutions for $M_x(t)$ and $M_y(t)$ satisfy this matrix equation with eigenfrequency ω_0 given by

$$\omega_0 = \gamma' B_0 \sqrt{1 - \left(\frac{\alpha M_z}{|\mathbf{M}|}\right)^2} \approx \gamma' B_0 \left[1 - \frac{1}{2}\left(\frac{\alpha M_z}{|\mathbf{M}|}\right)^2\right] \tag{2.69}$$

Plugging the solutions for $M_x(t)$ and $M_y(t)$ into the equation for $M_z(t)$, we get the equation

$$\frac{\partial}{\partial t} M_z(t) = \gamma' B_0 \frac{\alpha}{|\mathbf{M}|}\left[|\mathbf{M}|^2 - M_z^2(t)\right] \tag{2.70}$$

which has the solution

$$M_z(t) = -|\mathbf{M}|\tanh(\alpha\gamma' B_0 t + c) \tag{2.71}$$

where c is a constant determined by the initial conditions. This also gives the time-dependence for the amplitude for oscillations in the xy-plane.

$$M_r(t) = \sqrt{|\mathbf{M}|^2 - M_z^2(t)} = |\mathbf{M}|\operatorname{sech}(\alpha\gamma' B_0 t + c) \tag{2.72}$$

Note that near equilibrium, the condition $\gamma' B_0 \frac{\alpha}{|\mathbf{M}|} t + c \gg 1$ holds, so the amplitude of the oscillations decays approximately exponentially.

$$M_r(t) = |\mathbf{M}|\operatorname{sech}(\alpha\gamma' B_0 t + c) \approx 2|\mathbf{M}|\exp(-\alpha\gamma' B_0 t - c) \tag{2.73}$$

indicating that at small displacements from equilibrium, the LLG equation behaves similarly to the harmonic oscillator model, i.e. the system oscillates at a resonance frequency ω_0 with the amplitude of the oscillations decreasing exponentially with a rate constant $\Gamma = \alpha\gamma' B_0 = \alpha\omega_0$.

49

To couple the LLG equation to Maxwell's equations, we propagate $\mathbf{M}$ at each time step assuming a time-independent $\mathbf{B}_{\text{eff}}$: $\mathbf{M}$ is updated by rotating $\mathbf{M}$ about $\mathbf{B}_{\text{eff}}$ by an angle $\gamma' B_{\text{eff}} \Delta t$ according to Eq. 2.66, followed by a reorientation of $\mathbf{M}$ towards the equilibrium position according to Eq. 2.71. The magnetic dipole Hamiltonian $\hat{\mathbf{H}}$ and the effective magnetic field $\mathbf{B}_{\text{eff}}$ are recalculated at each time step. In this case, the external $\mathbf{H}$ propagated by Maxwell's equations is converted to $\mathbf{B}$ using the constitutive relation $\mathbf{B} = \mu_0 \mathbf{H}$. Note that the constitutive relation uses $\mu = 1$ because any magnetic behavior of the material is handled explicitly by propagating the LLG equation. $\mathbf{M}$ has the same spatial discretization as $\mathbf{H}$ and is updated simultaneously with $\mathbf{H}$. The magnetization couples into Ampere's law (Eq. 2.4) through the bound current $\mathbf{J}_{\text{b}}$, which is defined as

$$\mathbf{J}_{\text{b}} = \nabla \times \mathbf{M} \tag{2.74}$$

Electromagnetic sources are typically defined as current sources and enter into the simulation as an artificial contribution to $\mathbf{J}$. An intuitive source function is the Morlet (or Gabor) wavelet, which is composed of a Gaussian pulse envelope multiplied by a sinusoidal oscillation at the desired center frequency. However, care must be taken when using a Morlet wavelet because it can provide a significant DC field if the bandwidth is comparable to the carrier frequency. Although a DC field is not explicitly forbidden by Maxwell's equations, it is not excited by most excitation mechanisms and can result in large discrepancies between experiment and calculations. A common solution is to use the first (or higher) time derivative of the Gaussian function as the source function to eliminate the DC contribution. In Section 3.3, we describe THz generation in LN via optical rectification, which makes the Ricker wavelet (the second time derivative of a Gaussian function) a convenient source term for THz simulations.

In order to terminate the simulation space, absorbing boundary conditions are typically used to suppress reflections off of the simulation boundaries. This is typically implemented by using perfectly matched layers [77], where the electric and magnetic conductivities, σ_{e} and σ_{m}, are artificially increased towards the simulation boundary.

The ratio of σ_e to σ_m is chosen so that reflections off of the absorbing boundary are suppressed. This is done by keeping the wave impedance Z constant. The complex wave impedance is given by

$$Z = \sqrt{\frac{\mu + i\dfrac{\sigma_m}{\omega}}{\varepsilon + i\dfrac{\sigma_e}{\omega}}} \tag{2.75}$$

where ω is the angular frequency. This gives the simple condition that $\sigma_e/\sigma_m = \varepsilon/\mu$ to minimize reflections off of the boundary layer. Perfectly matched layers are typically implemented using the transformation

$$\frac{\partial}{\partial x} \rightarrow \frac{1}{1 + i\dfrac{\sigma_x}{\omega}}\frac{\partial}{\partial x} \tag{2.76}$$

(plus cyclic permutations) for the spatial derivatives in Maxwell's equations before applying the finite difference scheme. Notes on how to implement perfectly matched layers can be found in Ref. [78].

Chapter 3

Phonon-polaritons in LN waveguides

The THz polaritonics platform, named in reference to the THz-frequency phonon-polaritons that are formed as a result of strong coupling between the THz frequency electromagetic waves and the polar lattice vibrations in $LiNbO_3$ (LN) and $LiTaO_3$, uses thin $<100\,\mu m$ LN and LT slab waveguides for optical generation and detection of THz fields. A femtosecond laser pulse is focused into the LN waveguide, which launches polaritons away from the pumping region. The polaritons are confined to the slab and propagate in the transverse electric (TE) dielectric waveguide modes. The electric field component of the polaritons can be read out using a linearly polarized femtosecond probe pulse via electro-optic sampling. In this way, the polaritons can be monitored with sub-wavelength spatial resolution and sub-cycle temporal resolution as they interact with structures or samples integrated into the waveguide or deposited on the waveguide surface.

Here, we develop a framework for describing the phonon-polaritons used in our experiments. We start with the classical model for phonon-polaritons in a bulk material. The thickness of the LN and LT slabs is comparable to the THz wavelength (1 THz frequency $= 300\,\mu m$ wavelength in free space), so the slab acts as a dielectric waveguide. The mode profiles and dispersion for a free-standing LN slab are calculated. Lastly, we describe the nonlinear optical processes that allow for excitation and detection of the THz fields.

3.1 Phonon-polariton dispersion

Polaritons are quasiparticles that form as a result of strong-coupling between an electromagnetic wave and a material excitation through an electric-dipole (or magnetic-dipole) interaction. Here, we follow the treatment previously used in literature [79–82]. In LiNbO$_3$ (LN) and LiTaO$_3$ (LT), the THz electric field couples to the vibrational modes of the ionic crystal lattice to form phonon-polaritons. The ionic motion can be modeled as a harmonic oscillator, which has a linear susceptibility given by

$$\chi(\omega) = \frac{\sigma \omega_{\text{TO}}^2}{\omega_{\text{TO}}^2 - \omega^2 + i\omega\Gamma} \tag{3.1}$$

where ω_{TO} is the transverse phonon frequency, σ is the oscillator strength, and Γ is the phenomenological damping rate. Although LN and LT both have many THz-frequency phonon modes, here we only consider the lowest frequency mode. The THz bandwidth used in polaritonics experiments extends up to roughly $2\,\text{THz}$, so the lowest frequency mode, which has the largest oscillator strength, provides the main contribution to the dispersion. The contribution from the rest of the vibrational modes is summarized by the high-frequency permittivity ε_∞, which is simply the sum of the oscillator strengths. Both LN and LT are uniaxial crystals where the unique c-axis is called the "extraordinary" axis and the equivalent a and b axes are called the "ordinary" axes. Both materials have negative birefringence, meaning that extraordinary rays experience a smaller refractive index than ordinary rays. The Lorentzian dispersion parameters for LN and LT are summarized in Table 3.1. Normally, the linear electric permittivity ε is a frequency-dependent rank-2 tensor. However, by choosing a coordinate system where the extraordinary axis is aligned with one of the principle coordinate axes, ε is diagonalized. This allows us to treat light polarized along the x, y, and z axes independently. The dielectric function can be written as

$$\varepsilon(\omega) = \varepsilon_\infty + \frac{\sigma \omega_{\text{TO}}^2}{\omega_{\text{TO}}^2 - \omega^2 + i\omega\Gamma} \tag{3.2}$$

In general, the dispersion can be determined from the dielectric function through

	LiNbO$_3$		LiTaO$_3$	
	eo	o	eo	o
ϵ_∞	10.0	19.5	7.6	17.4
σ	16.0	22.0	30.0	24.1
$\omega_{\mathrm{TO}}/2\pi$ (THz)	7.4	4.6	6.0	4.3
$\Gamma/2\pi$ (THz)	0.63	0.42	0.84	0.42

Table 3.1: **Summary of material parameters for LN and LT.** Values taken from Ref. [83] for LN and Ref. [84] for LT. eo = extraordinary, o = ordinary

the relation

$$k = \frac{\omega\sqrt{\varepsilon}}{c} \tag{3.3}$$

where k is the wavevector, ω is the angular frequency, and c is the vacuum speed of light. We will neglect polariton damping ($\Gamma = 0$) for simplicity. Combining Eq. 3.2 and 3.3 gives the characteristic equation

$$\varepsilon_\infty \omega^4 - \left(\varepsilon_0 \omega_{\mathrm{TO}}^2 + c^2 k^2\right)\omega^2 + \omega_{\mathrm{TO}}^2 c^2 k^2 = 0 \tag{3.4}$$

where $\varepsilon_0 = \varepsilon_\infty + \sigma$ is the low-frequency permittivity. The solutions to this equation are

$$\omega_\pm = \sqrt{\frac{1}{2}\frac{\varepsilon_0\omega_{\mathrm{TO}}^2 + c^2 k^2}{\varepsilon_\infty} \pm \frac{1}{2}\sqrt{\left(\frac{\varepsilon_0\omega_{\mathrm{TO}}^2 + c^2 k^2}{\varepsilon_\infty}\right)^2 - \frac{4\omega_{\mathrm{TO}}^2 c^2 k^2}{\varepsilon_\infty}}} \tag{3.5}$$

Here, we only keep the positive solutions. The two solutions, plotted in Fig. 3-1, correspond to the upper polariton and lower polariton branches.

At high wavevectors ($ck \gg \omega_0$), the dispersion is approximated by

$$\omega_+ = \frac{ck}{\sqrt{\varepsilon_\infty}} \tag{3.6}$$

$$\omega_- = \omega_{\mathrm{TO}} \tag{3.7}$$

The lower polariton branch is "phonon-like" and is approximately constant at the transverse optical phonon frequency. The upper polariton branch is "photon-like" and has linear wavevector dependence.
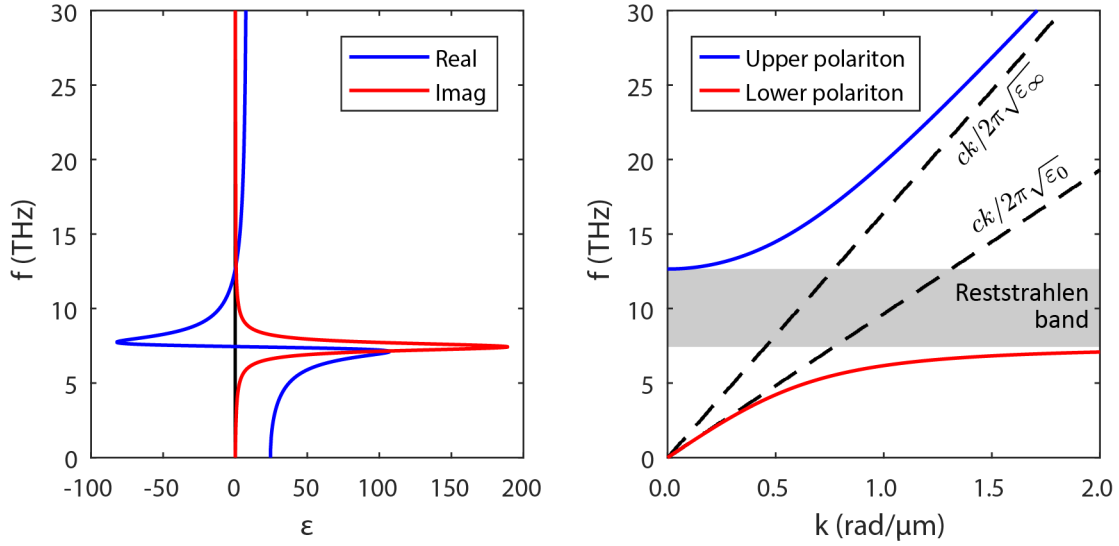
Figure 3-1: **Phonon-polariton dispersion in LN** (a) The real (blue) and imaginary (red) components of the electric permittivity in LN are plotted. Only the lowest-frequency transverse optical phonon mode was considered for this calculation. (b) Polariton dispersion calculated using Eq. 3.5. The upper polariton (blue) and lower polariton (red) branches are shown. The dashed lines show the photon-like dispersion in the high-frequency and low-frequency limits. The shaded region shows the Reststrahlen band, which corresponds to the region in (a) where $\mathrm{Re}\,(\varepsilon) < 0$.

At low wavevectors $(ck \ll \omega_0)$, the dispersion is approximated by

$$\omega_+ = \sqrt{\frac{\varepsilon_0}{\varepsilon_\infty}}\,\omega_{\mathrm{TO}} \tag{3.8}$$

$$\omega_- = \frac{ck}{\sqrt{\varepsilon_0}} \tag{3.9}$$

Now, the lower polariton branch is "photon-like" with linear wavevector dependence while the upper polariton branch is "phonon-like" and is approximately constant at the longitudinal optical phonon frequency ω_{LO}. In a typical polaritonics experiment, the excited THz bandwidth extends up to $\sim 2\,\mathrm{THz}$, so the relevant region of the polariton dispersion is the linear portion of the lower polariton branch. The longitudinal phonon frequency is given by the Lyddane-Sachs-Teller relation [85]

$$\frac{\omega_{\mathrm{LO}}}{\omega_{\mathrm{TO}}} = \sqrt{\frac{\varepsilon_0}{\varepsilon_\infty}} \tag{3.10}$$

Note that we have $\varepsilon(\omega) < 0$ in the region between ω_{TO} and ω_{LO}, which is known as the "Reststrahlen band" [86]. In this region, there are no propagating modes and incident light is strongly reflected.

At first glance, it may seem strange that a propagating electromagnetic wave can couple to a longitudinal phonon mode. For a planewave travelling through a medium, Gauss's law (Eq. 2.1) imposes the requirement $\mathbf{k} \cdot \mathbf{D} = \mathbf{k} \cdot \varepsilon \mathbf{E} = 0$ on the electric field. In most media, this leads to the requirement that $\mathbf{k} \cdot \mathbf{E} = 0$, and thus that light travels as a transverse wave. However, the phonon-polariton dispersion gives $\varepsilon(\omega_{\mathrm{LO}}) = 0$, so we can support a longitudinal electric field ($\mathbf{k} \cdot \mathbf{E} \neq 0$) without violating Gauss's law.

It is important to emphasize that the phonon-polaritons in LN and LT are hybrid quasiparticles formed by mixing a THz-frequency photon with the polar transverse optical phonons in LN and LT. It is inaccurate to think of the polaritons in terms of photons and phonons separately. In the classical picture, the travelling electromagnetic wave drives lattice vibrations in LN and LT. Simultaneously, the oscillating ions in the crystal lattice radiate out an electric field that interferes with the driving field. Energy is transferred back and forth between the electric field and the ionic motions, so both components are required to properly describe the mode.

3.2 Symmetric dielectric slab waveguides

The slabs used in the polaritonics platform have thickness comparable to the THz wavelength, so the THz fields propagate as dielectric waveguide modes. Consider a dielectric slab with the refractive index profile as shown in Fig. 3-2. The slab extends infinitely along the y and z axes. The slab has refractive index n_{core} and thickness d along the x-axis and is surrounded on both sides by an infinitely thick dielectric cladding with refractive index n_{clad}. The refractive index profile is given by

$$n(x) = \begin{cases} n_{\mathrm{core}} & |x| \leq \dfrac{d}{2} \\ n_{\mathrm{clad}} & |x| > \dfrac{d}{2} \end{cases} \tag{3.11}$$
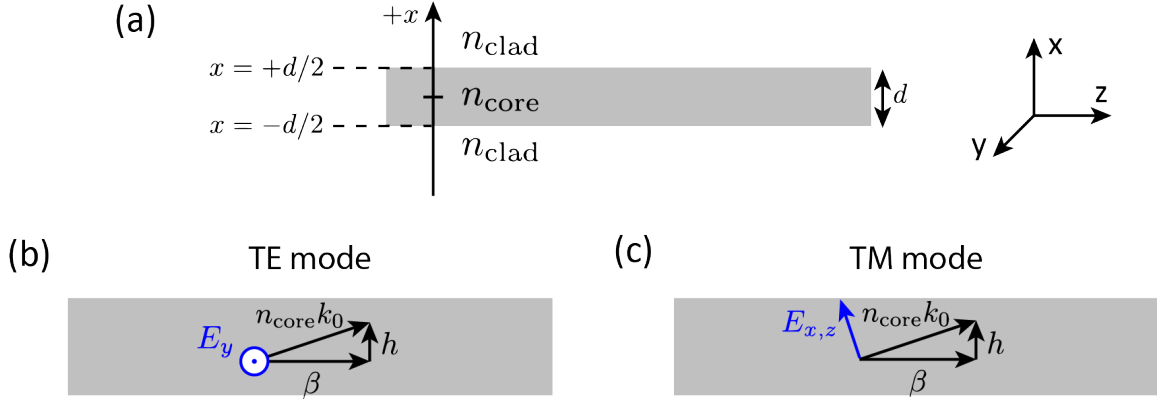
Figure 3-2: **The symmetric dielectric waveguide.** (a) Refractive index profile for a symmetric dielectric slab waveguide. The waveguide has a central high-index region with thickness d and refractive index n_{core}. A low-index cladding with refractive index n_{clad} surrounds the waveguide on both sides. (b) Transverse electric (TE) mode. The electric field is polarized along the y-axis. The field propagates along the z-axis with propagation constant β. h is the component of $n_{\text{core}}k_0$ perpendicular to the propagation direction and k_0 is the vacuum wavevector. (c) Transverse magnetic (TM) mode. The electric field has components polarized along the x- and z-axes.

For convenience, we place the origin of our coordinate axes at the center of the waveguide. Due to the mirror symmetry present in this geometry, we can separate the modes into two families: transverse electric (TE; the electric field is perpendicular to the propagation direction) and transverse magnetic (TM) modes. In the following sections, we will calculate the mode profiles and dispersion for both the TE and TM modes of the symmetric dielectric slab waveguide.

3.2.1 TE modes

For the TE mode, the electric field is polarized along the y-axis and the magnetic field has components polarized along the x and z axes. To solve for the TE modes, we solve the eigenproblem form of Maxwell's equations (Eq. 2.10) subject to transversality constraints Eq. 2.1 and Eq. 2.2. Within the high-index region, Eq. 2.10 produces sinusoidal solutions. For the mode to be well-behaved, the electric field must decay

exponentially to 0 at $x = \pm\infty$. Thus, $E_y(x)$ is given by

$$E_y(x) = \begin{cases} A\cos(hx) + B\sin(hx) & |x| \leq \dfrac{d}{2} \\ C\exp(qx) & x < -\dfrac{d}{2} \\ D\exp(-qx) & x > \dfrac{d}{2} \end{cases} \tag{3.12}$$

We can use Faraday's law (Eq. 2.11) to calculate $H_x(x)$ and $H_z(x)$ from $E_y(x)$.

$$H_x(x) = \frac{\beta}{\omega\mu_0} \begin{cases} A\cos(hx) + B\sin(hx) & |x| \leq \dfrac{d}{2} \\ C\exp(qx) & x < -\dfrac{d}{2} \\ D\exp(-qx) & x > \dfrac{d}{2} \end{cases} \tag{3.13}$$

$$H_z(x) = -\frac{i}{\omega\mu_0} \begin{cases} -hA\sin(hx) + hB\cos(hx) & |x| \leq \dfrac{d}{2} \\ qC\exp(qx) & x < -\dfrac{d}{2} \\ -qD\exp(-qx) & x > \dfrac{d}{2} \end{cases} \tag{3.14}$$

The parameters h and q are related to the propagation constant β by the following equalities.

$$\beta^2 = n_{\text{core}}^2 k_0^2 - h^2 = n_{\text{clad}}^2 k_0^2 + q^2 \tag{3.15}$$

This puts constraints on the possible values of β.

$$n_{\text{clad}} k_0 < \beta < n_{\text{core}} k_0 \tag{3.16}$$

At the surface of the slab, the E_y and H_z must be continuous across the interface due to Faraday's law (Eq. 2.3) and Ampere's law (Eq. 2.4) respectively. Due to the symmetry of the waveguide, the modes either have even symmetry ($B = 0$ and $C = D$) or odd symmetry ($A = 0$ and $C = -D$). For the even modes, we get the

59

following system of equations

$$A \cos\left(\frac{hd}{2}\right) = D \exp\left(-\frac{qd}{2}\right)$$
$$hA \sin\left(\frac{hd}{2}\right) = qD \exp\left(-\frac{qd}{2}\right)$$

(3.17)

which gives the characteristic equation

$$h \tan\left(\frac{hd}{2}\right) = q$$

(3.18)

For the odd modes, we get the following system of equations

$$B \sin\left(\frac{hd}{2}\right) = D \exp\left(-\frac{qd}{2}\right)$$
$$hB \cos\left(\frac{hd}{2}\right) = -qD \exp\left(-\frac{qd}{2}\right)$$

(3.19)

which gives the characteristic equation

$$h \cot\left(\frac{hd}{2}\right) = -q$$

(3.20)

At this point, we have one equation and two unknowns (h and q). To add a constraint, we define the normalized frequency V as

$$V^2 = \left(h^2 + q^2\right)\left(\frac{d}{2}\right)^2 = \left(n_{\text{core}}^2 - n_{\text{clad}}^2\right)\left(\frac{\omega d}{2c}\right)^2$$

(3.21)

This allows us to numerically solve the characteristic equation. The representative dispersion for a 50-μm LN slab is shown in Fig. 3-3a. Representative E_y field profiles are also shown in Fig. 3-3b for the three lowest-order TE modes.

The cutoff frequency for each mode can be found by finding the minimum frequency such that the characteristic equations still have a solution. For simplicity, we combine the two characteristic equations together to get

$$\tan\left(hd\right) = \frac{2hq}{h^2 - q^2}$$

(3.22)

60
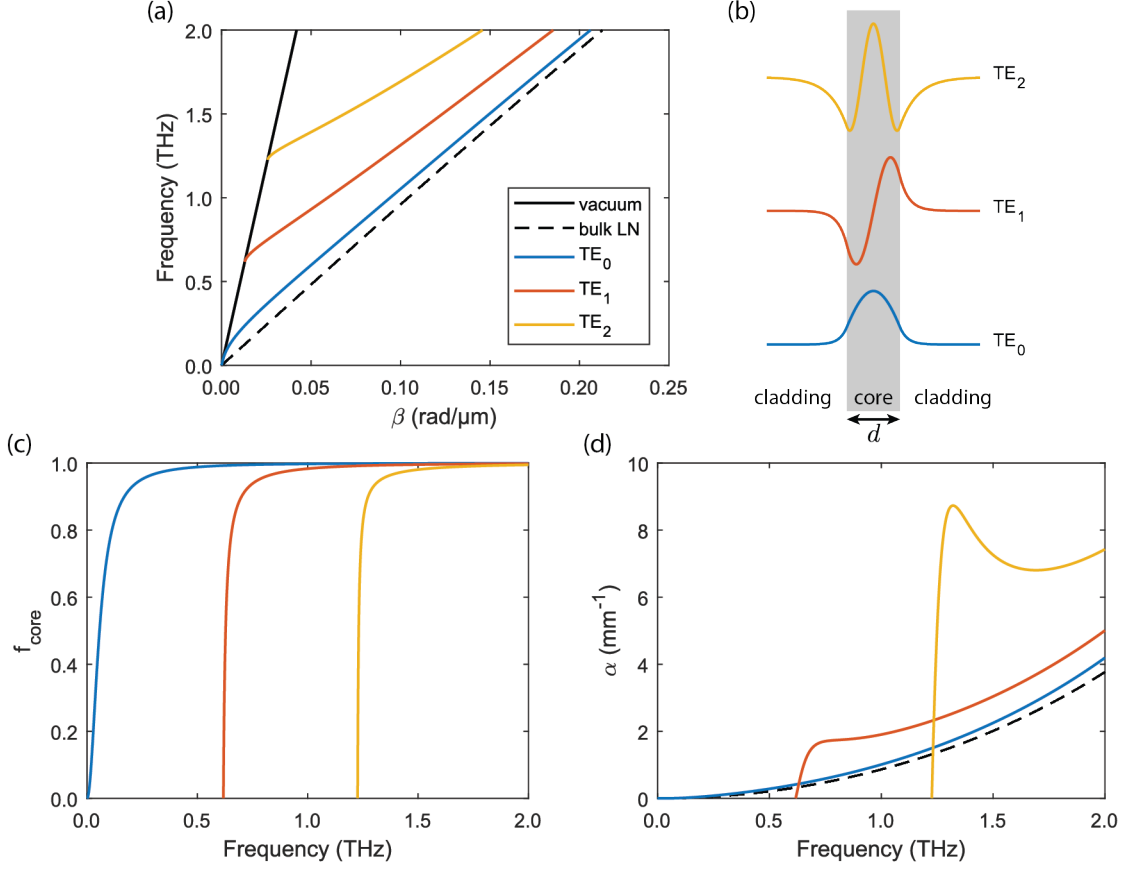
Figure 3-3: **TE modes in a symmetric dielectric waveguide.** (a) Calculated TE dispersion curves for a 50-µm LN slab waveguide. The parameters used for the LN bulk dispersion are taken from Table 3.1. The cladding material is air ($n_{\text{clad}} = 1$). (b) TE mode profiles for a LN slab with thickness $d = 50\,\mu\text{m}$ calculated at $1.5\,\text{THz}$. (c) Calculated fill fractions for the TE modes in a 50-µm LN waveguide. (d) Frequency-dependent absorption coefficients for the TE modes in a 50-µm LN waveguide.

Substituting for h and q and setting β to its minimum value ($\beta = \omega n_{\text{clad}}/c$) results in the equation

$$f_{\text{cutoff},m} = \frac{mc}{2d\sqrt{n_{\text{core}}^2 - n_{\text{clad}}^2}} \tag{3.23}$$

where m is an integer counting the TE_m modes.

We can also calculate the fill fractions for the modes. The energy density inte-

grated over the core region is

$$U_{\text{core}} = A^2 n_{\text{core}}^2 \left[\frac{d}{2} + \frac{1}{2h} \sin(hd) \right] \quad \text{(even modes)}$$

$$U_{\text{core}} = B^2 n_{\text{core}}^2 \left[\frac{d}{2} - \frac{1}{2h} \sin(hd) \right] \quad \text{(odd modes)}$$

(3.24)

and the energy density integrated over the cladding region (on both sides of the core) is

$$U_{\text{clad}} = \frac{D^2 n_{\text{clad}}^2}{q} \exp(-qd) \tag{3.25}$$

The relationships between A, B, and D are given by Eq. 3.17 and 3.19. The fill fractions are calculated using the equations

$$f_{\text{core}} = \frac{U_{\text{core}}}{U_{\text{core}} + U_{\text{clad}}}$$

$$f_{\text{clad}} = \frac{U_{\text{clad}}}{U_{\text{core}} + U_{\text{clad}}}$$

(3.26)

Note that U_{core} is proportional to n_{core}^2 while U_{clad} is proportional to n_{clad}^2. Therefore, for waveguides with a large dielectric contract, such as LN ($n_{\text{core}}/n_{\text{clad}} \approx 5$), f_{core} approaches unity very quickly. The core fill fractions for a 50-μm LN waveguide are plotted in Fig. 3-3b.

In the previous calculations, THz absorption was neglected. We can use perturbation theory to calculate the frequency-dependent absorption experienced by waveguided THz waves via Eq. 2.48, treating the imaginary part of the bulk LN and LT dispersion as the perturbation. The results are plotted in Fig. 3-3c. The calculated absorption coefficients are similar to the bulk absorption coefficients. The higher-order modes experience stronger absorption due to their lower group velocities. Note that there is a somewhat strong absorption feature near the cutoff frequency for each mode. This is due to the sharp decrease in group velocity where the TE dispersion starts to deviate from the vacuum light line.

3.2.2　TM modes

Although we do not routinely excite the TM waveguide modes in our experiments, it is still instructive to calculate the dispersion and properties of the modes. Following the same procedure as before, we can deduce the form of $H_y(x)$.

$$
H_y(x) = \begin{cases} A\cos(hx) + B\sin(hx) & |x| \leq \dfrac{d}{2} \\ C\exp(qx) & x < -\dfrac{d}{2} \\ D\exp(-qx) & x > \dfrac{d}{2} \end{cases} \tag{3.27}
$$

Using Ampere's law (Eq. 2.13), we can calculate $E_x(x)$ and $E_z(x)$ from $H_y(x)$.

$$
E_x(x) = -\frac{\beta}{\omega\epsilon_0} \begin{cases} \dfrac{1}{n_{\text{core}}^2}A\cos(hx) + \dfrac{1}{n_{\text{core}}^2}B\sin(hx) & |x| \leq \dfrac{d}{2} \\ \dfrac{1}{n_{\text{clad}}^2}C\exp(qx) & x < -\dfrac{d}{2} \\ \dfrac{1}{n_{\text{clad}}^2}D\exp(-qx) & x > \dfrac{d}{2} \end{cases} \tag{3.28}
$$

$$
E_z(x) = \frac{i}{\omega\epsilon_0} \begin{cases} -\dfrac{1}{n_{\text{core}}^2}hA\sin(hx) + \dfrac{1}{n_{\text{core}}^2}hB\cos(hx) & |x| \leq \dfrac{d}{2} \\ \dfrac{1}{n_{\text{clad}}^2}qC\exp(qx) & x < -\dfrac{d}{2} \\ -\dfrac{1}{n_{\text{clad}}^2}qD\exp(-qx) & x > \dfrac{d}{2} \end{cases} \tag{3.29}
$$

Applying the corresponding interface conditions, we get the characteristic equations

$$
\begin{aligned} h\tan\left(\frac{hd}{2}\right) &= \left(\frac{n_{\text{core}}}{n_{\text{clad}}}\right)^2 q & \text{(even modes)} \\ h\cot\left(\frac{hd}{2}\right) &= -\left(\frac{n_{\text{core}}}{n_{\text{clad}}}\right)^2 q & \text{(odd modes)} \end{aligned} \tag{3.30}
$$

The TM dispersion in a 50-μm LN waveguide is plotted in Fig. 3-4a. Representative E_x and E_z field profiles are also shown in Fig. 3-4b for the three lowest-order TM modes.

Like before, we can calculate the cutoff frequency from the condensed character-
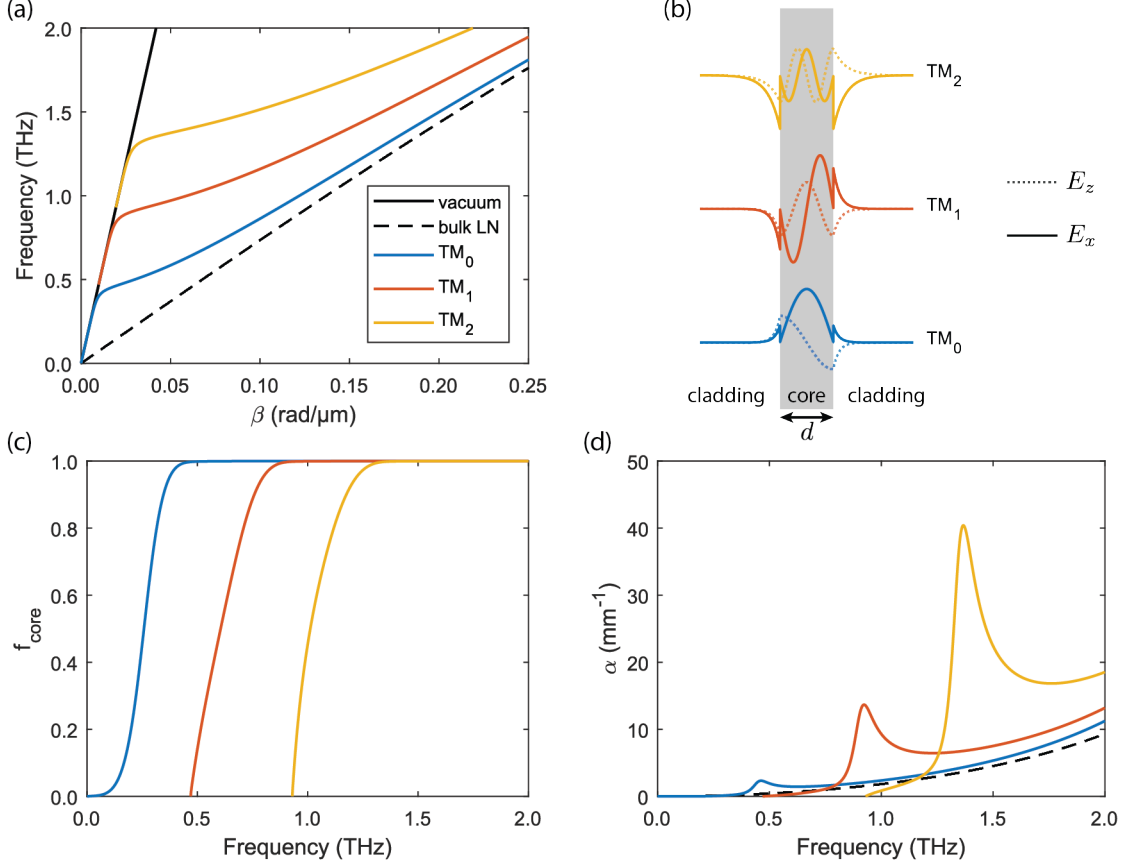
Figure 3-4: **TM modes in a symmetric dielectric waveguide.** (a) Calculated TM dispersion curves for a 50-µm LN slab waveguide. The parameters used for the LN bulk dispersion are taken from Table 3.1. The cladding material is air ($n_{\text{clad}} = 1$). (b) TM mode profiles for a LN slab with thickness $d = 50\,\mu\text{m}$ calculated at 1.5 THz. Both the E_x annd E_z field components are plotted. (c) Calculated fill fractions for the TM modes in a 50-µm LN waveguide. (d) Frequency-dependent absorption coefficients for the TM modes in a 50-µm LN waveguide.

istic equation

$$\tan\left(hd\right) = \frac{2h\bar{q}}{h^2 - \bar{q}^2} \tag{3.31}$$

where $\bar{q} = \left(n_{\text{core}}/n_{\text{clad}}\right)^2 q$. Setting $\beta = \omega n_{\text{clad}}/c$ gives

$$f_{\text{cutoff},m} = \frac{mc}{2d\sqrt{n_{\text{core}}^2 - n_{\text{clad}}^2}} \tag{3.32}$$

where m is an integer counting the TM_m modes. Note that for the symmetric waveguide, both the TE and TM modes have the same cutoff frequencies.

The fill fraction is calculated the same way as before. The energy density inte-

grated over the core region is

$$U_{\text{core}} = A^2 \left[\frac{(\beta^2 + h^2)\,d}{2} + \frac{(\beta^2 - h^2)}{2h} \sin{(hd)} \right] \quad \text{(even modes)}$$

$$U_{\text{core}} = B^2 \left[\frac{(\beta^2 + h^2)\,d}{2} - \frac{(\beta^2 - h^2)}{2h} \sin{(hd)} \right] \quad \text{(odd modes)}$$

$$(3.33)$$

and the energy density integrated over the cladding region (on both sides of the core) is

$$U_{\text{clad}} = \frac{D^2\,(\beta^2 + q^2)}{q} \exp{(-qd)} \tag{3.34}$$

where the coefficients A, B, and D are related by

$$A \cos{\left(\frac{hd}{2} \right)} = D \exp{\left(-\frac{qd}{2} \right)}$$

$$B \sin{\left(\frac{hd}{2} \right)} = D \exp{\left(-\frac{qd}{2} \right)}$$

$$(3.35)$$

The fill fractions are

$$f_{\text{core}} = \frac{U_{\text{core}}}{U_{\text{core}} + U_{\text{clad}}}$$

$$f_{\text{clad}} = \frac{U_{\text{clad}}}{U_{\text{core}} + U_{\text{clad}}}$$

$$(3.36)$$

Note that U_{core} and U_{clad} are not scaled by the square of the refractive index, so f_{core} does not increase as sharply as it does for the TE modes. The fill fractions for a 50-µm LN waveguide are plotted in Fig. 3-4b.

Like with the TE modes, we treat absorption using perturbation theory. The results are plotted in Fig. 3-4c and are similar to the results for the TE modes. Note that the spikes in the absorption coefficient are larger for the TM modes due to the sharper drop in group velocity where the dispersion deviates from the vacuum light line.

3.3 THz generation – Optical rectification

THz fields are excited in LN and LT through the second-order nonlinear process optical rectification, in which an ultrafast optical laser pulse enters the crystal and generates a nonlinear polarization proportional to the intensity of the driving field. To develop a simple model for THz generation, we start from Eq. 2.28 and Taylor expand the polarization $\mathbf{P}\left(\mathbf{r},t\right)$ in orders of the electric field $\mathbf{E}\left(\mathbf{r},t\right)$.

$$\mathbf{P}\left(\mathbf{r}.t\right) = \epsilon_0 \left[\chi_{\mathrm{e}}^{(1)} \mathbf{E}\left(\mathbf{r},t\right) + \chi_{\mathrm{e}}^{(2)} \mathbf{E}^2\left(\mathbf{r},t\right) + \ \cdots \ \right] \tag{3.37}$$

The first-order term is the linear polarization which was already treated in Section 2.2.1. All the higher-order terms collectively make up the nonlinear polarization $\mathbf{P}^{\mathrm{NL}}\left(\mathbf{r},t\right)$ and describe higher-order effects that become apparent at sufficiently large electric field strengths (a rough estimate gives $\mathbf{E} > \sim 10^{11}$ V/m) [87, 88]. Note that although the susceptibilities are written as scalars here for convenience, in general $\chi_{\mathrm{e}}^{(n)}$ is a tensor of rank $n+1$. By explicitly separating out $\mathbf{P}^{\mathrm{NL}}\left(\mathbf{r},t\right)$ in Eq. 2.30, we arrive at the equation

$$\nabla^2 \mathbf{E}\left(\mathbf{r},t\right) - \frac{n^2}{c^2}\frac{\partial^2}{\partial t^2}\mathbf{E}\left(\mathbf{r},t\right) = \frac{1}{\epsilon_0 c^2}\frac{\partial^2}{\partial t^2}\mathbf{P}^{\mathrm{NL}}\left(\mathbf{r},t\right) \tag{3.38}$$

The nonlinear process relevant for THz generation is optical rectification, which is a second-order nonlinear process where the generated polarization P_i^{OR} is proportional to the intensity of the input pulse.

$$P_i^{\mathrm{OR}} = \epsilon_0 d_{ijk} E_j E_k^* \tag{3.39}$$

where E_j and E_k are the input electric fields and $d_{ijk} = \frac{1}{2}\chi_{ijk}^{(2)}$ is the corresponding element of the effective nonlinear tensor. The superscript * denotes complex conjugate. From Eq. 2.30, we can show that the signal field radiated by the polarization is proportional to the second time-derivative of the polarization [89, 90]. Suppose we focus a Gaussian pump pulse with duration $\tau = 100\,\mathrm{fs}$ into a bulk LN crystal. The

jk	11	22	33	23,32	13,31	12,21
l	1	2	3	4	5	6

Table 3.2: **Voigt notation.** Convention used for converting between the uncontracted indices jk and the Voigt indices l.

excited THz waveform and spectrum are approximately given by

$$E\left(t\right) = \frac{4E_0}{\tau^2}\left(-\frac{1}{2} + \frac{t^2}{\tau^2}\right)\exp\left(-\frac{t^2}{\tau^2}\right) \tag{3.40}$$

$$\tilde{E}\left(\omega\right) = \tilde{E}_0\omega^2\exp\left(-\frac{\omega^2\tau^2}{4}\right) \tag{3.41}$$

The waveform $E\left(t\right)$ is known as a Ricker wavelet and is a commonly used source term for electromagnetic simulations. Using a 100 fs pump pulse, the generated THz pulse is predicted to have bandwidth up to 10 THz. This estimate only considers the bandwidth limitation due to the pump pulse duration and neglects other limiting factors such as the finite spot size of the pump beam and coupling to the TO phonon mode which has a resonance frequency below 10 THz. In practice, the spot size of the optical pump limits the excited range of wavevectors which in turn limits the bandwidth to approximately 2 THz.

The form of the effective nonlinear tensor d_{ijk} is determined by the crystal symmetry. Due to Kleinman symmetry, d_{ijk} is symmetric upon exchanging the last two indices, so we can use Voigt notation rewrite the nonlinear tensor as a more compact rank-2 tensor d_{il} using the convention given in Table 3.2 [87, 91]. LN and LT have crystal lattices belonging to the $3m$ point group, so d_{il} takes the form [87]

$$d = \begin{bmatrix} 0 & 0 & 0 & 0 & d_{15} & -d_{22} \\ -d_{22} & d_{22} & 0 & d_{15} & 0 & 0 \\ d_{31} & d_{31} & d_{33} & 0 & 0 & 0 \end{bmatrix} \tag{3.42}$$

The nonlinear coefficients for LN and LT at optical frequencies are summarized in Table 3.3. Note that in general, the nonlinear coefficients vary slightly depending on the optical wavelength and the crystal composition (e.g. doping). In both LN and LT,

	LiNbO$_3$	LiTaO$_3$
d_{22} (pm/V)	2.5	1.7
d_{31} (pm/V)	4.6	1.0
d_{33} (pm/V)	32.4	15.6
d_{15} (pm/V)	4.6	1.0

Table 3.3: **Summary of effective nonlinear coefficients for LN and LT.** Values taken from Refs. [92, 93].

the largest nonlinear coefficient is d_{33}, so THz generation is the most efficient when the pump is polarized along the extraordinary c-axis and the emitted THz fields are also polarized along the c-axis.

THz generation in LN and LT is noncollinear due to the large difference in extraordinary refractive index at optical and THz frequencies ($n_{\text{opt}} \approx 2.2$ and $n_{\text{THz}} \approx 5.1$ in LN; $n_{\text{opt}} \approx 2.2$ and $n_{\text{THz}} \approx 6.2$ in LT). We can treat the optical pump pulse as a moving THz source in LN and LT. At any instant in time, the pump pulse emits a spherical THz wave. Using Huygen's principle, constructive inference between the spherical wave gives a conical THz field propagating away from the pump region, as shown in Fig. 3-5a. The emitted cone of THz radiation is referred to as a Cherenkov cone [94] in reference to Cherenkov radiation observed in nuclear sciences which is emitted in a very similar geometry [95, 96]. The Cherenkov angle θ_c can be calculated using simple geometry to give the equation

$$\cos\left(\theta_c\right) = \frac{n_{\text{opt}}}{n_{\text{THz}}} \tag{3.43}$$

In LN and LT, this gives $\theta_c = 64°$ and $69°$, respectively, so the THz fields are excited with a predominant lateral wavevector component.

If a pump pulse is focused into a thin LN or LT slab, the emitted THz fields are launched laterally and couple very efficiently to the dielectric waveguide modes as shown in Fig. 3-5b. In our experiments, the optical pump pulse and the generated THz fields are both polarized along the in-plane c-axis, so the THz fields couple into the transverse electric (TE) waveguide modes. We can estimate the frequency-dependent THz generation efficiency for the different waveguide modes by first calculating the
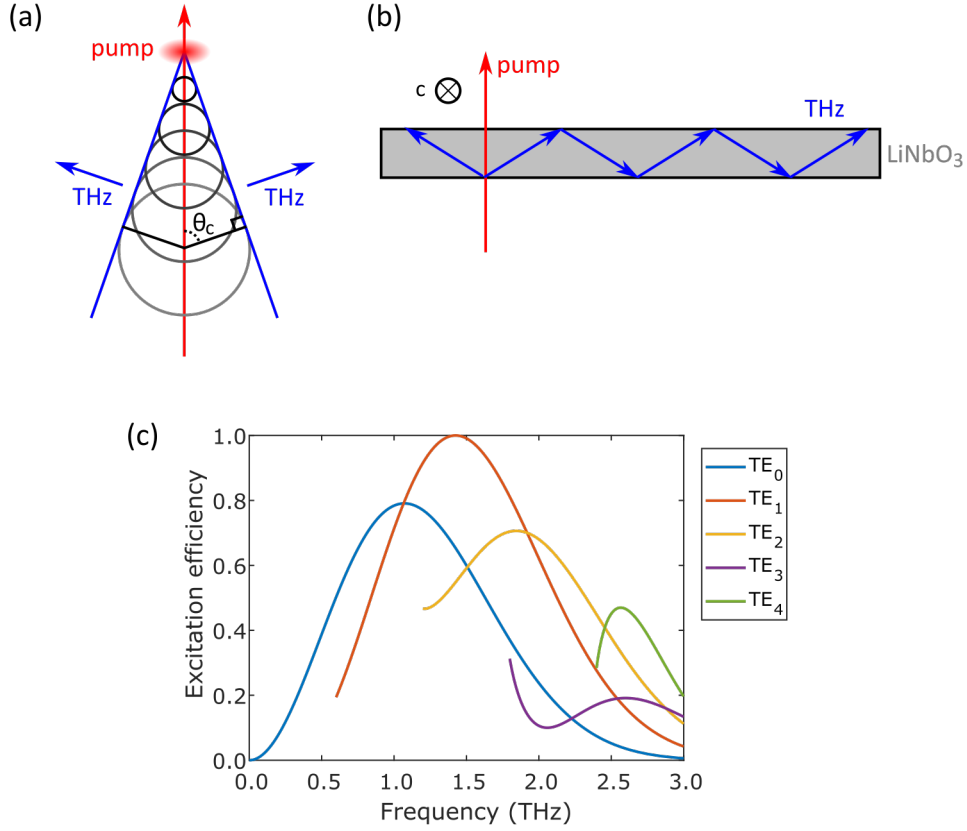
Figure 3-5: **THz generation in LN.** (a) Illustration of the Cherenkov cone. At any instant in time, the pump beam (red) excites a spherical wave of THz radiation. The THz wavefront resulting from constructive interference of the spherical waves propagates away from the pump region at the Cherenkov angle θ_c. (b) Ray optics diagram of the THz waves in a LN waveguide. The excited THz waves are launched with a large lateral wavevector component and are confined within the waveguide via total internal reflection. (c) Calculated relative THz generation efficiency for the TE modes in a 50-µm LN slab using a 100 fs pump pulse focused to a line 30 µm wide. The curves are calculated using Eq. 3.47.

THz field profile excited by a Gaussian pulse passing through the slab, then projecting the THz field pattern onto the waveguide mode profiles. We model the pump pulse using a Gaussian function that travels along the $+x$ direction with speed v_{pump}.

$$
I_{\mathrm{pump}}\left(x, z, t\right) = I_0 \exp\left[-\frac{(z - z_0)^2}{\sigma_z^2}\right] \exp\left[-\frac{(x - x_0 - v_{\mathrm{pump}}t)^2}{\sigma_x^2}\right] \tag{3.44}
$$

where σ_z is the width along the z-axis and σ_x is pulse extent along the x-axis which

is related to the pulse duration $\tau = \sigma_x / v_{\mathrm{pump}}$. x_0 and z_0 are the coordinates of the center of the Gaussian pulse at $t = 0$. Here, we use the same coordinate system as in Fig. 3-2 and assume that there is negligible variation of the pump profile along the y-axis. Using the TE mode profiles of the form

$$E_{\mathrm{THz}}(x, z, t) = E_m(x) \exp\left[i\left(\beta z - \omega t\right)\right] \tag{3.45}$$

the excitation efficiency $\eta_m(\omega)$ for the TE_m mode at the frequency ω can be estimated using the following integral.

$$
\begin{aligned}
\eta_m(\omega) &\propto \omega^2 \int_{-d/2}^{d/2} dx \int_{-\infty}^{\infty} dz \int_{-\infty}^{\infty} dt \; \exp\left(-\frac{z^2}{\sigma_z^2}\right) \\
&\quad \exp\left[-\frac{(x - v_{\mathrm{pump}}t)^2}{\sigma_x^2}\right] E_m(x) \exp\left[i\left(\beta z - \omega t\right)\right]
\end{aligned}
\tag{3.46}
$$

Because the THz fields are generated through optical rectification, the phase of the excited THz fields is independent of the phase of the optical pump, so the only phase factor to consider is that of the propagating waveguide mode. The factor of ω^2 accounts for the fact that the emitted THz field follows the second time derivative of the pump pulse intensity. Solving this integral gives

$$\eta_m(\omega) \propto \omega^2 \exp\left(-\frac{1}{4}\beta^2 \sigma_z^2\right) \exp\left(-\frac{1}{4}\omega^2 \tau^2\right) \int_{-d/2}^{d/2} E_m(x) \exp\left(-\frac{i\omega x}{v_{\mathrm{pump}}}\right) dx \tag{3.47}$$

The results of this equation are plotted in Fig. 3-5c for a 100 fs pump pulse focused to 30 μm width. Although we might expect a 100 fs pump pulse to generate THz fields with bandwidth up to 10 THz, the THz generation efficiency quickly drops past $\sim$2 THz. This is primarily due to the finite width of the pump beam, which limits the range of β that can be excited.

Interestingly, the complex exponential in the integral in Eq. 3.47 results in larger generation efficiencies for higher-order waveguide modes at higher frequencies. For example, consider the TE_0 and TE_1 modes at 1.5 THz. The pump pulse requires a time $\Delta t = d n_{\mathrm{opt}}/c \approx 370$ fs to traverse the thickness of the slab, so the 1.5 THz field

generated at the front face of the slab ends up being out of phase with the THz field generated at the back face. For the TE_0 mode where the sign of the THz field is the same over the thickness of the slab, this results in a decreased THz generation efficiency. In contrast, this results in a larger generation efficiency for the TE_1 mode where the signs of the field profile are opposite at the front and back faces of the slab.

When using multiple pump pulses, we can use the superposition principle to calculate the total THz generation efficiency by considering the interference between the THz fields excited by the individual pump pulses. For example, consider a series of N pulses separated spatially by Δz and temporally by Δt, as one might expect when using a stair-step "echelon" mirror to shape the pump pulse into a discrete tilted pulse front (such as in Ref. [97]). The generation efficiency can be estimated as

$$
\begin{aligned}
\eta_m(\omega) \propto \sum_{n=1}^{N} \omega^2 \int_{-d/2}^{d/2} dx \int_{-\infty}^{\infty} dz \int_{-\infty}^{\infty} dt \exp\left[-\frac{(z - n\Delta z)^2}{\sigma_z^2}\right] \\
\exp\left[-\frac{(x - n v_{\text{pump}}\Delta t - v_{\text{pump}}t)^2}{\sigma_x^2}\right] E_m(x) \exp\left[i(\beta z - \omega t)\right]
\end{aligned}
\tag{3.48}
$$

Carrying out the integral gives the following equation.

$$
\begin{aligned}
\eta_m(\omega) \propto \omega^2 \exp\left(-\frac{1}{4}\beta^2 \sigma_z^2\right) \exp\left(-\frac{1}{4}\omega^2 \tau^2\right) \\
\sum_{n=1}^{N} \exp\left[in(\beta\Delta z - \omega\Delta t)\right] \int_{-d/2}^{d/2} E_m(x) \exp\left(-\frac{i\omega x}{v_{\text{pump}}}\right) dx
\end{aligned}
\tag{3.49}
$$

The result looks similar to before, but now there is a summation over the phasors that gives the velocity matching condition. For perfect velocity matching, we require $\omega/\beta = \Delta z/\Delta t$. In other words, the laterial scan speed of the series of pump pulses $v_{\text{scan}} = \Delta z/\Delta t$ must match the phase velocity of the THz fields $v_{\text{ph}} = \omega/\beta$.

3.4 THz detection – Electro-optic sampling

The electric field component of the phonon-polaritons can be measured through electro-optic sampling. As the THz field propagates through the LN or LT waveg-

	LiNbO$_3$	LiTaO$_3$
r_{22} (pm/V)	3.4	1
r_{13} (pm/V)	8.6	7.9
r_{33} (pm/V)	30.8	35.8
r_{51} (pm/V)	28	20

Table 3.4: **Summary of electro-optic coefficients.** These values are for a 633 nm probe beam in LiNbO$_3$ and LiTaO$_3$ assuming a DC voltage. Values taken from Ref. [100].

uide, it modifies the local optical refractive index through the Pockels effect. The THz electric field perturbs the crystal lattice, which results in a small change in the electronic susceptibility [98, 99]. This results in a small modulation in the refractive index Δn given by [87]

$$\Delta n_i = -\frac{1}{2}n_i^3 r_{ij}E_j \tag{3.50}$$

Similar to effective nonlinear tensor, the non-zero elements of the electro-optic tensor are determined by the crystal symmetry. For LN and LT, which belong to the $3m$ point group, r_{ij} takes the form (again using Voigt notation)

$$r = \begin{bmatrix} 0 & -r_{22} & r_{13} \\ 0 & r_{22} & r_{13} \\ 0 & 0 & r_{33} \\ 0 & r_{51} & 0 \\ r_{51} & 0 & 0 \\ -r_{22} & 0 & 0 \end{bmatrix} \tag{3.51}$$

The values for the electro-optic tensor elements in LN and LT are given in Table 3.4.

In LN and LT, the main contribution to the electro-optic response comes from the THz electric field coupling to the lowest-frequency transverse optical phonon [99, 101]. In our experiments, we use THz frequencies < 2 THz, so the atomic displacement is approximately in phase with the THz electric field. This means that we can safely neglect any lag time in the electro-optic response.

The THz-induced change in refractive index can be read out by taking a linearly polarized ultrafast probe pulse and measuring the change in polarization after passing through the LN or LT waveguide. We can model the probe polarization using the Jones matrix formalism where the light polarization is described by a 2-element complex-valued column vector [102]. Each element is a phasor describing the amplitude and phase of the corresponding polarization. Here, we will use the linearly polarized basis with basis vectors $|V\rangle$ and $|H\rangle$ representing vertically polarized and horizontally polarized light, respectively. The corresponding Jones vectors are

$$|V\rangle = \begin{bmatrix} 1 \\ 0 \end{bmatrix} \qquad |H\rangle = \begin{bmatrix} 0 \\ 1 \end{bmatrix} \tag{3.52}$$

Optical elements modify the phase of the two polarization components and are described by 2-by-2 matrices that act on the state vector. For example, suppose we have a generic birefringent material that induces a relative phase delay of ϕ for the horizontal polarization. The corresponding Jones matrix is

$$\begin{bmatrix} 1 & 0 \\ 0 & \exp{(i\phi)} \end{bmatrix} \tag{3.53}$$

The detection geometry for our experiments is shown in Fig. 3-6. The probe light is initially polarized at a 45° angle relative to the LN c-axis, which is vertical. The probe passes through the LN slab, followed by a compensating crystal (a LN slab identical to the sample LN slab but rotated by 90°) and a quarter-wave plate with its fast axis aligned along the vertical axis. A Wollaston prism is used to decompose the probe pulse into two beams polarized parallel and perpendicular to the initial polarization. For convenience, we define the following Jones vectors.

$$|+45°\rangle = \frac{1}{\sqrt{2}} \begin{bmatrix} 1 \\ 1 \end{bmatrix} \qquad |-45°\rangle = \frac{1}{\sqrt{2}} \begin{bmatrix} 1 \\ -1 \end{bmatrix} \tag{3.54}$$

We take $|+45°\rangle$ to describe the initial probe polarization.
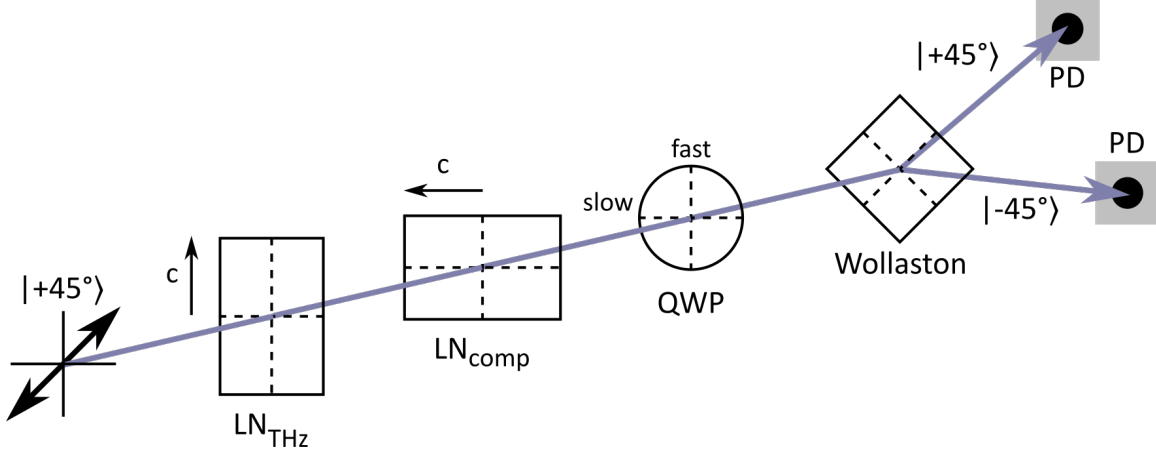
Figure 3-6: **Schematic illustration of polariton detection.** The linearly polarized probe beam passes through the LN waveguide and a compensating crystal (an identical LN waveguide rotated by 90°). The THz-induced birefringence in the LN slab is encoded as a change in probe polarization. A quarter-wave plate (QWP) and Wollaston prism are used to convert the change in polarization into an intensity modulation, which is measured using a balanced pair of photodiodes (PD).

The LN slab is treated as a birefringent slab of material where the phase delay experienced by vertically polarized light is dependent on the THz electric field strength. This gives the Jones matrix

$$
\text{LN}_{\text{THz}} =
\begin{bmatrix}
\exp\left(\dfrac{in_{\text{e}}\omega d}{c}\right)\exp\left(i\Delta\phi_{\text{e}}\right) & 0 \\[2ex]
0 & \exp\left(\dfrac{in_{\text{o}}\omega d}{c}\right)\exp\left(i\Delta\phi_{\text{o}}\right)
\end{bmatrix}
\tag{3.55}
$$

where $n_{\text{e,o}}$ is the extraordinary/ordinary optical refractive index, c is the vacuum speed of light, d is the thickness of the LN slab, and $\Delta\phi_{\text{e,o}} = 2\pi\Delta n_{\text{e,o}}d/\lambda_0$ is the THz-induced phase delay for extraordinary/ordinary rays. For each element, the first exponential term describes the phase delay caused by the static birefringence in LN. The contribution from the static birefringence in LN can be eliminated by including a compensating LN crystal, which is a second LN crystal that is identical to the first except rotated by 90°, in the beam path. The Jones matrix for the compensating

crystal is

$$
\text{LN}_{\text{comp}} = \begin{bmatrix} \exp\left(\dfrac{in_{\text{o}}\omega d}{c}\right) & 0 \\[2ex] 0 & \exp\left(\dfrac{in_{\text{e}}\omega d}{c}\right) \end{bmatrix} \tag{3.56}
$$

The probe then passes through a quarter-wave plate with the fast axis aligned with the vertical axis, which has the following Jones matrix.

$$
\text{QWP} = \begin{bmatrix} 1 & 0 \\ 0 & i \end{bmatrix} \tag{3.57}
$$

Electro-optic sampling uses a Wollaston prism to separate the probe light into two linear polarizations oriented $\pm 45°$ relative to vertical. The intensities of each polarization are read out using balanced photodiodes. Assuming ideal optics, the measured intensities $I_\pm$ are given by

$$
\begin{aligned}
I_+ &= |\langle +45°| \,(\text{QWP})\,(\text{LN}_{\text{comp}})\,(\text{LN}_{\text{THz}}) \,|+45°\rangle|^2 = \frac{1}{2}\left[1 + \sin\left(\Delta\phi_{\text{e}} - \Delta\phi_{\text{o}}\right)\right] \\
I_- &= |\langle -45°| \,(\text{QWP})\,(\text{LN}_{\text{comp}})\,(\text{LN}_{\text{THz}}) \,|+45°\rangle|^2 = \frac{1}{2}\left[1 - \sin\left(\Delta\phi_{\text{e}} - \Delta\phi_{\text{o}}\right)\right]
\end{aligned} \tag{3.58}
$$

The balanced signal is calculated as follows

$$
\frac{\Delta I}{I_0} = \frac{I_+ - I_-}{I_+ + I_-} = \sin\left(\Delta\phi_{\text{e}} - \Delta\phi_{\text{o}}\right) \tag{3.59}
$$

In the low field limit, we can linearize the sine function and get the following equation. We assume that the THz field is polarized along the z-axis, which is typical for our experiments.

$$
\frac{\Delta I}{I_0} \approx \Delta\phi = -\frac{\pi d}{\lambda_0}\left(n_{\text{e}}^3 r_{33} - n_{\text{o}}^3 r_{13}\right) E_z \tag{3.60}
$$

Using a 400-nm probe pulse in a 50-µm LN slab, this equation becomes approximately

$$
\frac{\Delta I}{I_0} \approx -\left(0.0104\,\text{cm/kV}\right) E_z \tag{3.61}
$$

so a $1\,\text{kV/cm}$ THz field gives about 1% $\Delta I/I_0$ signal.

So far, we have assumed that the electric field is static. However, the waveguided

75
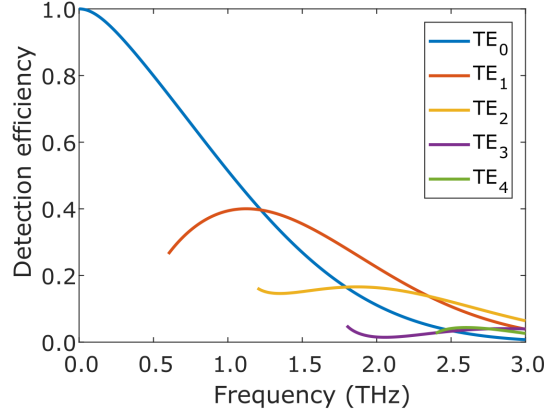
Figure 3-7: **THz detection efficiency in a LN slab.** Calculated THz detection efficiency for the TE modes in a 50-µm LN slab using a 100 fs probe pulse focused to a point 10 µm wide. The curves are calculated using Eq. 3.62.

THz field travels laterally as the optical probe passes through the slab, so the optical probe samples a time-varying THz field. The average THz-induced phase delay experienced by a probe beam passing through the LN slab with thickness d can be calculated using the following equation.

$$\Delta\phi \propto \exp\left(-\frac{1}{4}\beta^2\sigma_z^2\right) \exp\left(-\frac{1}{4}\omega^2\tau^2\right) \int_{-d/2}^{d/2} E_m\left(x\right) \exp\left(-i\frac{\omega x}{v_{\text{probe}}}\right) dx \qquad (3.62)$$

where σ_z is the width of the probe pulse and τ is the pulse duration, $E_m\left(x\right)$ is the TE dielectric waveguide mode profile, and v_{probe} is the group velocity of the probe beam in LN. Evaluating this integral numerically, we can calculate the frequency-dependent detection efficiency, which is defined as $\Delta\phi$ normalized by the phase delay that would result from a DC electric field. The results are plotted in Fig. 3-7. The detection efficiency is the highest at low frequencies and decreases at higher frequencies. This makes intuitive sense because at higher frequencies, the probe pulse samples a rapidly varying electric field.

3.5 Time-resolved polariton imaging

The THz fields in the waveguides can be imaged via polarization gating imaging using a collimated probe beam [103, 104]. A charge-coupled device (CCD) camera captures images of the two polarization components separated out by the Wollaston prism. The polarization gating imaging setup is shown in Fig. 3-8a. The imaging setup uses a self-compensating geometry to account for small variations in the LN slab thickness. The probe beam passes through the LN slab and is imaged onto a retroreflecting mirror. A quarter-wave plate is placed just before the mirror in order to exchange the amplitudes of the horizontal and vertical polarization components of the probe beam. As a result, each portion of the probe beam is imaged back onto the same part of the LN waveguide and any change in polarization due to the LN static birefringence is eliminated. The pump beam arrives at the LN waveguide after the probe passes through the waveguide the first time, so the THz-induced signal is only recorded on the return trip. Fig. 3-8b shows representative THz images captured using this technique.
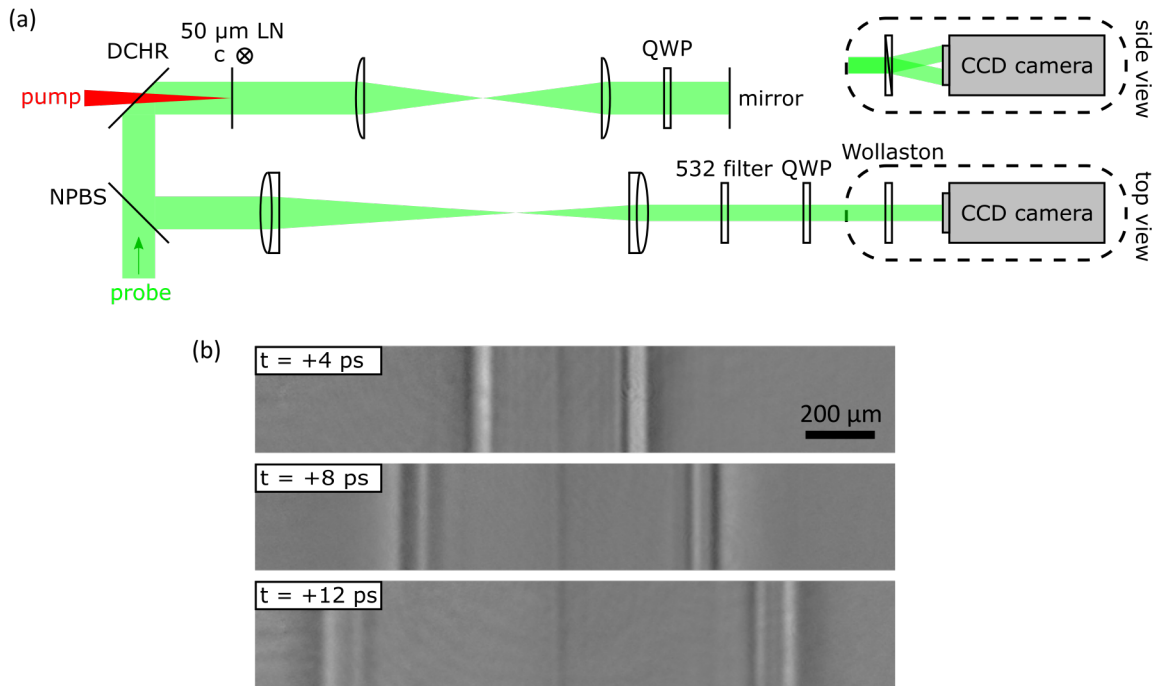
Figure 3-8: **Polariton imaging.** (a) Schematic illustration of the polarization gating imaging setup. A linearly polarized probe beam passes through the LN waveguide and is imaged onto a retroreflecting mirror using a $4f$-imaging system. A quarter-wave plate (QWP) is placed in the $4f$-imaging system. The probe beam is then imaged back onto the LN waveguide. The pump beam is focused onto the LN waveguide through a dichroic mirror (DCHR; reflects $532\,\mathrm{nm}$, transmits $800\,\mathrm{nm}$) and arrives after the probe reflects off of the mirror, so the THz signal is only measured on the return trip. The probe beam is then directed into the detection arm using a non-polarizing beam splitter (NPBS) and is imaged onto a charged-coupled device (CCD) camera. A quarter-wave plate and Wollaston prism are used to convert the change in probe polarization into an intensity modulation. (b) Representative images of the THz fields at various pump-probe delays. The THz field amplitude is proportional to the image contrast.

Chapter 4

Enhancement of THz generation using bounce crystals

This work was done in close collaboration with Blake Dastrup (Nelson Group) from MIT. Content adapted from (Ref. [105]): B. S. Dastrup*, **E. R. Sung***, F. Wulf, C. Saraceno, K. A. Nelson. "Enhancement of THz generation in LiNbO₃ waveguides via multi-bounce velocity matching," *Light Sci. Appl.* **11**, 335 (2022).

A key tool for high-field THz generation in LN is the use of a spatiotemprally shaped optical tilted pulse front (TPF). The large refractive index mismatch at optical and THz frequencies results in noncollinear propagation of the optical pump and the generated THz field. This results in a Cherenkov cone of THz radiation that emanates away from the pump region [94]. In the TPF technique, the optical pump is shaped to have an angled intensity front that matches the Cherenkov angle, which leads to constructive buildup of the THz pulse [15]. TPF pumping has enabled routine generation of THz pulses with electric field strengths reaching the MV/cm range [16, 17], which has opened the way for nonlinear THz spectroscopy [28, 106–109], electron acceleration for coherent x-ray generation [110], and THz-induced phase transitions [26, 29, 30].

Many studies have been devoted to optimizing generation efficiency, reaching optical-to-THz conversion efficiencies in the few % range [111–113], and on under-

standing the physical mechanisms that limit the efficiency [114, 115] of TPF THz generation. In particular, angular dispersion introduced by the grating used to create the pulse front tilt limits the spatial extent over which THz generation can occur. To minimize the effect of angular dispersion, stair-step "echelon" mirrors have been used in place of an optical grating to generate a discrete TPF [97, 116]. Many other variations to improve upon the traditional TPF pumping scheme have also been demonstrated [117–121].

In this chapter, we demonstrate a novel velocity-matching scheme in LN in which the optical pump beam undergoes repeated total internal reflection (TIR) between the parallel faces of a slab of LN, following a back-and-forth trajectory with an in-plane wavevector that satisfies the velocity-matching condition such that the optical beam progresses laterally within the slab at the same speed as the THz wave that it generates. We demonstrate this scheme using thin (50-100 µm) LN slabs with beveled edges through which pump light is coupled into the crystal as illustrated in Fig. 4-1a. We use the LN waveguide to confine both the THz field and the optical pump field. This allows us to effectively reuse the pump light through its many traversals back and forth through the LN slab, resulting in a THz field buildup similar to that achieved using the separate parts of a tilted pulse front beam to pump successive LN regions. The resulting enhanced field is highly encouraging for the development of a robust chip-based THz spectroscopy and signal processing platform within the scope of THz polaritonics using relatively low optical pump pulse energy.

4.1   Velocity-matching condition

THz generation by optical rectification (OR) in LN is a second-order nonlinear optical process with the phase-matching relation,

$$\mathbf{k}_\Omega = \mathbf{k}_\omega - \mathbf{k}_{\omega-\Omega} \tag{4.1}$$
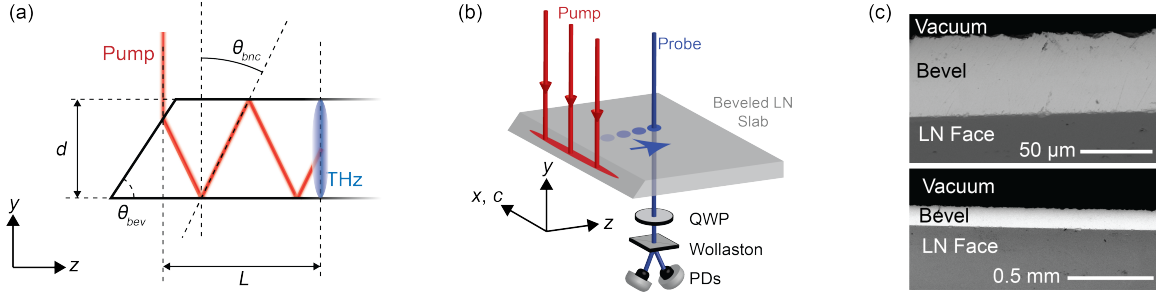
Figure 4-1: **Experimental "bounce" geometry and beveled LN images.** (a) Schematic illustration of a beveled LN slab with thickness d. Pump light is incident at the bevel angle θ_{bev} with respect to the bevel normal and refracts into the crystal at "bounce" angle θ_{bnc}. Buildup distance for the THz generation is denoted as L. (b) Diagram of the experimental geometry. The LN slab is oriented with the optic axis (c-axis) parallel to the beveled edge. The c-polarized pump pulse is focused on the bevel and the THz field is sampled at multiple distances from the bevel. After passing through the sample, the probe pulse is sent through a quarter-wave plate (QWP) and a Wollaston prism and then measured on balanced photodiodes (PDs). (c) SEM images of the beveled edge of the LN slab at two different scales. The slab is viewed from the top down (the y-direction as defined in (b)). The light gray region shows the beveled edge and the dark gray region below it showes the face of the LN slab.

where $\mathbf{k}_\Omega$ is the wavevector at the THz frequency Ω, and $\mathbf{k}_\omega$ and $\mathbf{k}_{\omega-\Omega}$ are the wavevectors at the optical frequencies ω and $\omega - \Omega$ respectively. Considering only the projection along the direction of optical pump propagation allows us to express the Cherenkov angle θ_{c} between $\mathbf{k}_\Omega$ and $\mathbf{k}_\omega$ in terms of the THz and optical wave parameters,

$$\cos\left(\theta_{\text{c}}\right) = \frac{c}{\Omega n_{\text{THz}}} \left(\mathbf{k}_\omega - \mathbf{k}_{\omega-\Omega}\right) \tag{4.2}$$

where n_{THz} is the THz refractive index and c is the vacuum speed of light. We assume that the angle between $\mathbf{k}_\omega$ and $\mathbf{k}_{\omega-\Omega}$ is small because $\Omega \ll \omega$. Recognizing the right-hand side as the discrete derivative $\left(\mathbf{k}_\omega - \mathbf{k}_{\omega-\Omega}\right)/\Omega \approx \partial k/\partial \omega = 1/v_{\text{gr}}^{\text{opt}}$ multiplied by $c/n_{\text{THz}} = v_{\text{ph}}^{\text{THz}}$, we arrive at the expression,

$$\cos\left(\theta_{\text{c}}\right) = \frac{v_{\text{ph}}^{\text{THz}}}{v_{\text{gr}}^{\text{opt}}} \tag{4.3}$$

where $v_{\text{gr}}^{\text{opt}}$ is the optical group velocity and $v_{\text{ph}}^{\text{THz}}$ is the THz phase velocity.

In the case of an optical pump beam focused to a round spot, the THz field emanates from the pump as a cone of light at the Cherenkov angle θ_c, so called in reference to Cherenkov radiation, which is isomorphic to the THz generation process described here [94]. In our scheme, the in-plane projection of the pump velocity is given by,

$$v_{\mathrm{gr},z}^{\mathrm{opt}} = v_{\mathrm{gr}}^{\mathrm{opt}} \sin\left(\theta_\mathrm{bnc}\right) \tag{4.4}$$

where $v_{\mathrm{gr},z}^{\mathrm{opt}}$ is the component of the optical group velocity along the z-direction and θ_bnc is the bounce angle defined in Fig. 4-1a. When $\theta_\mathrm{bnc} - \theta_\mathrm{c} = \pi/2$, substitution of Eq. 4.4 into Eq. 4.3 gives $v_{\mathrm{gr},z}^{\mathrm{opt}} = v_{\mathrm{ph}}^{\mathrm{THz}}$. In other words, the THz phase velocity is matched to the group velocity of the optical pump in the positive z-direction. Waveguide dispersion effectively introduces frequency dependence (beyond the weak frequency dependence due to material dispersion in LN) into the THz phase velocity $v_{\mathrm{ph}}^{\mathrm{THz}}\left(\Omega\right)$. In this case, the velocity-matching condition becomes

$$\sin\left[\theta_\mathrm{bnc}\left(\Omega\right)\right] = \frac{v_{\mathrm{ph}}^{\mathrm{THz}}\left(\Omega\right)}{v_{\mathrm{gr}}^{\mathrm{opt}}} \tag{4.5}$$

which indicates that for a given bounce angle, the velocity-matching condition will be satisfied optimally for a particular THz frequency.

The bounce angle θ_bnc can be written in terms of the bevel angle θ_bev using Snell's law. In these experiments, the pump beam is incident on the bevel at an angle θ_bev relative to the bevel normal and refracts into the crystal at an angle θ_bnc. Using the geometry shown in Fig. 4-1a, this gives the relationship

$$\sin\left(\theta_\mathrm{bev}\right) = n_{\mathrm{THz}} \sin\left(\theta_\mathrm{bev} - \theta_\mathrm{bnc}\right) \tag{4.6}$$

Isolating θ_bnc gives the equation

$$\theta_\mathrm{bnc} = \theta_\mathrm{bev} - \arcsin\left[\frac{1}{n_{\mathrm{THz}}} \sin\left(\theta_\mathrm{bev}\right)\right] \tag{4.7}$$

while isolating θ_{bev} gives the equation

$$\tan\left(\theta_{\text{bev}}\right) = \frac{n_{\text{THz}} \sin\left(\theta_{\text{bnc}}\right)}{n_{\text{THz}} \cos\left(\theta_{\text{bnc}}\right) - 1} \tag{4.8}$$

Backward-propagating THz signal (i.e. propagating in the negative z-direction) is also generated and while not contributing to the buildup, can be observed in the experiment and leads to an interference effect that is described later.

4.2   Fabrication of beveled LN crystals

The starting materials were x-cut 5% MgO-doped LN slabs with $50\,\mu\text{m}$ and $100\,\mu\text{m}$ thicknesses (NanoLN). To create the beveled edge, the slabs were mounted using Scotch tape onto the angled face of a negative epoxy mold (c-axis parallel to polishing plane) which was then filled with prototyping wax (McMaster-Carr). The entire assembly was polished with silicon-carbide grinding paper with a minimum grit size of $9\,\mu\text{m}$ at which point the beveled surface of the crystal appeared optically smooth under an optical microscope. The polished LN slabs were slowly heated to 200°C in a box furnace, at which point the melted prototyping wax was drained from the mold. The LN slab was removed from the epoxy mold and then submerged in SP-28 wax remover (MachinableWax.com) at 200°C for a few hours to remove any residual prototyping wax and tape adhesive. The LN slabs were left to cool to room temperature under ambient conditions and then rinsed with isopropyl alcohol to clean off the wave remover. Representative SEM images of the final beveled LN slab are shown in Fig. 4-1c. For the THz measurements, the LN slabs were fixed at the edges to a copper mount with a rectangular aperture such that the slabs were effectively free standing.

4.3   Measuring the THz buildup

Optical measurements were made using the $1\,\text{kHz}$ repetition rate output of a Ti:Sapphire regenerative amplifier providing $1.5\,\text{mJ}$ pulses centered at $800\,\text{nm}$ with $100\,\text{fs}$ duration. The output was split 95:5 into pump and probe respectively. The

pump was attenuated to an overall pulse energy of $200\,\mu\text{J}$ and an optical chopper running at $500\,\text{Hz}$ was used to modulate the pump for electro-optic (EO) sampling. Fig. 4-1b shows an illustration of the experimental geometry at the LN slab. The pump was polarized parallel to the LN c-axis and focused onto the bevel with a 20-cm cylindrical lens. The pump was incident normal to the slab face (oblique to the beveled face) at an angle θ_{bev} and refracted into the crystal at an angle θ_{bnc}. The THz field was measured by EO sampling directly in the LN slab. This method of detection is typical for LN waveguide THz measurements, and has been described elsewhere [48]. The probe beam was frequency-doubled in a β-barium borate (BBO) crystal and then polarized $45°$ relative to the optic axis of LN before being focused onto the back face of the sample with a 15-cm lens. After passing through the sample, the probe was separated from the pump beam path with a dichroic mirror, then directed through a quarter-wave plate and a Wollaston prism and detected on two balanced photodiodes. A delay stage in the pump line was used to scan the pump-probe delay. To measure the THz buildup, the probe position was shifted in the z-direction in $25\,\mu\text{m}$ increments from a starting distance of $100\,\mu\text{m}$ to a maximum distance of $3\,\text{mm}$ away from the bevel.

Because the thickness of the LN slabs used in our experiments is comparable to the wavelengths of THz light confined in the slabs, the THz field propagates in dielectric waveguide modes which are the electromagnetic eigenmodes for a high-index core (LN) sandwiched between layers of a low-index cladding (air). Both transverse electric (TE) and transverse magnetic (TM) modes are supported. (See Section 3.2 for more details.) Since OR is mediated by the d_{33} element of the second-order nonlinear tensor of LN, the optical pump and the excited THz field are both polarized along the optic axis (c-axis) of LN, which results in efficient excitation of TE modes for our geometry.

Dielectric waveguide modes are characterized by dispersion that transitions smoothly from cladding-like to core-like as the wavelength decreases (as depicted in Fig. 4-2b). As it propagates through the slab, the broadband THz pulse disperses with low frequencies leading high frequencies. Over the course of their interaction,
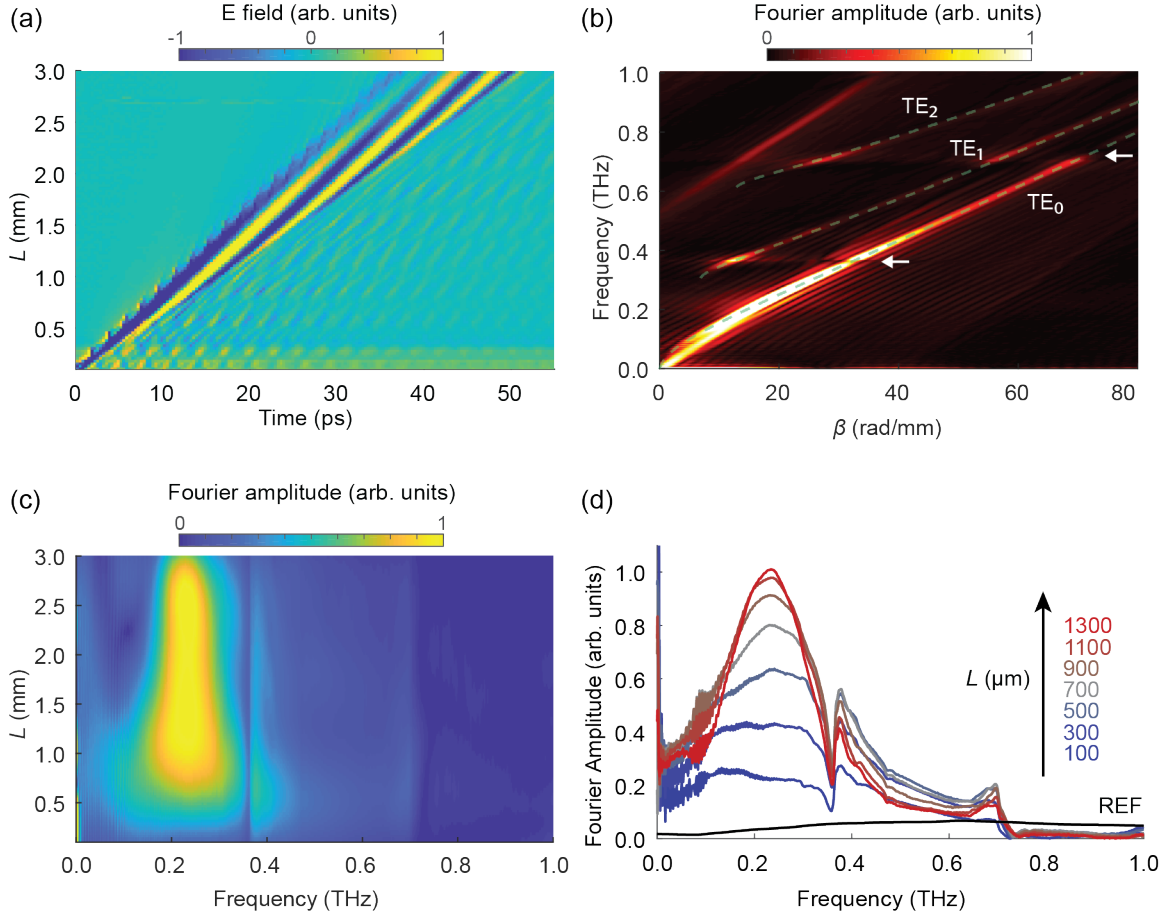
Figure 4-2: **THz buildup using a beveled LN slab.** Data and buildup plots obtained for Sample III. (a) Space-time plot of raw data. (b) Dispersion plot obtained by 2D Fourier transform of data in (a). Calculated dispersion curves for TE_0, TE_1, and TE_2 dielectric waveguide modes are shown by the dashed curves. White arrows indicate spectral modulations caused by backward-propagating THz waves. (c) Surface plot of THz buildup. (d) 2D plot of THz buildup with selected probe positions shown. Reference spectrum is shown in black.

waveguide dispersion creates a velocity mismatch between the optical pump and THz frequency components that either lag behind or lead it. The result is a narrowing of the THz bandwidth over the course of the buildup. By changing θ_{bnc}, the buildup center frequency can be tuned. For our experiments, θ_{bnc} was chosen to match a selected frequency in the TE_0 mode since this is where the majority of the THz energy resides.

To measure the THz buildup, the probe position was shifted in the z-direction in $25\,\mu\mathrm{m}$ increments from a starting distance of $100\,\mu\mathrm{m}$ to a maximum distance of $3\,\mathrm{mm}$

Sample	d (μm)	θ_{bev} (deg)	f_0^{theo} (THz)	f_0^{meas} (THz)	$L_{\max}$(mm)	$\bar{\eta}$	η_0
I	50	59	0.52	0.50	1.4	35.9	10.8
II	50	53	0.78	0.61	0.9	98.4	13.7
III	100	59	0.26	0.23	1.0	79.2	29.2
VI	100	53	0.40	0.38	0.5	69.9	12.8
V	100	50	0.57	0.46	0.6	113.8	13.4

Table 4.1: **Enhancement values and buildup center frequencies.**

away from the bevel. Fig. 4-2a shows a representative raw space-time plot, with the corresponding dispersion plot shown in Fig. 4-2b. In order to better visualize the buildup in the TE_0 mode, we isolated the portion of the dispersion curve that corresponds to the TE_0 mode using a super-Gaussian window function W_β of the form

$$W_\beta (f) = \exp\left[-\left(\frac{f - f_0}{2.25\Gamma_{\text{FWHM}}} \right)^{20} \right] \tag{4.9}$$

where f_0 is the center frequency of the Lorentzian fit and Γ_{FWHM} is the full width at half maximum of the Lorentzian fit. The parameters for W_β were determined by fitting the TE_0 peak to a Lorentzian function for each constant wavenumber slice of the dispersion curve to extract the width Γ_{FWHM} and center frequency f_0. A representative wavenumber slice showing the Lorentzian fit and the super-Gaussian window function is shown in Fig. 4-3. The windowed dispersion was then obtained by multiplying the raw THz spectrum at each constant wavenumber slice by the window function $W_\beta (f)$. The spatial buildup plot shown in Fig. 4-2c was then obtained by inverse Fourier transforming over the β-axis of the isolated TE_0 dispersion. Fig. 4-2d shows THz spectra at selected probe locations from the data in Fig. 4-2c. The THz buildup was measured in five samples with different combinations of thickness and bevel angle chosen to match a particular THz frequency. In each case, the pump bounce angle was matched to a frequency of the TE_0 mode. Sample parameters and experimental results are summarized in Table 4.1.

Room-temperature buildup plots for each of the five samples are shown in Fig. 4-4. For each sample, there is a monotonic increase in the THz spectral amplitude over an average buildup distance of $L \approx 1.1\,\text{mm}$, with an average amplitude enhancement
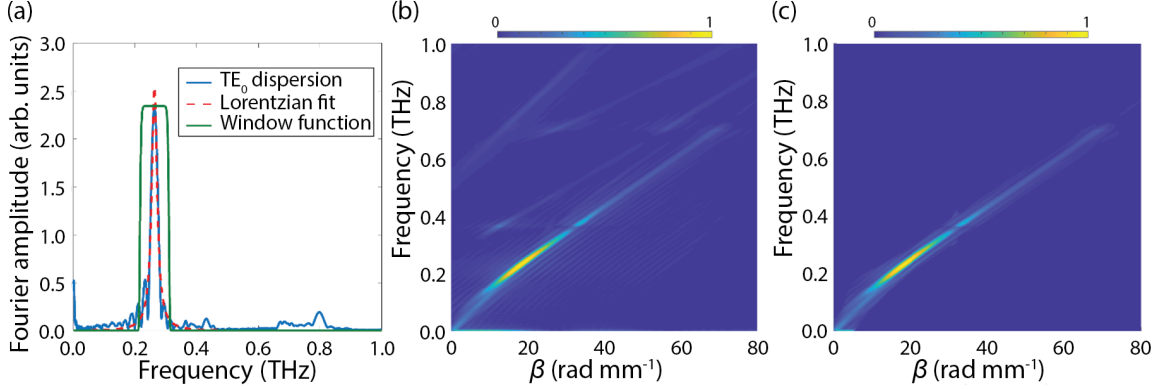
Figure 4-3: **Isolation of the TE$_0$ mode dispersion.** (a) Constant wavenumber slice of THz dispersion at $\beta = 21.5$ rad/mm (blue). Lorentzian fit is indicated by the red dashed line, and the super-Gaussian window function is shown in green. Note: For viewing convenience, the window function has been scaled to the TE$_0$ peak maximum, but the actual peak value of the window function is 1. (b) Dispersion plot obtained by 2D Fourier transformation of raw space-time data. (c) Cropped TE$_0$ dispersion obtained by multiplying the dispersion plot in (b) by the window function obtained from the Lorentzian fitting procedure shown in (a) for every wavenumber.

of 11× relative to the reference trace at the buildup center frequency.

For each sample configuration, we see significant buildup of spectral amplitude in the TE$_0$ waveguide mode of the LN slab, which we attribute to a prolonged interaction with the pump beam facilitated by the TIR geometry. For 50-µm thick samples I and II, the pump bounces 48 times (24 back-and-forth traversals) on average before reaching the peak buildup, while for 100-µm thick samples III–V, the peak buildup occurs after 29 bounces of the pump on average. The buildup center frequency is determined by the bevel angle and the sample thickness and generally agrees with the value expected from velocity-matching considerations. However, we see a slight deviation for samples II and V from the predicted buildup center frequency f_0^{theo} in both simulation and experiment. We attribute this difference to interference with backward-propagating THz waves, which gives rise to sharp modulations in the buildup spectra that overlap with f_0^{theo}, thereby shifting the observed buildup frequency. A further discrepancy could also arise due to the increasing THz absorption in LN with increasing frequency. In this case, the buildup process is balanced against the frequency-dependent THz absorption. This would explain the observation that
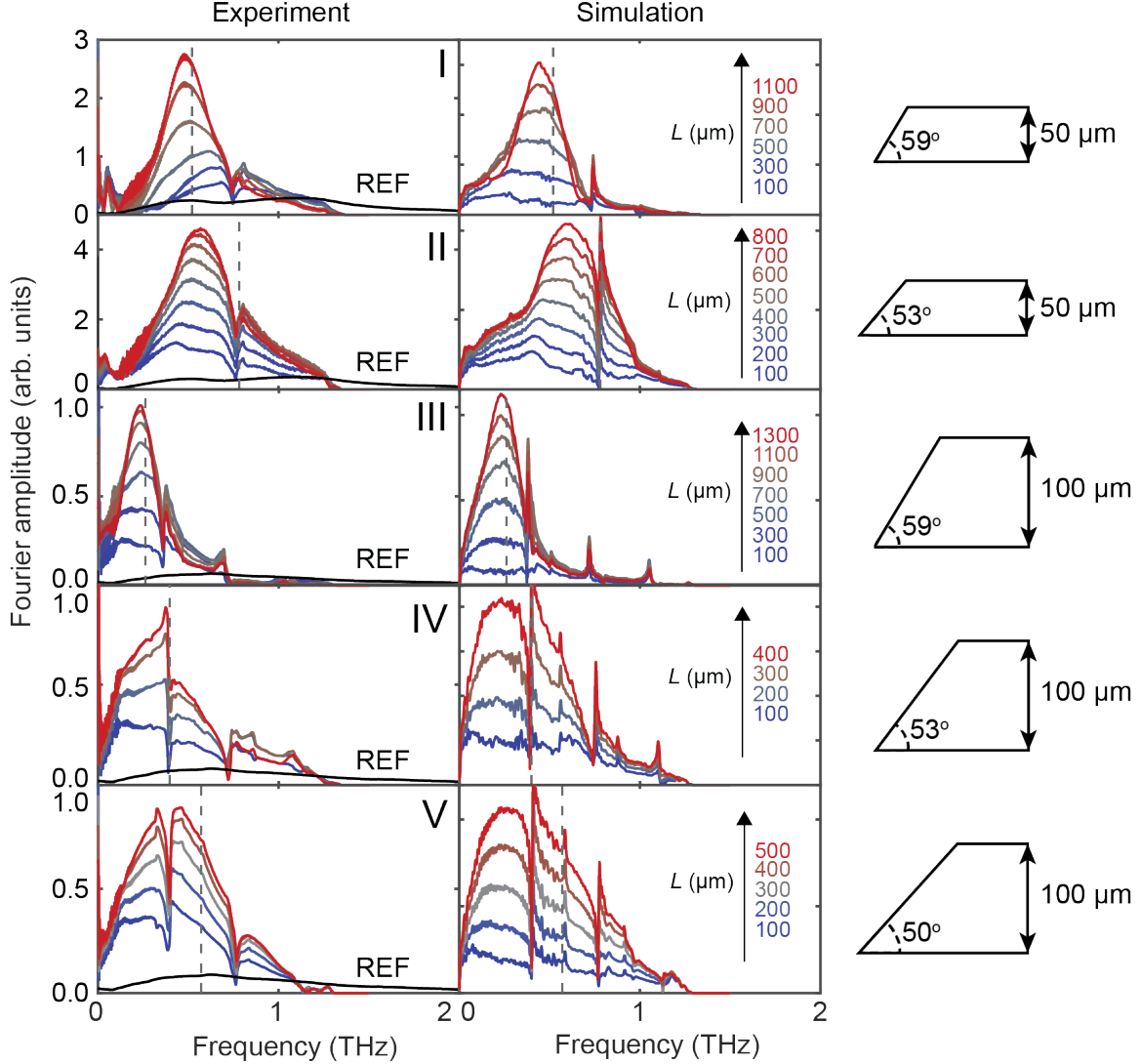
Figure 4-4: **Room temperature THz buildup.** Buildup of THz spectral amplitude from both experiment and simulation at room temperature. The corresponding sample for each row of plots is shown on the right. The theoretical buildup frequency is marked by the vertical grey dotted line in each plot. The legend for each plot gives the selected buildup distances L from $L = 100\,\mu m$ to $L = L_{max}$.

as f_0^{meas} increases, the disagreement between f_0^{meas} and f_0^{theo} generally increases.

Sharp spectral modulations that appear in the THz spectra can be seen at ~ 0.75 THz in samples I and II and at ~ 0.37 THz and ~ 0.75 THz in samples III–V. The modulations are present even after isolating the TE_0 mode. In the FDTD simulation, it can be seen that backward-propagating THz waves (THz waves generated by the optical pump but traveling initially in the opposite direction of the optical pump) form a

zig-zag pattern that reflects from the bevel, creating a train of reflected pulses that follow the main pulse shown in Fig. 4-5. The periodicity of this pulse train gives rise to the sharp modulations in the spectrum that can be seen in Fig. 4-4, and which are indicated by the white arrows in Fig. 4-2b. The pulse train gives rise to a relatively flat (constant frequency) dispersion feature that crosses the TE_0 mode dispersion at the frequencies indicated above. This dispersion feature results from the fact that the periodicity of the pulse train is not a function of the actual THz frequency content of the THz waves forming the pulse train, but rather of the geometry of the optical pump trajectory. The pulse train can be represented by a Fourier series with frequencies given by

$$f_m = \frac{m}{T} \tag{4.10}$$

where T is the temporal spacing between successive reflections (labeled R1, R2, and R3 in Fig. 4-5) and m is an integer. T can be calculated using

$$T = \frac{\Delta x}{v_x} \tag{4.11}$$

where Δx the pump lateral displacement after one back-and-forth traversal and v_x is the lateral velocity of the backward-propagating THz. Δx and v_x can be related to the bounce angle θ_{bnc} using

$$\Delta x = 2d \sin\left(\theta_{\mathrm{bnc}}\right) \tag{4.12}$$

$$v_x = \frac{c}{n_{\mathrm{LN}}} \cos\left(2\theta_{\mathrm{bnc}}\right) \tag{4.13}$$

The frequencies of the first and second-order terms of the Fourier series for a sample with $100\,\mu\mathrm{m}$ thickness are found in this way to be $f_1 = 0.36\,\mathrm{THz}$ and $f_2 = 0.72\,\mathrm{THz}$, For samples with $50\,\mu\mathrm{m}$ thickness, the period T is halved giving first and second-order terms $f_1 = 0.72\,\mathrm{THz}$ and $f_2 = 1.43\,\mathrm{THz}$. These calculated frequencies match well with the observed frequency dips $f_1 = 0.37\,\mathrm{THz}$ and $f_2 = 0.75\,\mathrm{THz}$ for the $100\,\mu\mathrm{m}$ thick samples and $f_1 = 0.75\,\mathrm{THz}$ for the $50\,\mu\mathrm{m}$ thick samples.

Further narrowing of the THz spectrum continues even after the buildup peaks. This can be seen clearly in Fig. 4-2c and Fig. 4-4. The narrowing indicates that
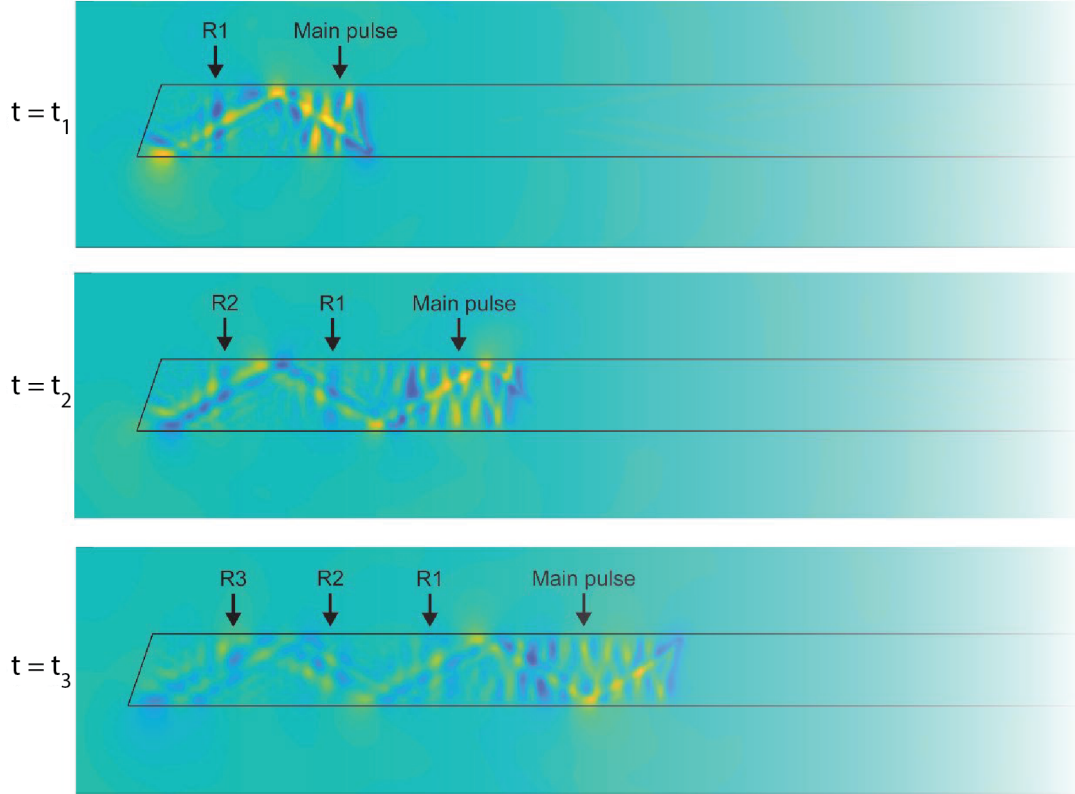
Figure 4-5: **Pulse train simulation.** Pulse train formed from reflections of backward traveling THz waves from the beveled edge of the LN slab shown at three selected time points. Reflections from successive upward slanting portions of the backward traveling wavefront are denoted as R1, R2, R3, which can be seen lagging behind the main pulse.

although the pump continues to generate new cycles of the THz field, the conversion efficiency has diminished to the point that THz absorption reduces the overall THz energy at a higher rate than new THz signal is generated.

To quantify the extent of the enhancement, the buildup traces are compared to a reference that was collected by line-focusing the pump onto a portion of the LN slab that was not beveled and measuring the THz signal generated by a single pass of the pump through the slab. The reference was measured in this way to match previous THz polaritonics experiments [31, 48]. Note that the reference was collected with the pump at normal incidence to the face of the sample, while the sample measurements were collected with the pump at an angle of incidence on the bevel equal to θ_{bev}. To correct for the resulting differences in Fresnel reflection and pump fluence, the

reference THz spectrum is scaled using

$$\tilde{E}_{\text{ref}}(\omega) = \alpha_{\text{Fresnel}}\alpha_{\text{fluence}}E_{\text{ref}}(\omega) \tag{4.14}$$

where $\tilde{E}_{\text{ref}}(\omega)$ is the corrected reference spectrum, $E_{\text{ref}}(\omega)$ is the raw reference spectrum, and α_{Fresnel} and α_{fluence} is the scaling factor for Fresnel reflection and pump fluence considerations respectively. These can then be expressed as

$$\alpha_{\text{Fresnel}} = \frac{1 - R_{\theta_{\text{bev}}}}{1 - R_0} \tag{4.15}$$

$$\alpha_{\text{fluence}} = \frac{A_0}{A_{\theta_{\text{bev}}}} = \frac{\cos(\theta_{\text{bev}})}{\sqrt{1 - \dfrac{1}{n_{\text{LN}}^2}\sin^2(\theta_{\text{bev}})}} \tag{4.16}$$

where $R_{\theta_{\text{bev}}}$ (R_0) is the power reflection coefficient and $A_{\theta_{\text{bev}}}$ (A_0) is the pump spot size at $\theta_{\text{inc}} = \theta_{\text{bev}}(0°)$. n_{800} is the extraordinary refractive index of LN at 800 nm. The reference spectrum is shown in Fig. 4-4 as the solid black curve in each of the experimental plots. In calculating the enhancement, we consider both the integrated enhancement,

$$\bar{\eta} = \frac{\int_0^\infty n_{800}(f)\,|E(f)|^2\,df}{\int_0^\infty n_{800}(f)\,|E_{\text{ref}}(f)|^2\,df} \tag{4.17}$$

as well as the maximum amplitude enhancement,

$$\eta_0 = \frac{E(f_0^{\text{meas}})}{E_{\text{ref}}(f_0^{\text{meas}})} \tag{4.18}$$

where f_0^{meas} is the experimental buildup center frequency. $\bar{\eta}$ measures the enhancement in total THz energy over all frequencies and is approximately proportional to the overall THz generation efficiency (see Fig. 4-8), while η_0 measures the enhancement in amplitude at the buildup center frequency. Maximum values of $\bar{\eta}$ and η_0 are reported for each sample in Table 4.1 and are plotted as a function of buildup distance L in Fig. 4-6. The peak buildup distance L_{max} as given in Table 4.1 is the distance at which η_0 is maximized.
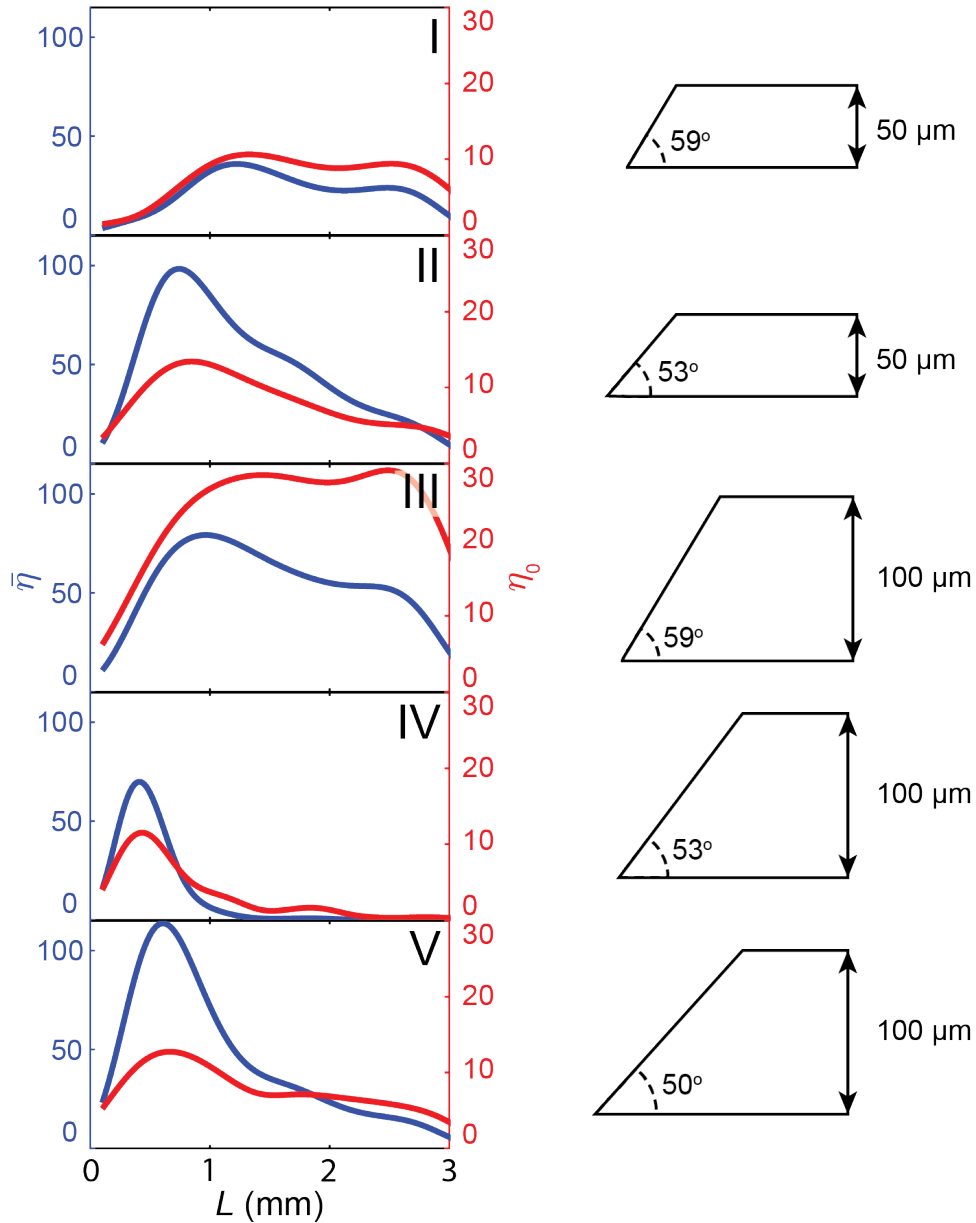
Figure 4-6: **Integrated enhancement and enhancement at the buildup frequency.** Integrated enhancement ($\bar{\eta}$) in blue and enhancement at the buildup center frequency (η_0) in red plotted for each sample as a function of buildup distance (L). Sample thickness and angle are shown in the diagram to the right of each plot.

4.4 Simulating the THz buildup

Saturation of the THz buildup occurs as a result of pump depletion, dispersion, and THz absorption [114]. In order to better understand the roles of these processes in the multi-bounce THz generation method, finite-difference time-domain (FDTD) simula-

tions were performed. The optical pump was treated as a moving point source that followed the back-and-forth trajectory shown in Fig 4-1a. The THz field emitted by each point source at each time step was calculated using a one-dimensional numerical simulation of the coupled optical/THz wave equations, following the method of Ravi et al. [115]. The coupled THz and optical wave equations were solved in one spatial dimension (the direction of THz propagation) while accounting for the different depletion mechanisms at play (optical rectification, 2,3-photon absorption, etc.) using the Runge-Kutta method. The integrated enhancement $\bar{\eta}$ is plotted as a function of buildup distance L in Fig. 4-7, along with calculated generation efficiency curves with progressing levels of included depletion mechanisms. As can be seen from the plot, the processes that limit THz generation most strongly are pump beam divergence and 3-photon absorption. The Rayleigh range for the pump beam (assuming a beam waist of $15\,\mu m$) is $\sim 0.9\,mm$. Initially, divergence of the pump beam results in a drop in the pump intensity, which reduces the OR efficiency. After many reflections of the pump, some wavevector components of the diverging beam deviate significantly from the bounce trajectory, which leads to further degeneration of the nonlinear process. In contrast, the limiting mechanism for the classic TPF generation scheme is a combination of grating-induced angular dispersion and OR-induced repeated red-shifting of the pump spectrum [115]. One reason that pump red-shifting plays a less significant role here is THz spectral narrowing due to waveguide dispersion described earlier. Narrowing of the THz spectrum leads to a field with multiple cycles that is spatially more delocalized than a single-cycle field, and therefore interacts with the pump less strongly. The fact that pump beam divergence is a primary limiting factor in saturation of THz buildup suggests that improvements could be made by focusing the beam less tightly (while keeping pump fluence constant). This, in turn, is limited by the bevel aperture. The effective aperture width could be enlarged by directing the pump light into the bevel at normal incidence, though this is more difficult to execute in practice than using refraction as in the present work. Ultimately the pump beam width would be limited by wavevector considerations, i.e. the wavevector content should include the desired wavevector range in the dispersion curves shown in
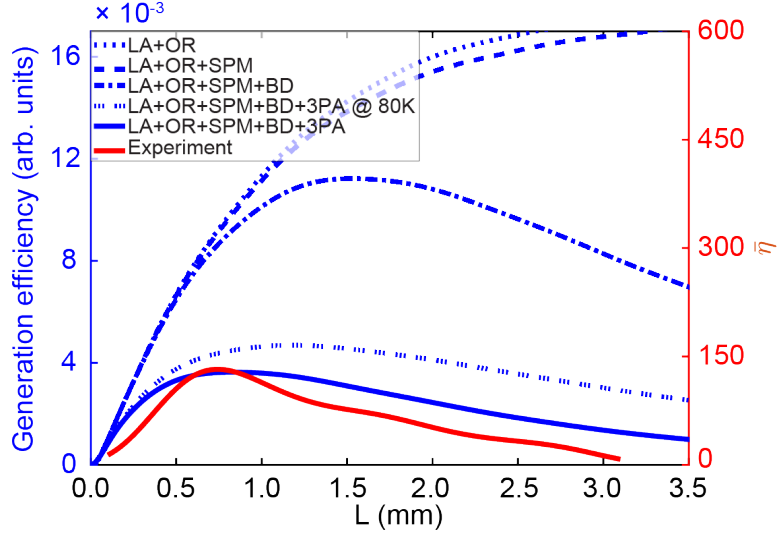
Figure 4-7: **Comparison of generation efficiency for different combinations of depletion mechanisms.** The following mechanisms were considered: linear absorption (LA), optical rectification (OR), self-phase modulation (SPM), pump beam divergence (BD), and 3-photon absorption (3PA). Simulated curves are plotted against the left axis while the experimental integrated enhancement curve is plotted against the right axis. Data shown here are for Sample II ($d = 50\,\mu\text{m}$, $\theta_{\text{bev}} = 53°$).

Fig. 4-2d. Further improvements could be made by using a longer pump wavelength such as the output of an Yb-based femtosecond system to reduce 3-photon absorption [122, 123].

Using the simulations, the optical-to-THz conversion efficiency can be calculated. The overall THz energy was estimated as a function of the distance L using the equation

$$U_{\text{THz}}(L) = \frac{\epsilon_0 c}{2} \int_{-\infty}^{\infty} dx \int_{-\infty}^{\infty} dy \int_{-\infty}^{\infty} dz \; n_{\text{THz}}(\omega) \left| E(x, y, \omega, L) \right|^2 \tag{4.19}$$

$$E(x, y, \omega, L) = E_{\text{EO}}(\omega, L) E_{\text{pump}}(x) E_{\text{wvg}}(\omega, y) \tag{4.20}$$

where c is the vacuum speed of light, ϵ_0 is the vacuum permittivity, n_{THz} is the THz refractive index in LN, $E_{\text{EO}}(\omega, L)$ is the Fourier transform of the EO-sampling trace at position L, $E_{\text{pump}}(x)$ is spatial profile of the generated THz (which is proportional to the intensity profile of the optical pump in the x-direction), and $E_{\text{wvg}}(\omega, y)$ is the TE$_0$ dielectric waveguide mode profile at frequency ω. The coordinate system used here is

defined in Fig. 4-1b. Here, we assume that the THz wave does not diverge significantly along the c-axis over the course of the buildup and that the instantaneous profile of the THz electric field is proportional to the intensity profile of the optical pump during the generation process. The generation efficiency is calculated by dividing the THz pulse energy $U_{\mathrm{THz}}(L)$ by the optical pump pulse energy $(200\,\mu\mathrm{J})$. The calculated values for the generation efficiency for each sample are shown in Fig. 4-8 along with the experimental values of $\bar{\eta}$. Although the numerical values do not match, the qualitative shape of the curves match remarkably well, which means $\bar{\eta}$ can be used as a proxy for the generation efficiency.

4.5   Summary and future directions

In summary, we have demonstrated 11-fold enhancement of the peak THz spectral amplitude in LN waveguides by using a velocity-matched THz generation scheme based on total internal reflection of the optical pump. The center frequency of the THz buildup can be tuned by changing the bounce angle of the pump. Simulations of experimental results indicate that the primary mechanisms that lead to THz buildup saturation are divergence of the pump beam, which may be improved by focusing the pump beam into the LN slab at normal incidence to the bevel to make full use of the bevel aperture, and three-photon absorption, which could be eliminated by using a longer pump wavelength.

These results represent a relatively simple method for accessing greatly enhanced THz spectral amplitudes for THz polaritonics applications. This could prove useful for enabling linear and nonlinear THz signal processing and spectroscopic measurements in compact experimental geometries. Further enhancement may be possible through the use of optical pump fields that are tailored for difference-frequency mixing at a selected THz frequency [35].
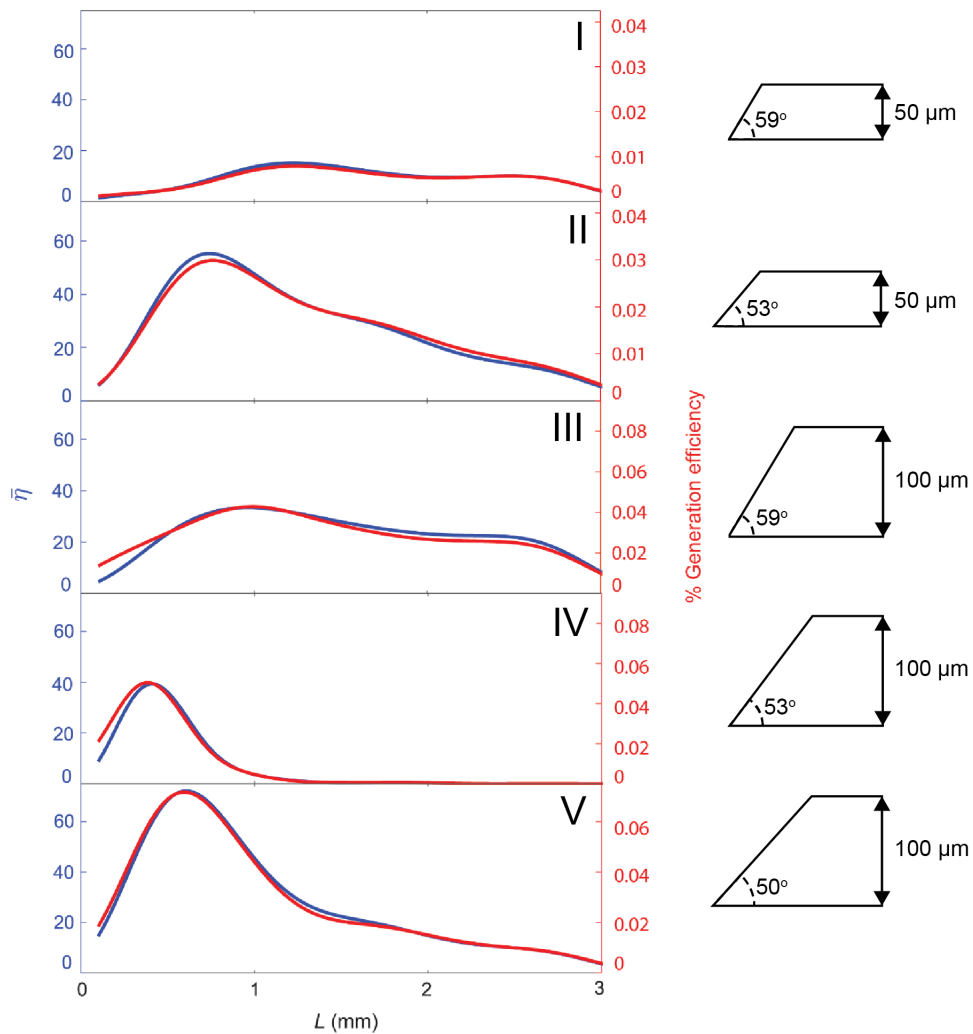
Figure 4-8: **Estimated generation efficiency as a function of buildup distance.**
Comparison with the integrated enhancement factor $\bar{\eta}$ shows that these quantities can
be reasonably treated as proportional to each other. Sample parameters for each of
the plots are given by the corresponding diagram on the right.

Chapter 5

Enhanced THz generation using a conical tilted pulse front

Content adapted from: **E. R. Sung**, Y. Kai, T. Pezeril, K. A. Nelson. "Amplification of terahertz fields in LiTaO$_3$ waveguides using a conical pulse front," *in preparation.*

The THz region of the electromagnetic spectrum has gained much interest due to the access it provides to a wide range of physical processes such as molecular rotations and spin precessions as well as responses of collective modes in solid-state materials [3, 5]. Nonlinear spectroscopic studies in gases [18–20], liquids [21, 22], and solids [23–25] have been conducted. THz fields have been used for control over the states of condensed matter including recent examples of ferroelectric phase transitions [26, 27], magnetic domain reorientations [28, 29], and electronic/structural phase transitions [30].

The development of tabletop THz sources has been instrumental in the study and control of these phenomena. In the 0.1-1 THz range, the robust electro-optic material lithium niobate (LiNbO$_3$, LN) has been used for generation of intense freespace THz fields at kHz repetition rates which, when focused, reach or approach amplitudes of 1 MV/cm. High field strengths are reached using pump laser light that is spatiotemporally shaped to form a tilted pulse front [15–17, 97] with the tilt angle adjusted to match the THz phase velocity in order to optimally drive the THz field.

The utility of the THz polaritonics platform for applications in spectroscopy has been limited by the field strengths (roughly 5-10 kV/cm [31]) that can be routinely generated in the waveguide. Several methods have been developed to generate larger field strengths in waveguides. In one study, a tilted pulse front was used, resulting in a 3-fold increase in multi-cycle field strengths [59]. In another study, a conical prism (axicon) was used to shape the pump light into a "circular ring" pattern to generate THz fields that focused to give 6-fold increased single-cycle field strengths in LT [58].

In this chapter, we describe the Terahertz Ring Excitation (TREx) scheme which combines these two approaches by pumping a LT waveguide with a timed sequence of concentric optical rings to generate superposed, converging THz fields. The TREx scheme yields strong fields in a configuration that is compatible with most environments that permit optical access to the waveguide. The method also permits selection of either a strong THz electric or magnetic field component.

5.1 Terahertz Ring Excitation (TREx) scheme

The TREx scheme is illustrated in Fig. 5-1. A concave circular stair-step "echelon" mirror is used to transform an incident pump pulse with a Gaussian spatial profile into a conical discrete tilted pulse front consisting of concentric rings of light which propagate in timed sequence, with the largest-diameter ring first and the smallest-diameter ring last. There is a circular hole at the center of the echelon mirror, which results in a $\sim$15 μm diameter circular region at the center of the rings where there is no pump light. The time between successive rings is determined by the echelon step height. For an echelon mirror with step width W and step height H, the tilt angle φ of the resulting conical tilted pulse front reflected off the echelon mirror is given by

$$\tan(\varphi) = \frac{W}{2H} \tag{5.1}$$

The pump light reflected off the echelon is imaged onto a 50-μm LT waveguide using a zoom lens. After traveling through the zoom lens and entering the LT substrate, the
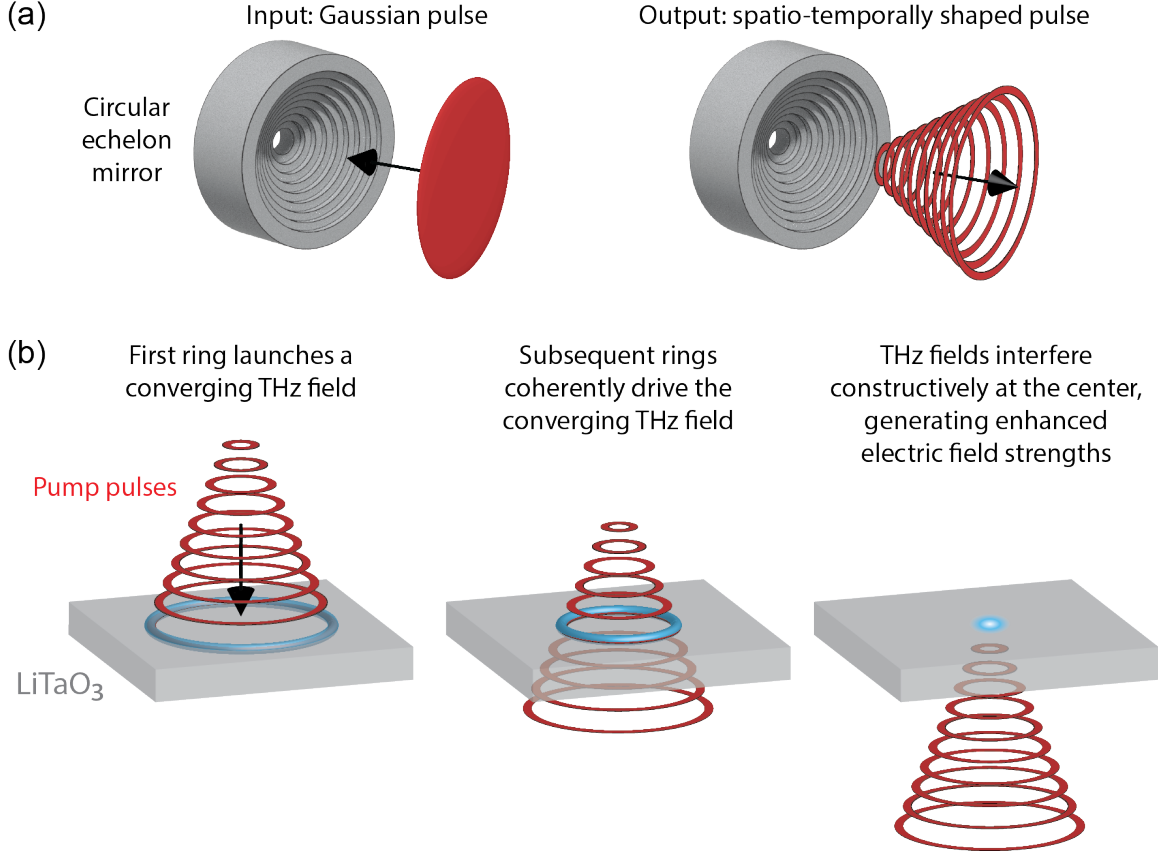
Figure 5-1: **Illustration of the working principles of the TREx scheme.** (a) The echelon mirror transforms a Gaussian pulse into a sequence of concentric rings that form a conical discrete tilted pulse front. (b) Each ring excites a converging and diverging THz field in the LT slab. The converging field is superposed constructively with those generated in succession by the conical pulse front. At the THz focus, the contributions from all the pump rings interfere constructively to give a dramatically enhanced THz electric field amplitude.

tilt angle changes. The zoom lens modifies the radial spacing between rings according to the demagnification M, i.e. $W \to W/M$. In addition, the refractive index n_{800} of LT at the 800 nm pump wavelength modifies the axial spacing between the rings, i.e. $2H \to 2H/n_{800}$. These two effects give a new tilt angle θ in the LT slab given by

$$\tan(\theta) = \frac{W n_{800}}{2HM} \tag{5.2}$$

Each individual pump ring generates converging and diverging single-cycle THz fields. The initial THz field is launched by the largest ring, which arrives at the LT slab first,

and the later pump rings repeatedly drive the converging THz field as it focuses. The driving force is proportional to the pump light intensity (independent of the optical phase) [31], so the speed at which pump light in the conical pulse front moves across the sample, i.e. the lateral scan speed v_{scan}, must match the THz phase velocity v_{ph} to achieve the maximum THz field amplitude. The velocity-matching condition is

$$v_{\text{scan}} = \frac{\Delta x}{\Delta t} = v_{\text{ph}} \tag{5.3}$$

where Δx is the spatial shift between successive rings, i.e. the difference between successive ring radii, at the LT slab and Δt is the difference in arrival time between successive rings. As in the usual tilted pulse front geometry, when the velocity-matching condition is satisfied, the same lobe of the THz field is driven by each pump intensity maximum. Constructive interference along with the enhancement from focusing leads to a dramatic buildup of the THz electric field strength.

The free-space delay between successive pump rings is $\Delta t = 2H/c$ where H is the echelon step height and c is the vacuum speed of light. The spatial shift between successive rings inside the LT slab is $\Delta x = W/M$ where W is the echelon step width and M is the demagnification of the imaging system which is adjusted using a zoom lens. Thus, the velocity-matching condition can be rewritten in terms of the echelon parameters and the demagnification as

$$v_{\text{ph}} = \frac{Wc}{2HM} \tag{5.4}$$

Using the echelon parameters $W = 150\,\mu\text{m}$ and $H = 37.5\,\mu\text{m}$ and the THz extraordinary refractive index in LT $n_{\text{e}} \approx 6.2$ [31], the demagnification required for effective buildup of the THz fields is approximately 12.4.

5.2   Zoom lens

The pump rings are imaged using a zoom lens, which is a three-lens telescope which allows the demagnification M to be tuned over a wide range by moving one of the
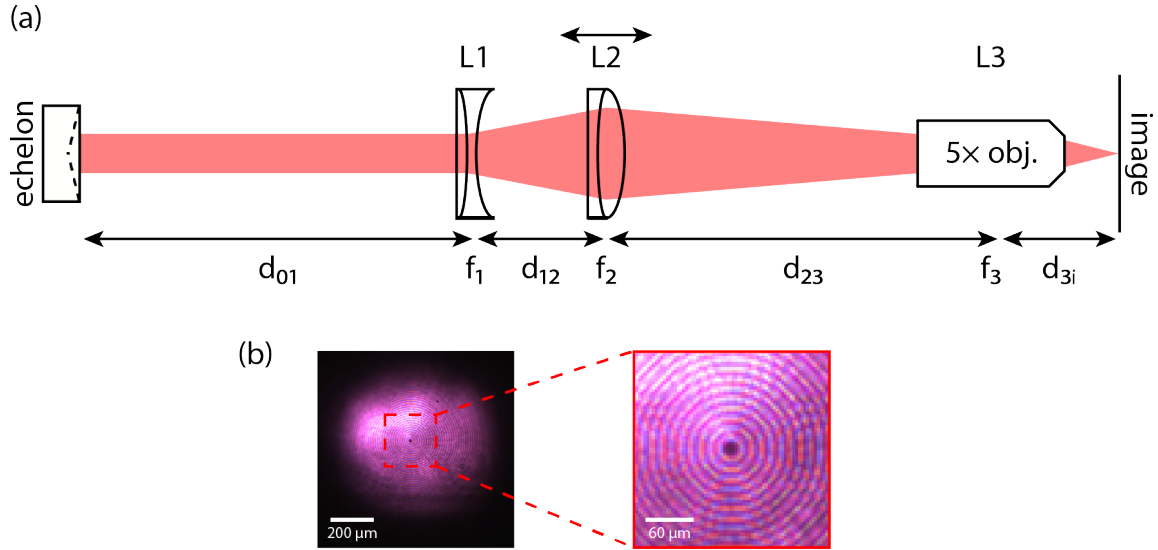
Figure 5-2: **Zoom lens telescope.** (a) Schematic illustration of the zoom lens design. L1 and L2 are achromatic lenses. L3 is a 5× objective lens. The red shaded area represents the beam width as it travels through the zoom lens. In this study, the demagnification was varied by moving the second lens (L2). (b) Image of the pump rings at the image plane. A close-up image near the center of the rings is also shown.

lenses (L2 in this case) without significantly shifting the image position [124]. The configuration used here is illustrated in Fig. 5-2a with initial parameters listed in Table 5.1. In order to minimize aberrations in the imaging system, we used achromatic lenses for L1 and L2 and an objective lens for L3. A representative experimental image of the pump rings taken with a CCD camera placed at the image plane is shown in Fig. 5-2b. A close-up of the image near the center of the rings is also shown. The image shows that a very clear series of concentric rings is formed at the image plane, indicating that any aberrations and distortions in the imaging system that would degrade the quality of the rings are negligible. The echelon mirror has a 200-µm diameter circular hole in the middle which results in a small circular region at the center of the rings where there is no pump light.

The demagnification M of the zoom lens was determined experimentally by imaging the pump rings at the image plane and measuring the spacing between the rings. M was measured at several positions of L2 while keeping the positions of all other optics fixed. For each position of L2, the position of the camera was adjusted to compensate for the slight shift in image position. The experimentally measured values of

parameter	value (mm)	optic
f_1	-100	L1 (concave achromatic lens)
f_2	$+150$	L2 (convex achromatic lens)
f_3	$+40$	L3 ($5\times$ objective lens)
d_{01}	300	–
d_{12}	100	–
d_{23}	350	–
$d_{3\mathrm{i}}$	37.8	–

Table 5.1: **Summary of zoom lens parameters.** The zoom lens was initialized using these values to give a demagnification $M = 12.3$, then adjusted to obtain the desired M.

M are plotted in Fig. 5-3c as a function of the distance d_{12}. By varying d_{12} between 92 and 105 mm, M covers a range from 11.9 to 13.1 (velocity matched to a refractive index range $n = 5.9$ to 6.5). This range includes the optimal value of M predicted by Eq. 5.4, so the velocity-matching condition required for optimal THz generation in LT can be satisfied. In this study we controlled the demagnification by moving L2 and then adjusted the sample position to correct for the slight shift of the image plane. However, any two distances could be used to control the demagnification and image position.

Ray tracing simulations were performed using the ABCD matrix formalism in a home-built MATLAB code to verify the behavior of the zoom lens. In these simulations, principal rays are propagated in the paraxial limit through the telescope, and the image position is determined by calculating where the rays intersect. The individual lenses are treated as ideal lenses. A representative ray tracing diagram output by the program is shown in Fig. 5-3a. A close-up of the ray tracing diagram near the image plane is shown in Fig. 5-3b. Note that the principal rays do not cross the optic axis except in the vicinity of the image plane. Therefore, a beam going through the zoom lens does not focus near any of the lenses, minimizing the risk of damage to the optics.

The demagnification ratio M is calculated from the simulations by comparing the object and image heights. Fig. 5-3c shows the results of the ray tracing simulations calculating the positions of L2 (d_{12}) and the image plane ($d_{3\mathrm{i}}$) for a range of M.
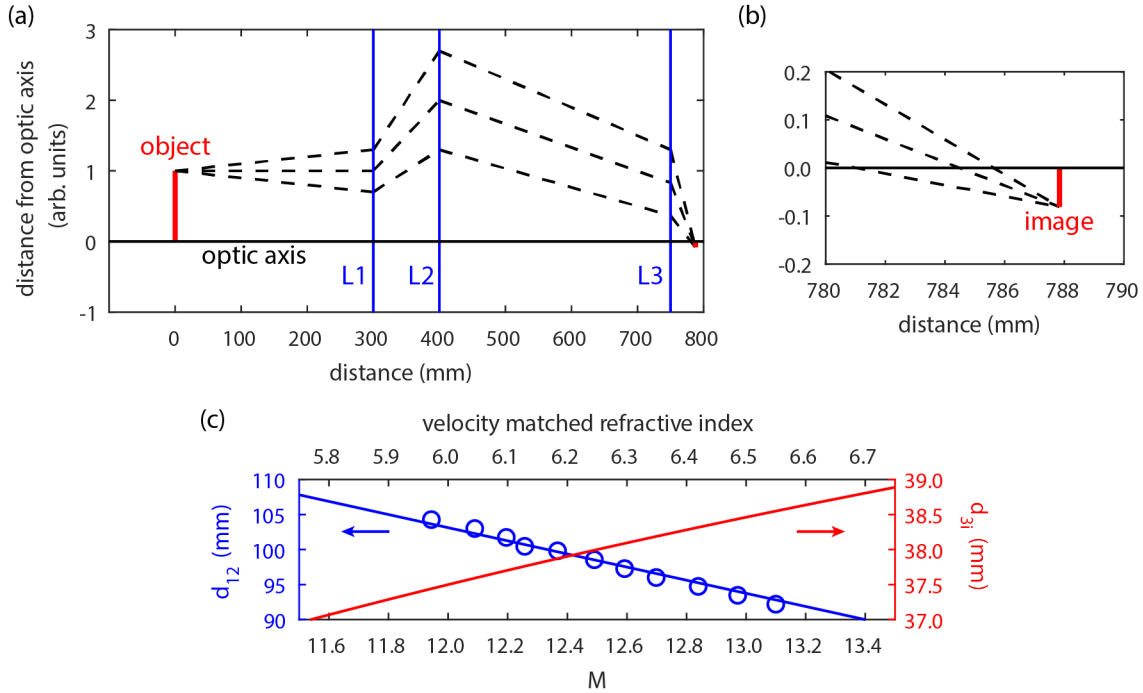
Figure 5-3: **Zoom lens demagnification calculations.** (a) Ray tracing simulation of the zoom lens using the parameters listed in Table 5.1. The calculated demagnification is 12.3. red lines = object/image, black dashed lines = principle rays, blue lines = (ideal) lenses, black solid line = optic axis. (b) Close-up of the ray tracing simulation near the image plane. (c) Plot showing how the distances d_{12} and $d_{3\mathrm{i}}$ vary with the target demagnification. lines = simulation, circles = experiment.

The positions of the other elements (echelon mirror, L1, L3) were kept fixed. The simulations agree well with experimentally measured L2 positions and values of M. The simulations show that over the investigated range of d_{12}, the image plane shifts by about 1 mm. The LT position was shifted to remain in the image plane when THz field measurements were made with different demagnification values.

5.3 Imaging the THz buildup

The performance of the TREx method is characterized by imaging the THz fields as they converge. A schematic illustration of the experimental setup is shown in Fig. 5-4. The output of a Ti:sapphire amplifier system (800 nm center wavelength, 100 fs pulse duration, 4 mJ pulse energy, 1 kHz repetition rate) was split in a 90/10 ratio for the pump and probe pulses. The pump pulse energy was controlled using a half waveplate
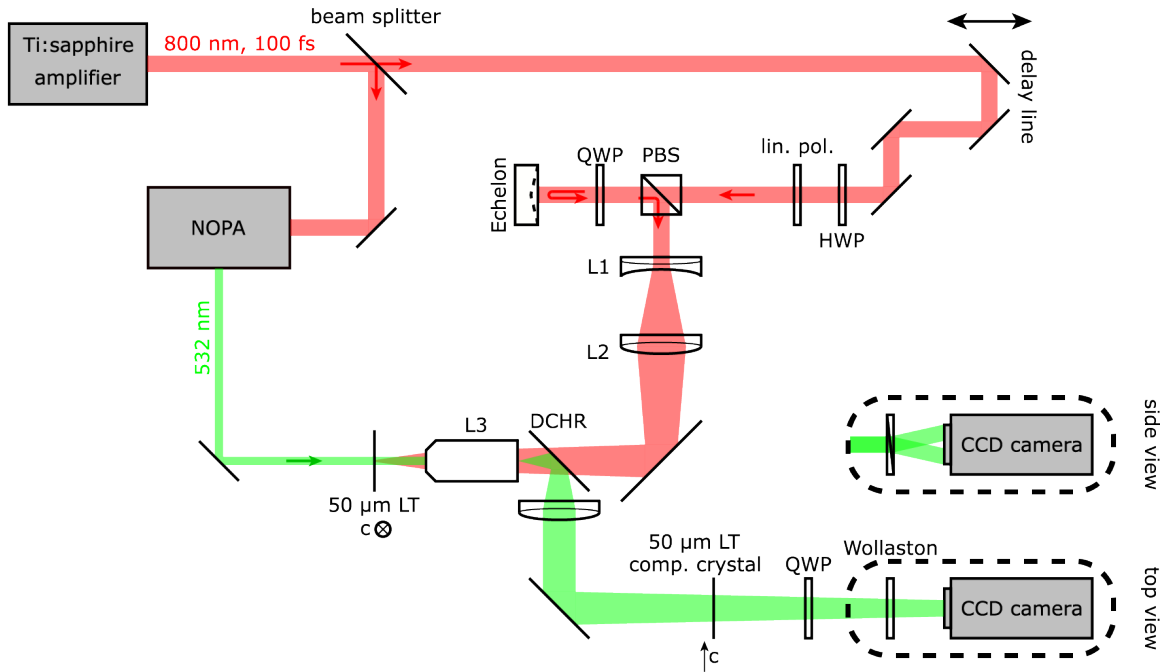
Figure 5-4: **Schematic illustration of the TREx setup.** Abbreviations: PBS = polarizing beam splitter, QWP = quarter-wave plate, HWP = half-wave plate, lin. pol. = linear polarizer, DCHR = dichroic mirror, NOPA = noncollinear optical parametric amplifier.

and linear polarizer. The pump pulses were reflected off of a circular "echelon" mirror (manufactured by Sodick) made of Stavax nickel-phosphorus. The resulting series of pump rings were redirected into the zoom lens using a quarter-wave plate (QWP) and polarizing beam splitter (PBS) and then imaged onto the lithium tantalate (LT) slab. The probe pulses were generated using a noncollinear optical parametric amplifier (NOPA) tuned to output 532 nm pulses. The (collimated) probe pulses were linearly polarized 45° relative to the in-plane LT c-axis, sent through the backside of the LT slab, and then imaged onto a CCD camera using an objective lens (same as used in the zoom lens). A quarter-wave plate and Wollaston prism were placed before the camera to enable electro-optic sampling with balanced detection. A 50-µm LT compensating crystal was also placed before the camera to compensate for the static optical birefringence of LT. The THz electric field strength was quantitatively determined from the electro-optic sampling signal [36] using the calculations described in Section 3.4. A delay stage was used to control the timing between the pump and
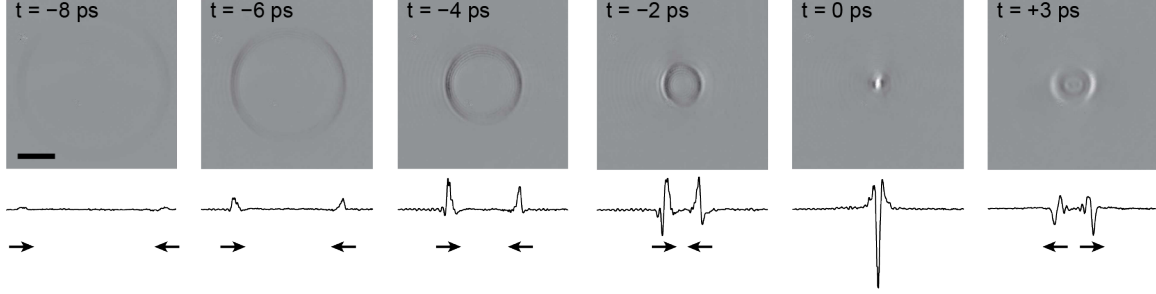
Figure 5-5: **Images of the THz fields.** Top row: Images of the THz field at various times. Scale bar = 200 µm. Bottom row: Line-out plots of the THz field amplitude along a horizontal dashed line going through the THz focus. All line-out plots have the same vertical scale. The arrows indicate the direction of THz field propagation. The time when the THz field is focused is defined as $t = 0$ ps.

probe pulses.

To corroborate the experimental results, simulations of the THz fields were performed with the finite-difference time-domain (FDTD) method using the open-source software package MEEP [125]. The LT slab was treated as an infinite slab in the x and y directions with finite extent in the z direction. Material dispersion was included by using a Lorentzian susceptibility with parameters taken from literature [126]. The in-plane LT c-axis is set along the y-axis in the simulation. Absorbing boundary conditions were used to suppress reflections off the edges of the simulation space. Each pump ring was modeled as a current source with an annular spatial profile. The start time of each pump ring was adjusted to emulate the discrete tilted pulse front in the LT slab.

Fig. 5-5 shows the THz electric field at various times during focusing. At early times, the outer rings launch single-cycle THz fields which increase in amplitude while traveling toward the focus. When the pump light and optical probe overlap in the LT slab, a hyperpolarizability signal appears in the images. This in addition to measurement noise obscures the THz waveform at early times while the peak amplitude is small, resulting in what appears to be a half-cycle THz field. The amplitude of the excited THz fields follow a $\cos^2(\theta)$ angular dependence due to the THz electric field being excited parallel to the LT crystallographic c-axis over the entire ring. When the THz fields reach the focus, there is constructive interference
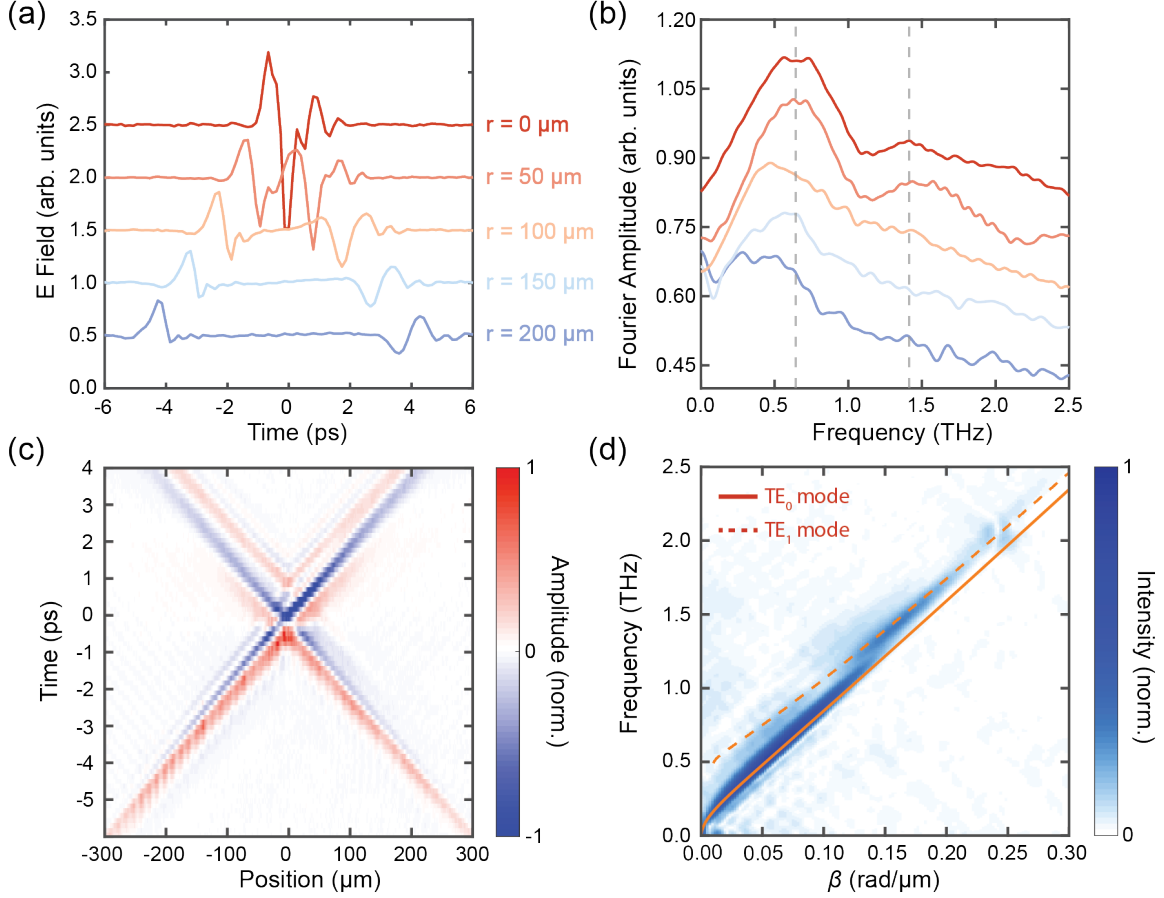
Figure 5-6: **THz field at the focus.** (a) Time traces of the THz field at various distances from the focus. The THz fields reach the focus at t = 0 ps. The pump energy was 225 μJ. Saturation of the THz signal was not observed. (b) THz spectra at the same positions as in (a). For the time traces away from the focus ($r \neq 0\,\mu$m), only the converging THz wave is considered when calculating the spectrum. The plots in (a) and (b) have been vertically offset for clarity. (c) Space-time plot constructed from lineout plots taken through the center of the focus. (d) Dispersion plot obtained from a 2D Fourier transform of (c). The calculated TE_0 (red solid line) and TE_1 (dashed red line) dielectric waveguide dispersion curves are overlaid.

resulting in a dramatically increased THz field amplitude, and the single-cycle THz waveform becomes apparent. The full width at half maximum dimensions of the THz spot at the focus are 30 μm horizontally and 60 μm vertically. After passing through the focus, the THz field diverges and the peak field strength decreases.

Figs. 5-6a,b show the time traces and spectra, respectively, of the focusing THz field at several distances r from the focus. As the THz field focuses, the peak field strength increases due to the individual responses from the multiple pump rings in-

terfering constructively. In addition, the THz spectrum narrows about broad peaks at 0.7 THz and 1.3 THz, suggesting optimal velocity-matching at the two different frequencies. The origin of these two frequencies is clarified by the space-time plot and dispersion plot shown in Figs. 5-6c,d respectively. The space-time plot shows that the pump rings excite two sets of focusing THz fields. The main THz field arrives at the focus at t = 0 ps and a second weaker THz field arrives about 1 ps afterward. The dispersion plot reveals that spectral peaks at 0.7 THz and 1.3 THz correspond to THz fields in the TE_0 and TE_1 dielectric waveguide modes respectively. Due to the slightly different group velocities of the TE_0 and TE_1 waveguide modes, the TE_0 and TE_1 waveguided THz fields focus at slightly different times. Note that the propagation time of the pump light from front to back of the LT slab is $dn_{800}/c = 360$ fs, where $d = 50\,\mu$m is the slab thickness and $n_{800} = 2.157$ is the LT optical refractive index at the 800-nm pump wavelength [127]. The TE_0 mode has no nodes in the plane of the slab, while the TE_1 mode has a node in the center. For frequencies below 1 THz, i.e. field cycles longer than 1 ps, the pump pulse traverses the slab in less than half of a cycle, so the THz response generated by the pump pulse is approximately in phase throughout the slab thickness. For higher frequencies, the THz field generated by the pump pulse near the front of the slab is significantly out of phase with the THz field generated near the back, so the response has a significant TE_1 mode component. A thinner slab would have a TE_0 response that would extend to higher frequencies and a smaller TE_1 mode response. Note also that the imaging of the THz fields depends on the field-induced phase delay of the 532-nm probe light ($n_{532} = 2.207$) [127], integrated through the slab thickness. The opposite signs of the TE_1 mode field in the front and back of the slab diminish the contributions of this mode to the images we record.

5.4   Optimization

In order to optimize the performance of the TREx scheme, we investigated how the THz focusing depends on various parameters. Simulations were performed using the

finite-difference time-domain (FDTD) method with the open-source software package MEEP [125] to determine how material anisotropy and ring ellipticity affect focusing. Experiments were then performed and corroborated by simulations to determine the peak field dependence on the scan speed of the pump rings and the number of pump rings used to excite THz fields.

5.4.1 THz focusing

Simulations were performed to investigate the effect of material anisotropy on the THz focusing. In this study, LT was used due to its very low anisotropy ($n_e \approx 6.2, n_o \approx 6.4$) compared to LN ($n_e \approx 5.1, n_o \approx 6.2$) [31]. This means that a circular ring-shaped THz field will focus much better in LT than in LN. In order to determine how the slight anisotropy of LT affects focusing, simulations were performed by varying the ordinary refractive index n_o while keeping the extraordinary refractive index n_e constant at 6.2. Material dispersion was ignored. A single ring with radius $400\,\mu\text{m}$ was used and the peak THz field strength at the center was recorded.

Fig. 5-7a shows the simulated peak field strength at the focus as the ordinary refractive index n_o is varied. The peak field strength appears to be insensitive to n_o over a range of values from about 6.2 to 6.5. Outside this range, the peak field strength drops quickly due to poor focusing. Contrary to what one might expect, the maximum does not occur at $n_o = 6.2$ (perfectly isotropic). This behavior is due to the Gouy phase shift that occurs for a focusing beam and has been observed previously in focusing THz fields [58]. When each THz half-ring reaches the focus, the phase increases by $\pi/4$. As a result, the THz half-cycle with the maximum field strength becomes slightly offset from the THz focus. When a small amount of anisotropy ($n_o > n_e$) is introduced, the two half rings focus slightly past each other which compensates for the shift from the Gouy phase and improves the overlap between the THz half-cycles. This behavior is illustrated in Fig. 5-7b,c.

In order to compensate for material anisotropy in the waveguide slab, cylindrical lenses can be placed in the zoom lens to shape the pump rings into ellipses rather than circles. The simulations in the previous section were repeated, but with the
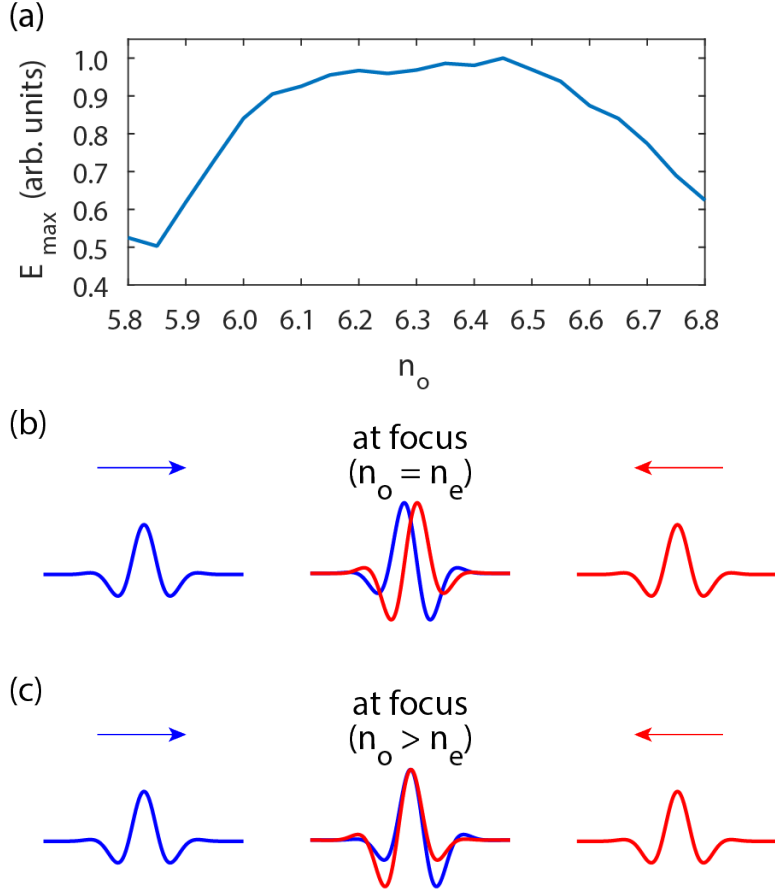
Figure 5-7: **Simulations of THz focusing with varying material anisotropy.**
(a) Simulated peak E field strength at varying values of n_o. (b,c) Sketch showing
the effect of the Gouy phase on the overlap between the two focusing half-rings. (b)
When the half-rings focus in an isotropic medium, the Gouy phase offsets the field
maxima at the focus. (c) When the half-rings focus in a slightly anisotropic medium
where $n_o > n_e$, the overlap of the two half-rings is improved.

pump rings scaled linearly by a factor δ along the y-direction. ($\delta > 1$ corresponds to
stretching the rings.) The pump rings were left unstretched along the x-direction. A
sketch of the simulation geometry is shown in Fig. 5-8a.

The simulation results are summarized in Fig. 5-8b. For every value of n_o, the
value of δ that gives the largest THz electric field at the focus is extracted. As the
ratio n_o/n_e is increased, δ monotonically increases with a slope of approximately
1. This makes intuitive sense because one would expect that the pump rings would
need to be stretched by the ratio of refractive indices to compensate for the material
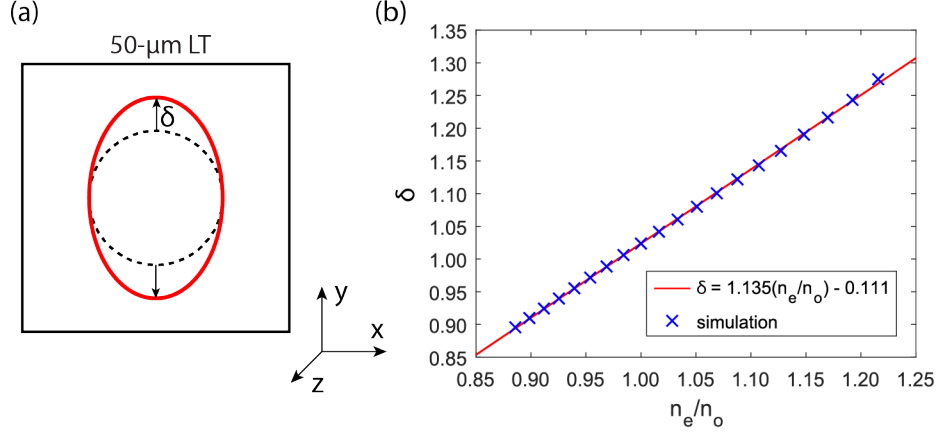
Figure 5-8: **Simulations of THz focusing with varying pump ring ellipticity.** (a) Illustration of the elliptical ring excitation profile. The red ellipse represents the pump ring after being scaled by a factor of δ along the y-direction. (The dashed black circle is the pump ring without scaling.) (b) Plot showing the optimal value of δ at various ratios of $n_{\mathrm{o}}/n_{\mathrm{e}}$.

anisotropy and focus at the center of the elliptical pump region. Deviations from a perfect $\delta = n_{\mathrm{o}}/n_{\mathrm{e}}$ relationship can be explained by the Gouy phase shift, which causes the THz focusing to be optimized when the half-ellipses focus slightly past each other. Therefore, the value for δ should be slightly smaller than $n_{\mathrm{o}}/n_{\mathrm{e}}$. For LT ($n_{\mathrm{e}} \approx 6.2$, $n_{\mathrm{o}} \approx 6.4$), we get an optimal $\delta = 0.99$, which means that the circular pump rings used are very close to optimal. Thus, during the laser experiments we did not insert cylindrical lenses into the zoom lens and simply used the circular rings provided by the echelon mirror. For LN ($n_{\mathrm{e}} \approx 5.1$, $n_{\mathrm{o}} \approx 6.2$), we get $\delta = 0.82$ which indicates that focusing can be significantly improved by adding cylindrical lenses to the zoom lens to shrink the pump rings by 17% along the y-direction.

5.4.2 Scan speed

The peak THz field strength was measured at various pump scan speeds, which were controlled by adjusting the demagnification M of the zoom lens, while the number of rings used was held constant at 30. The demagnification of the zoom lens was adjusted by moving the position of the second lens. The position of the LT slab was then adjusted to place it in the image plane of the zoom lens. The experimental and
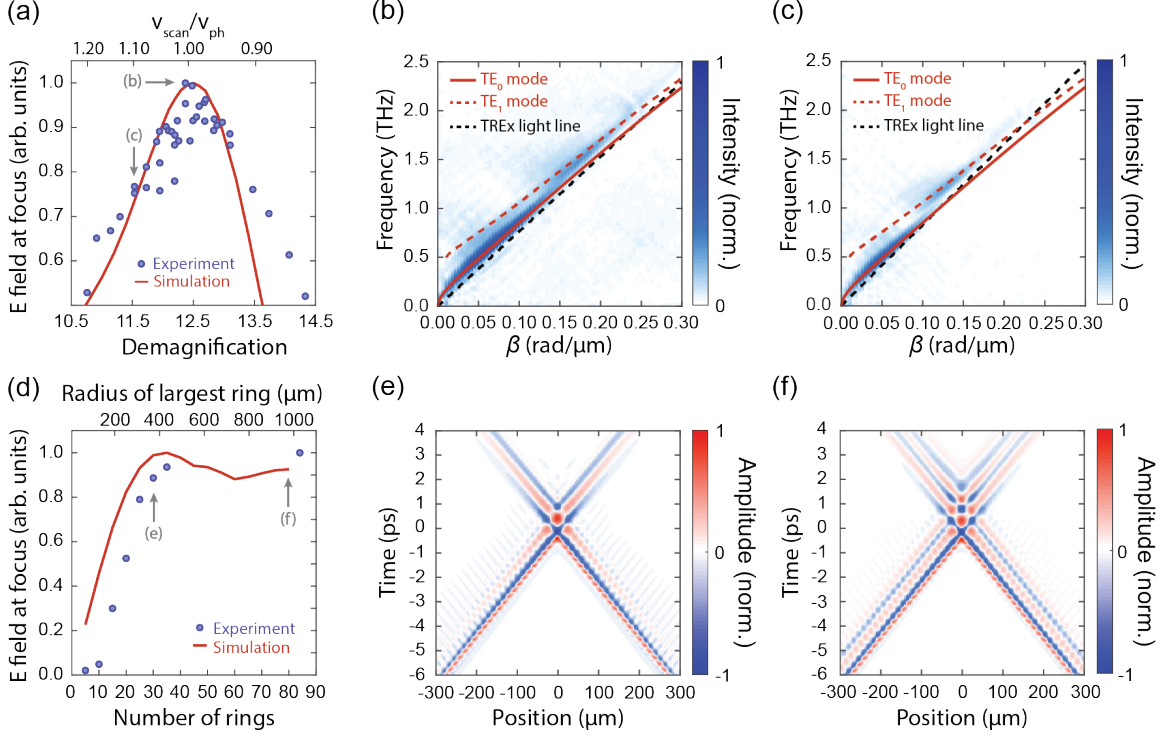
Figure 5-9: **Optimizing TREx performance.** (a) Plot of THz field strength at the focus at varying zoom lens demagnification ratios. (b,c) Dispersion plots showing the spectral content of the THz pulse at the data points labeled in (a). (d) Plot of the THz field strength at the focus at varying numbers of pump rings. (e,f) Simulated space-time plots of the focusing THz field at the data points labeled in (d).

simulated results are shown in Fig. 5-9a. The THz field strength reaches a maximum at $M = 12.4$, which is in good agreement with the predicted demagnification ratio. This behavior can be explained by comparing the dispersion plots at different scan speeds shown in Fig. 5-9b,c ($M = 12.4$ and 11.6). The velocity-matching condition described by Eq. 5.3 is graphically represented in the dispersion plots by the overlaid TREx light line. At optimal velocity-matching, the TREx light line approaches the TE_0 waveguide dispersion curve over a wide frequency range. Although perfect velocity-matching is not achieved for all frequencies, THz fields are still excited over a large frequency range and constructive interference between the many frequency components results in a large peak field strength. When a faster scan speed is used (lower demagnification), the slope of the TREx light line increases and the excited bandwidth is significantly smaller, leading to a lower peak field strength. In

111

both dispersion plots, the TREx scheme also excites TE_1 waveguided THz fields at higher frequencies. However, the curvature of the TE_1 dispersion prevents broadband velocity-matching. Thus, the optimal scan speed is that which optimizes the overlap between the TREx light line and the TE_0 dispersion, which in turn maximizes the excited THz bandwidth.

5.4.3   Number of rings

Next, we optimize the number of pump rings used at constant pump fluence while keeping the demagnification at the optimized value (12.4). The pump beam was expanded using a $3\times$ telescope to illuminate the entire echelon mirror with an approximately flat beam profile. An iris was used to set the beam diameter and the number of pump rings. The iris was placed right before the echelon mirror to minimize diffraction effects. The experimental and simulated results are shown in Fig. 5-9d. The peak THz field strength increases roughly linearly with the number of rings and flattens at 35 rings. Simulated space-time plots of the focusing THz fields using 30 and 80 pump rings are shown in Fig. 5-9e,f respectively. When 35 pump rings are used, the THz field at the focus is single-cycle. However, when using 80 pump rings, more THz cycles appear. This suggests that spatial walkoff limits the number of pump rings that could be used. The walkoff originates from the nonlinear shape of the TE_0 dispersion curve, resulting in a slight difference between the THz phase and group velocities. Because the THz phase velocity is slightly faster than the group velocity, the pump rings (which are velocity-matched to the THz phase velocity) scan slightly faster than the THz pulse speed. As the THz pulse lags behind the pump light, additional lobes appear, with the pump light always driving the leading lobe of the THz field. The optimal number of pump rings can be estimated by considering the walkoff between the pump rings and the excited THz field. Assuming that pump rings only contribute to buildup if they are spatially within one wavelength of the peak of the THz field, we get the condition

$$\frac{2H}{c}\left(v_{\mathrm{ph}} - v_{\mathrm{gr}}\right) n_{\mathrm{rings}} = \lambda_{\mathrm{THz}} \tag{5.5}$$

where n_{rings} is the optimal number of pump rings, λ_{THz} is the THz wavelength in the LT slab, and v_{ph} and v_{gr} are the THz phase and group velocities, respectively. Plugging in the values for v_{ph} and v_{gr} in a 50-µm LT waveguide at $\lambda_{\text{THz}} = 48\,\text{µm}$ (1 THz) gives an estimate of 35 rings, which matches well with the experimental and simulated data.

5.5   Calculating enhancement from focusing

Using the observations from the experimental data, we can build a simple model to estimate the field enhancement when using the TREx scheme. For a single THz ring, the increase in field strength due to focusing can be estimated using a simple argument based on conservation of energy. The energy of a pulse of electromagnetic radiation is given by

$$U = \int \frac{1}{2} \varepsilon\,(x, y, z)\,|E\,(x, y, z)|^2\ dV \tag{5.6}$$

where $\varepsilon\,(x, y, z)$ is the dielectric function, $E\,(x, y, z)$ is the electric field strength, and dV is the volume element. Here, we assume that ε is isotropic, which is approximately true for LT.

Suppose a ring of pump light with radius r_0 and width σ_{r} launches a focusing THz wave. The generated THz electric field is described by the equation

$$E_{\text{ring}}(r, \theta) = E_{0,\text{ring}} \exp\left(-\frac{(r - r_0)^2}{2\sigma_{\text{r}}^2}\right) \left[-\sin\,(\theta)\cos\,(\theta)\,\hat{x} + \cos^2\,(\theta)\,\hat{y}\right] \tag{5.7}$$

where $E_{0,\text{ring}}$ is the peak THz electric field amplitude, and r and θ are the radial and angular coordinates. Assuming $r_0 \gg \sigma_{\text{r}}$, the energy approximately is given by

$$U_{\text{ring}} \propto r_0 \sigma_{\text{r}} E_{0,\text{ring}}^2 \tag{5.8}$$

A similar calculation can be done at the THz focus. Assuming that the THz fields form a Gaussian spot at the focus with peak electric field amplitude $E_{0,\text{focus}}$ and spot dimensions σ_x and σ_y along the x and y Cartesian coordinates, the electric field profile

and energy are approximated as

$$E_{\text{focus}}(x, y) = E_{0,\text{focus}} \exp\left(-\frac{x^2}{2\sigma_x^2}\right) \exp\left(-\frac{y^2}{2\sigma_y^2}\right) \qquad (5.9)$$

$$U_{\text{focus}} \propto \sigma_x \sigma_y E_{0,\text{focus}}^2 \qquad (5.10)$$

Assuming the THz pulse energy decreases exponentially as it propagates, we can write the ratio

$$\frac{U_{\text{focus}}}{U_{\text{ring}}} = \exp(-\alpha r_0) \qquad (5.11)$$

where α is the absorption coefficient. Rearranging gives the following relationship.

$$\frac{E_{0,\text{focus}}}{E_{0,\text{ring}}} \propto \sqrt{\frac{r_0 \sigma_{\text{r}}}{\sigma_x \sigma_y}} \exp\left(-\frac{\alpha r_0}{2}\right) \qquad (5.12)$$

σ_x can be estimated using

$$\sigma_x \approx \sigma_{\text{r}} + D r_0 \qquad (5.13)$$

assuming that the THz pulse broadens at a linear rate D, which can be written in terms of the THz phase and group velocities, v_{ph} and v_{gr}, as follows.

$$D = 1 - \frac{v_{\text{gr}}}{v_{\text{ph}}} \qquad (5.14)$$

The parameter σ_y is a constant determined by the angular dependence of the excited THz fields. The spatial profile of the THz field at the focus can be obtained by decomposing the initially excited THz fields into a sum of planewaves and calculating the interference pattern at the focus. Due to the nearly isotropic THz refractive index in LT, the THz fields propagate directly toward the focus and all arrive with approximately the same phase. The THz field component polarized along the x-axis cancels due symmetry. The y-polarized THz field profile can be calculated as

$$E_y(y) = \int_{-\frac{\pi}{2}}^{\frac{\pi}{2}} \cos^2(\theta) \cos(k_0 y \sin(\theta)) \ d\theta = \pi \frac{J_1(k_0 y)}{k_0 y} \qquad (5.15)$$

where k_0 is the peak THz wavevector and J_n denotes a Bessel function of the first

kind. σ_y is found by solving

$$\pi \frac{J_1\left(\frac{k_0\sigma_y}{2}\right)}{\left(\frac{k_0\sigma_y}{2}\right)} = \frac{1}{2} \tag{5.16}$$

which gives $\sigma_y = 60\,\mu\mathrm{m}$, which agrees very well with the experimentally measured value.

We can estimate the enhancement $\gamma\left(r_0\right)$ from ring focusing with the following equation.

$$\gamma\left(r_0\right) = \frac{E_{0,\mathrm{focus}}}{E_{0,\mathrm{ring}}} \propto \sqrt{\frac{r_0}{1+\frac{D}{\sigma_r}r_0}}\exp\left(-\frac{\alpha r_0}{2}\right) \tag{5.17}$$

For a single ring, the radius that gives the largest enhancement r_{optimal} is then given by

$$r_{\mathrm{optimal}} = \frac{\sigma_r}{2D}\left(\sqrt{1+\frac{4D}{\alpha\sigma_r}} - 1\right) \tag{5.18}$$

Note that in the limit $4D/\alpha\sigma_r \ll 1$, the optimal ring radius is approximately the polariton propagation length α^{-1}.

The enhancement gained by using multiple rings (assuming optimal velocity-matching) can be estimated using a summation weighted by a Gaussian factor to account for walkoff.

$$E_{\mathrm{THz}} = \sum_n \gamma\left(r_n\right)\exp\left[-\left(2\frac{|v_{\mathrm{ph}} - v_{\mathrm{gr}}|}{v_{\mathrm{scan}}}\frac{\left(r_n - r_{\mathrm{optimal}}\right)}{\lambda_{\mathrm{THz}}}\right)^2\right] \tag{5.19}$$

where r_n is the radius of the nth ring.

Fig. 5-10 shows the simulated enhancement for a single ring and a series of rings along with the predictions from Equations 5.17 and 5.19. The curves were calculated using values for the THz refractive index in a 50-µm LT slab ($v_{\mathrm{ph}} = c/5.77$, $v_{\mathrm{gr}} = c/6.58$) and absorption coefficient ($\alpha = 46\,\mathrm{cm}^{-1}$) [126] at $1\,\mathrm{THz}$ ($\lambda_{\mathrm{THz}} = 50\,\mu\mathrm{m}$). The curves agree very well with the simulated results. Furthermore, the curves predict up to a 20-fold increase in the THz field amplitude that saturates at 35 rings, which agrees well with the experimentally observed 18-fold increase.
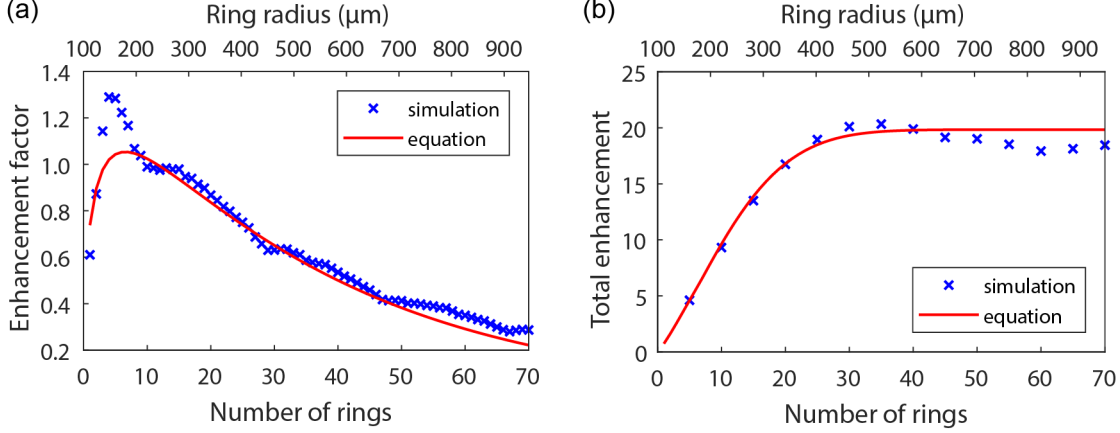
Figure 5-10: **Calculation of THz field enhancement from focusing.** Simulated results of the field enhancement for (a) a single ring and (b) a series of rings. The predictions from Equations 5.17 and 5.19 are overlaid.

5.6 Pump pulse energy dependence

The THz fields were imaged quantitatively via EO sampling following methods previously used with LN waveguides [36]. The relevant equations are summarized in Section 3.4. When the THz field strength is sufficiently large, the signal saturates. Further increasing the THz field strength results in an apparent decrease in signal. Extreme saturation occurs when $\Delta\phi = \pi/2$, which corresponds to a threshold field strength E' of approximately $160\,\text{kV/cm}$.

Overrotation in the EO sampling signal becomes apparent when comparing the THz focus at high and low pump energies, shown in Fig. 5-11a,b. At higher pump energies, a small amplitude modulation appears in the center of the THz focus as shown in Fig. 5-11b. Note that the dimensions of this modulation are much smaller than the THz wavelength in LT ($\lambda_{\text{THz}} \approx 50\,\mu\text{m}$), so it cannot correspond to any real variation in the THz field strength. To correct for overrotation in the experimental power dependence plot, the field strength at the focus is extracted at the same position in the focus and fit according to $E(I) \propto \sqrt{I}\tanh\left(a\sqrt{I}\right)$ [128], where I is the pump intensity and a is a scaling constant. At the overrotation threshold, the slope of the curve will suddenly change sign. Thus, the form of $E(I)$ after accounting for

overrotation would become

$$E\left(I\right) \to E' - \left|E\left(I\right) - E'\right| \tag{5.20}$$

Once the experimental overrotation threshold is determined this way, the data are corrected by inverting the transformation in Equation 5.20. The uncorrected and corrected field strengths are plotted in Fig. 5-11c. The overrotation threshold determined this way is $131\,\mathrm{kV/cm}$, which agrees reasonably well with the predicted value.

Using the optimized parameters for demagnification ($M = 12.4$) and number of pump rings ($n_{\mathrm{rings}} = 35$), the pump energy was increased to determine the maximum observable field strength. The pump energy was adjusted using a half waveplate and linear polarizer. When the pump fluence was above the optical damage threshold of LT at $1\,\mathrm{kHz}$ (approximately $96\,\mathrm{mJ/cm^2}$), the laser repetition rate was reduced to $10\,\mathrm{Hz}$. Fig. 5-12 shows the pump pulse energy-dependence results at room temperature. The peak THz field strength increases monotonically with pump energy, with a decreasing slope at higher pump energies. The optical-to-THz generation efficiency shows a linear increase before saturating at higher pump energies due to self-phase modulation [129] and three-photon absorption [130]. The largest observed field strength achieved with no damage to the LT slab was $175\,\mathrm{kV/cm}$ using $0.56\,\mathrm{mJ}$ of pump energy, corresponding to a 0.0055% conversion efficiency. Since the THz field is generated in a thin LT slab, the total THz pulse energy (and corresponding conversion efficiency) is low compared to what is routinely achieved in a bulk LN crystal [130]. At higher pump energies, there was gradual damage to the surface of the slab. The damage threshold can be increased by lowering the laser repetition rate, which may allow photoexcited carriers to relax between laser shots [131]. When the laser repetition rate was decreased to $10\,\mathrm{Hz}$, we observed several small damage spots that slowly grew with each laser shot at pulse energies $>0.70\,\mathrm{mJ}$. The rate of damage accumulation was slow enough that we could image the THz fields prior to severe damage. The largest observed field strength under these conditions was $300\,\mathrm{kV/cm}$ using $1.3\,\mathrm{mJ}$ of pump energy (0.007% conversion efficiency). We expect that various
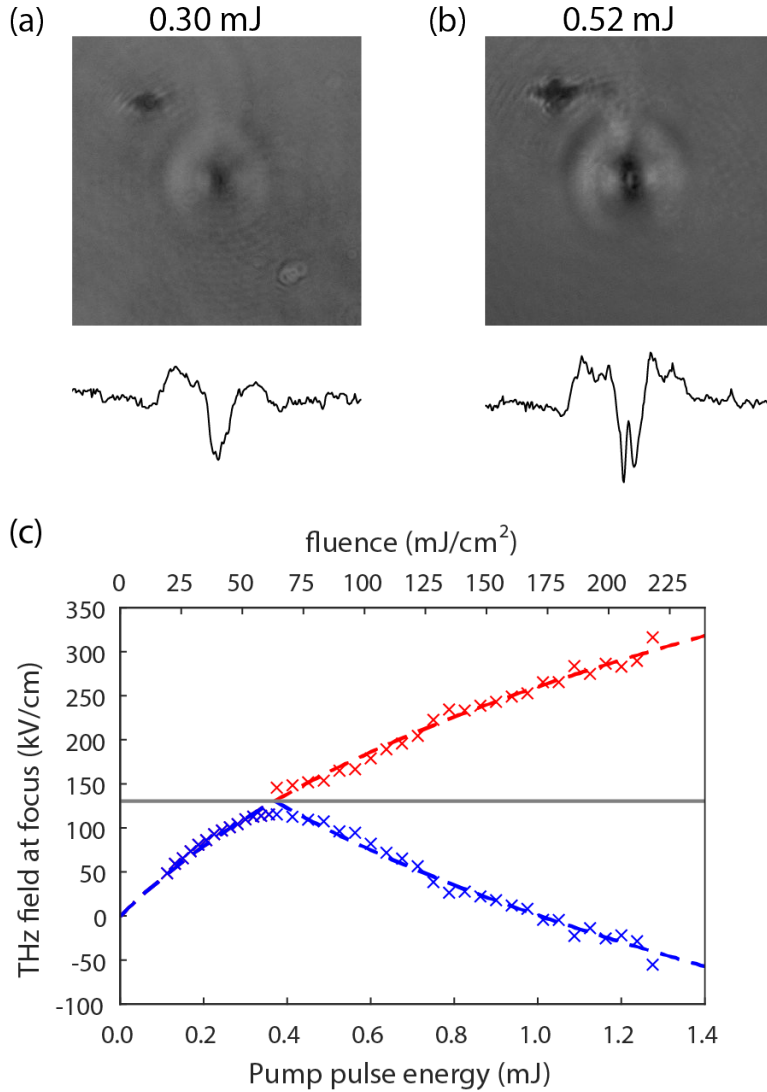
Figure 5-11: **Overrotation in THz signal.** (a,b) Image of the THz focus using (a) 0.30 mJ and (b) 0.52 mJ of pump energy. Below each image is a lineout plot showing the THz field profile along a horizontal line going through the center of the focus. (c) Plot of the pump energy dependence data before (blue) and after (red) correcting for overrotation. The horizontal grey line indicates the estimated overrotation threshold (131 kV/cm). Crosses = experimental data, dashed lines = fit

steps could be taken to further improve the maximum field strength, such as ensuring a dust-proof environment, pumping with a longer wavelength such as 1030 nm at which 3-photon absorption does not take place in LT [123], and using MgO-doped LT which would likely have a higher damage threshold than the undoped LT used here as is well known to be the case for lithium niobate [132].

118
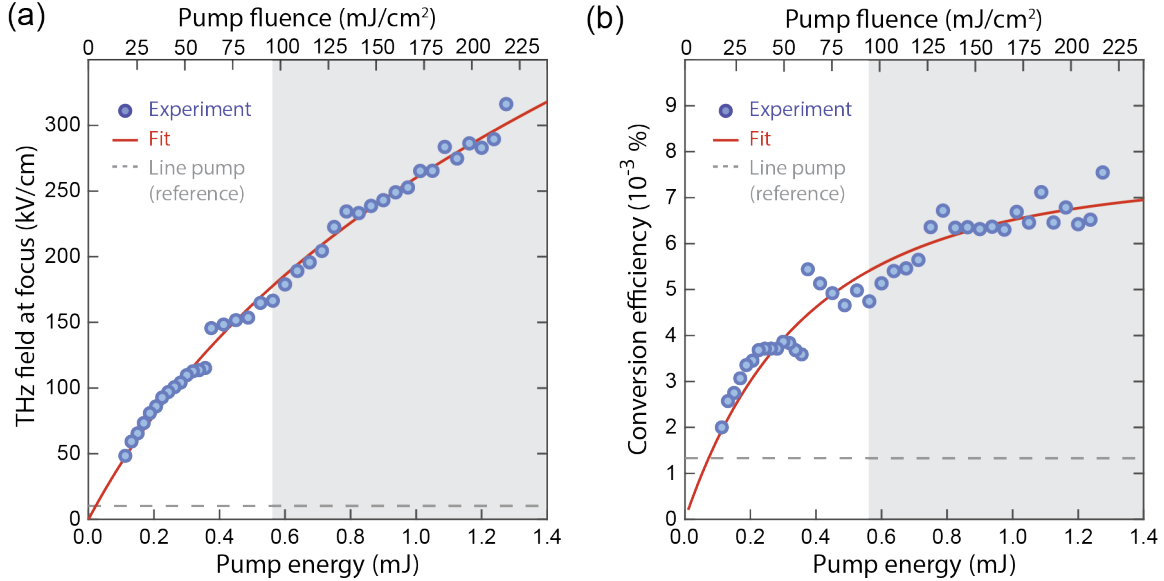
Figure 5-12: **TREx pump pulse energy dependence.** (a) Measured THz field strength at varying pump pulse energies. (b) Calculated optical-to-THz conversion efficiency. The black dashed line represents the field strength and conversion efficiency obtained from a single line-focused pump beam. The grey shaded region indicates pump fluences where the laser repetition rate was reduced to 10 Hz to slow down optical damage to the LT slab.

The TREx results are compared against a reference measurement performed by using a cylindrical lens to focus the pump beam as a line of pump light on the LT slab, as is typically done in a polaritonics experiment. This method generates THz electric field strengths up to 10 kV/cm, measured 100 μm away from the line pump, when the pump fluence is just below the damage threshold [31]. The line pump reference data are represented in Fig. 5-12 as horizontal dashed lines. The TREx scheme produces much larger electric field amplitudes using much lower pump fluences. At the same pump fluence, we observe an 18-fold increase in the THz field strength, a notable increase compared to previous works.

From Fig. 5-9 and 5-12, we see that the peak THz field strength depends approximately linearly on both the number of pump rings and the pump fluence. If the total pump energy is fixed, then a linear increase in the number of pump rings is accompanied by a quadratic decrease in the pump fluence, leading to an overall decrease in peak field strength. Thus, the maximum field strength is found by maximizing the
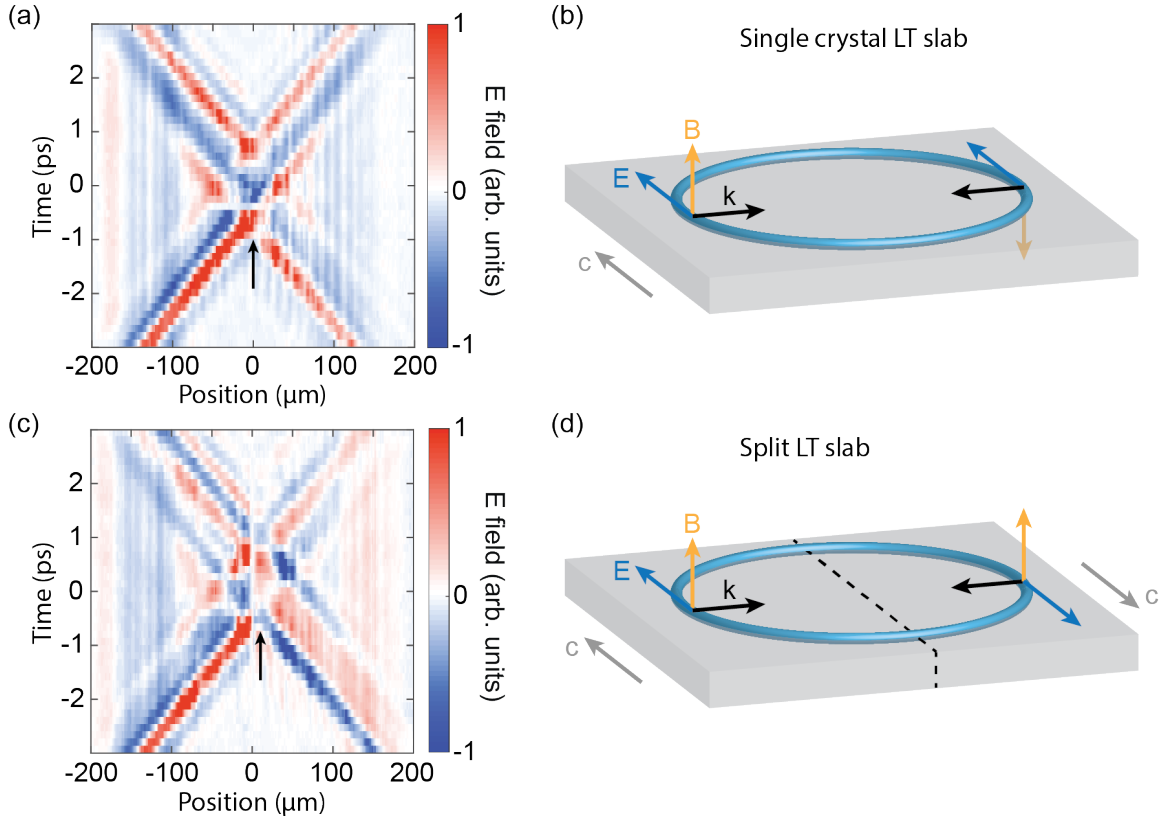
Figure 5-13: **Imaging the electric fields in a normal and "split" LT slab.** (a,c) Space-time plots of the THz electric field excited in the geometries shown in (b) and (d). The sign of the electric field shown in (c) is inverted on one side of the cut due to the reversed LT c-axis orientation. The position of the THz focus is marked by an arrow in both plots. (b,d) Schematic illustrations the electric and magnetic field polarizations of the excited THz fields in (b) a normal LT slab and (d) a modified LT slab where the c-axis is reversed on opposite sides of the THz focus. The dashed line in (d) indicates the cut in the "split" LT slab.

pump fluence. In practice, this means choosing the number of rings such that the pump fluence is just below the optical damage threshold.

5.7 Magnetic field behavior

Unlike most experimental geometries, the TREx scheme generates two counter-propagating focusing THz fields. This means that while the THz electric field components interfere constructively at the focus, the magnetic field components interfere destructively to reach nearly zero amplitude. Although the magnetic field cannot be

imaged directly in our experimental geometry, its behavior can be inferred by imaging the electric field in a "split" LT slab where the LT c-axis is reversed on one side of the THz focus. The "split" slab was constructed from a single LT slab. The slab was cut parallel to the c-axis using femtosecond laser machining [37] and one half was flipped over to reverse the c-axis orientation. The two pieces were then rotated 180 degrees so that their edges at the interface were pristine (i.e. not laser cut), brought as close together as possible on a flat surface, and then glued together at the corners using nail polish. In order to facilitate imaging of the THz field at the focus, the center of the pump rings was shifted slightly away from the cut so that the THz signal was not obscured. Fig. 5-13b,d show the electric and magnetic field polarizations in both a normal uncut LT slab and a "split" slab. By reversing the c-axis in half of the slab, the polarity of the electric (magnetic) fields is reversed, resulting in destructive (constructive) interference in the new slab.

Experimental space-time plots for both the normal and "split" slabs are shown in Fig. 5-13a,c respectively. The normal slab shows constructive interference of the electric fields at the focus. In contrast, the "split" slab shows destructive interference, reducing the THz field strength at the center of the focus by a factor of 6. By observing destructive interference in the electric field in the "split" slab, we deduce that the magnetic field destructively interferes in the normal slab. There are a few reasons that could explain why the destructive interference was not perfect in the experiment. Inhomogeneities in the intensity profile of the pump beam prevent the destructive interference from perfectly cancelling the electric fields in the "split" slab. In addition, the TREx focus was slightly offset from the cut, which leads to a small imbalance in the THz field strength generated on either side of the cut. The air gap in the cut was measured to be $<5\,\mu m$ wide, which is extremely small compared to the THz wavelength in air, so we expect negligible losses in THz field amplitude due to tunneling through the air gap. However, slight out-of-plane misalignment of the two slabs could diminish how efficiently the THz field tunnels through the gap. We note that constructive interference of the THz magnetic field could also be achieved in a single LT slab by including a temporal delay between the two sides

of the optical pump light, for example by inserting different thicknesses of glass in front of the left and right-hand sides of the circular echelon. A shift of one-half of the peak THz wavelength would optimize the magnetic field superposition. Although the superposition is not optimized for the entire THz bandwidth, this approach could permit switching between enhanced electric or magnetic field components at the focus.

Unlike in the experiments where we can only directly measure the THz electric fields, the magnetic fields could be directly observed in simulations. Fig. 5-14 shows the electric and magnetic field profiles in the normal and "split" slabs. In the normal slab, the electric (magnetic) field interferes constructively (destructively) at the focus as expected. In the "split" slab, the behavior is reversed and the electric (magnetic) field interferes destructively (constructively). Note that the focusing patterns of the magnetic field in the normal slab and the electric field in "split" slab are virtually identical. This confirms that imaging the electric field in the "split" slab gives qualitative insight into the magnetic field behavior in a normal slab. The peak magnetic field strength achieved in the "split" slab can be estimated from the corresponding peak electric field strength in the normal slab using

$$ B_{\mathrm{peak}} = \frac{1}{v_{\mathrm{ph}}} E_{\mathrm{peak}} \approx \left(\frac{1.92\,\mathrm{mT}}{1\,\mathrm{kV/cm}} \right) E_{\mathrm{peak}} \tag{5.21} $$

If a normal slab generates a peak electric field strength of $175\,\mathrm{kV/cm}$, then a "split" slab would generate a peak magnetic field strength of $337\,\mathrm{mT}$ under the same experimental conditions.

5.8   Summary and future directions

To conclude, we have demonstrated a novel compact scheme for generating large THz field strengths in thin LT waveguide slabs using a conical pulse front. The largest THz field strengths recorded using this technique without damage to the LT were $175\,\mathrm{kV/cm}$ at a $1\,\mathrm{kHz}$ laser repetition rate. Higher field strengths up to $300\,\mathrm{kV/cm}$ were observed at $10\,\mathrm{Hz}$ repetition rate. We expect that the peak THz field strength
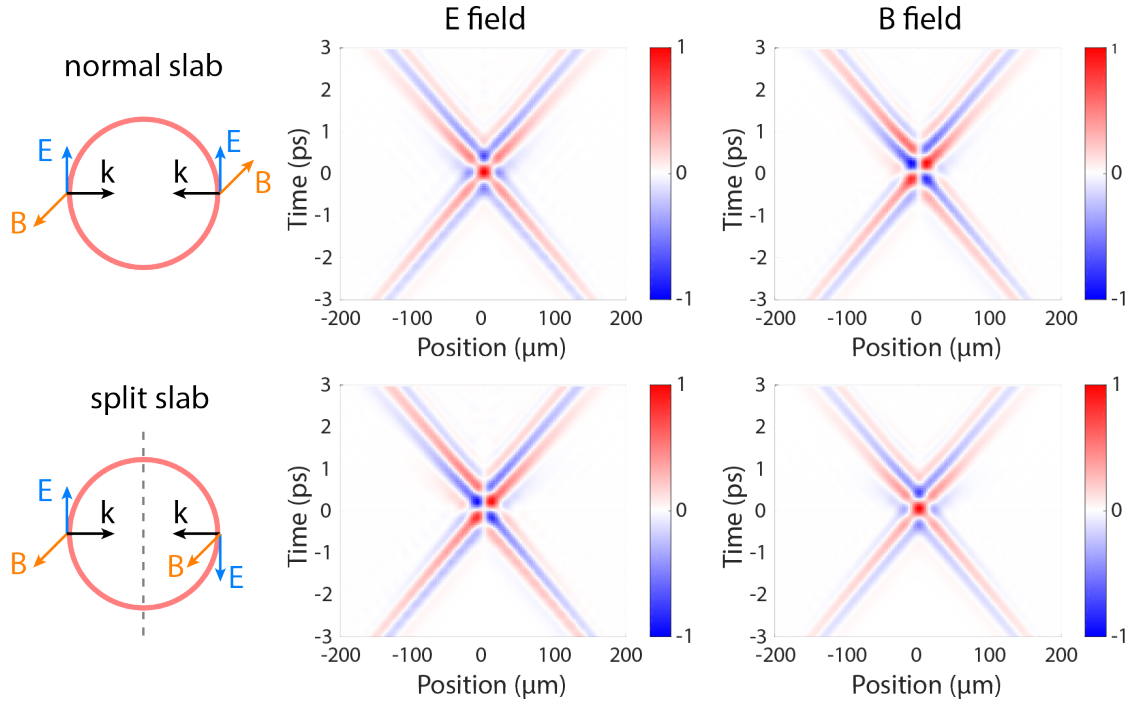
Figure 5-14: **Simulations of electric and magnetic field behavior.** Simulated electric and magnetic field profiles for a normal slab (top row) and "split" slab (bottom row).

could be further increased by pumping at a longer wavelength such as 1030 nm where THz generation is more efficient [123]. This method enables versatile waveguide-based THz spectroscopy and photonics by allowing strong THz fields to be delivered without any free-space THz generation or propagation to samples that could be on the LT surface or in a laser-machined hole at the focus and perhaps located inside a cryostat, cryomagnet, or XFEL chamber. Furthermore, we showed that the magnetic field component of the focusing THz field is significantly diminished at the focus ordinarily, and that measures can be taken to reverse the enhancement to generate a strong magnetic field and a diminished electric field. This method could be useful for studying materials that respond to both a THz electric and magnetic field, such as multiferroics, without using THz enhancement structures to selectively enhance one of the field components.

Chapter 6

THz spectroscopy using thin LN waveguides

The polaritonics platform has enabled many compact, detailed studies of integrated photonics structures, such as photonic crystals [43, 45, 133], cavities [47, 48, 134], and many more [54] during which the THz fields are directly monitored as they interact with the structures. However, the platform's utility as an integrated spectroscopy platform to probe light-matter interactions has remained largely unexplored. This is primarily because the large THz refractive index in LN results in a large LN fill fraction and, consequently, limited interaction between the THz fields and most samples deposited on the waveguide surface. In other words, only a very limited amount of the THz energy interacts with the deposited sample, resulting in small signals that can be hard to detect. Even in cases where the refractive index of the sample matches that of LN, these materials tend to be optically opaque which complicates imaging of the THz fields.

In this chapter, we describe two geometries aimed to expand the range of potential samples for compact, integrated THz spectroscopy using LN waveguides. The first geometry uses LN waveguides with a high-reflecting (HR) dielectric coating deposited on one face of the waveguide with the sample of interest deposited directly onto the HR coating. The waveguided THz fields penetrate through the HR coating and couple evanescently to the sample. The optical probe enters the LN and picks

up the THz signal, reflects off the the HR coating, and is subsequently imaged, all without entering the sample. This method is useful when the deposited material would strongly scatter or absorb the probe light, which severely hinders the usual polaritonics imaging techniques where the probe beam would need to pass through the sample layer. The second geometry uses a slot waveguide structure which consists of two thin strips of high-index material separated by a low-index slot [135, 136]. When the THz field enters the slot waveguide structure, the electric field is enhanced in the low-index region. This allows for efficient coupling to a low-index sample inserted into the slot.

6.1   THz imaging using HR-coated LN

In these experiments, we use an unpatterned 50 µm thick LN waveguide with a high-reflecting (HR) dielectric coating deposited on the backside designed to reflect the 532-nm probe wavelength. The thickness of the dielectric coating is much smaller than the THz wavelength, so the coating does not perturb the waveguide modes or THz propagation. Because the optical probe only picks up THz signal within the LN layer, the HR coating allows the THz fields to be imaged without the optical probe ever entering the sample layer. This enables experiments where the sample is strongly absorptive in the visible range as well as powdered samples which would scatter the probe beam.

THz imaging is performed using the polarization gating imaging method typically used for polaritonics experiments [104]. The pump beam is polarized parallel to the LN c-axis and focused to a line using a cylindrical lens, like usual. A collimated probe beam is polarized at a 45° angle relative to the LN c-axis and enters the LN slab from the uncoated side. Because the probe does not transmit through the LN slab, we cannot use the self-compensating geometry to eliminate the change in probe polarization due to the static birefringence in LN. Instead, we place a compensating crystal before the Wollaston prism. The probe passes through the 50 µm thick LN slab twice, so we use a 100 µm thick compensating crystal. Note that doing so does
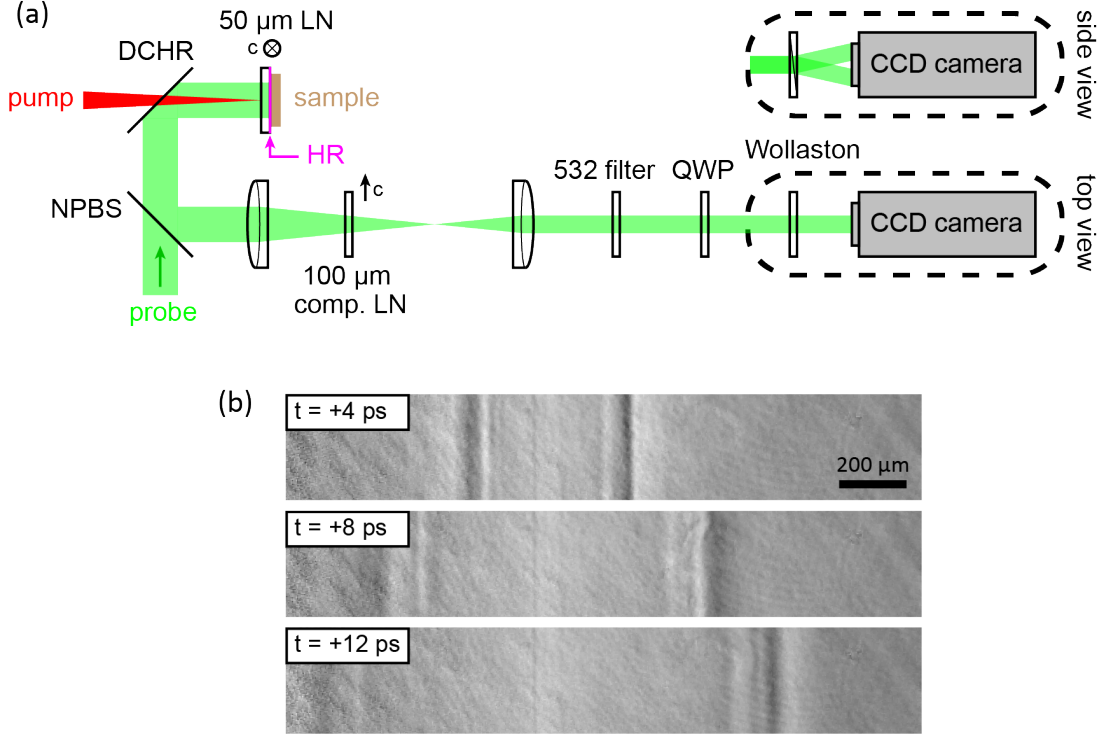
Figure 6-1: **Reflective imaging geometry.** (a) Schematic illustration of the reflective imaging geometry. The geometry is similar to the polarization gating imaging geometry shown in Fig. 3-8a. The LN waveguide has a 532-nm high-reflecting coating (HR) on the back side. The sample is adhered directly to the HR coating. Because the self-compensating imaging geometry cannot be used with the reflective LN waveguides, a 100-µm compensating crystal is used instead. (b) Representative images of the THz fields in a 50-µm LN slab obtained using the reflective geometry.

not compensate for local variations in the birefringence (e.g. due to stresses caused by laser machined structures) or thickness of the LN slab. The reflective imaging geometry is shown in Fig. 6-1a. Representative THz images obtained using this method in a LN slab without a deposited sample are shown in Fig. 6-1b.

6.1.1   Polariton imaging in a LN/EFO hybrid slab

In order to demonstrate the utility of the the reflective imaging geometry, we image the THz fields in a hybrid slab made of a HR-coated 50-µm LN slab and an 80-µm ErFeO$_3$ (EFO) slab, similar to what was studied previously [48]. Note that the THz refractive index of EFO is nearly the same as in LN ($n \approx 5$), so the hybrid waveguide is expected to behave like a single dielectric slab waveguide that is 130 µm thick. The
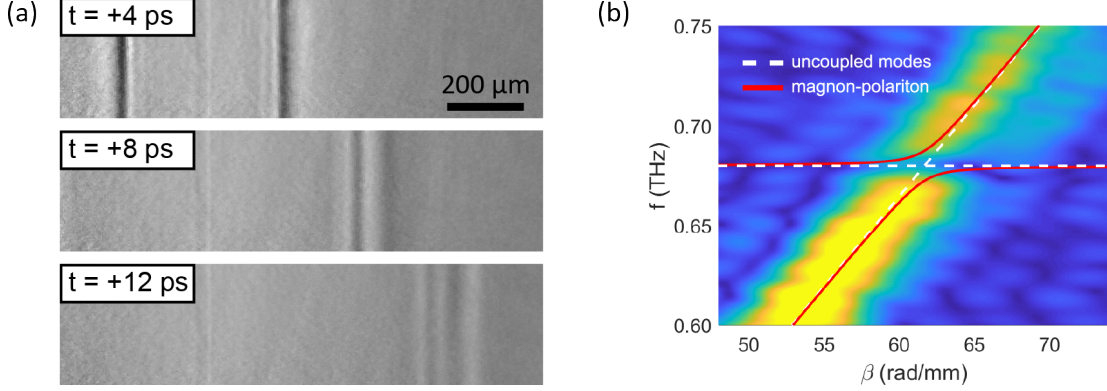
Figure 6-2: **Reflective polariton imaging in a LN/EFO hybrid waveguide slab.** (a) Images of the THz fields in the LN/EFO hybrid waveguide slab at various pump-probe delays. (b) Dispersion plot of the polaritons propagating in the LN/EFO hybrid waveguide slab obtained using the reflective polarization gating imaging technique. An avoided crossing is present at $0.67\,\mathrm{THz}$. The uncoupled TE_0 and bare magnon dispersion curves (white dashed lines) and the upper and lower magnon polariton dispersion curves (red solid lines) are also plotted.

HR coating was placed between the LN and EFO pieces. Due to the strong absorption of light with wavelength less than $1.2\,\mu\mathrm{m}$ in EFO [137], imaging the THz fields in a hybrid LN/EFO waveguide slab using the usual transmissive imaging technique with an optical probe suffers from very poor signal-to-noise. The advantage of the reflective geometry is that the probe never passes through the EFO layer, so the THz fields can be easily imaged despite the strong absorption at the probe wavelength.

The pump beam was focused to a line on the bare LN region and the fields were imaged as they propagate through the LN/EFO portion of the hybrid slab. The THz fields are very clearly visible in the images, as shown in Fig. 6-2a. The dispersion plot shown in Fig. 6-2b was calculated from images taken at many different pump-probe delays. The dispersion follows the expected TE_0 waveguide dispersion for a 130-µm thick slab waveguide with refractive index $n = 5$ and also shows an avoided crossing at $0.67\,\mathrm{THz}$, which indicates strong coupling between the phonon-polaritons in LN and the quasi-antiferromagnetic magnon modes in EFO. The extracted splitting frequency is $\Omega = 15\,\mathrm{GHz}$, which is similar to the previously measured value of $20\,\mathrm{GHz}$ [48]. This confirms that the dielectric coating is effectively invisible to the THz fields and does not affect coupling into the adjacent EFO slab.

6.1.2 Estimation of material parameters of lactose

Although the reflective imaging geometry is not ideal for compact THz spectroscopy due to the poor coupling between the waveguided THz fields and a sample (except in special cases like EFO where the THz refractive index is similar to that in LN), the technique could be used to get a rough measure of the material properties of a sample. As a test sample, we use powdered α-lactose monohydrate (Sigma-Aldrich, 99% purity, CAS 5989-81-1) which has a strong, sharp absorption peak centered at 0.53 THz which corresponds to a hindered rotation of the lactose molecules in the crystal [138, 139]. The powdered lactose was pressed into a 500 µm thick pellet and adhered to the HR-coated side of the thin LN to form an asymmetric waveguide slab. A small droplet of water was used to partially dissolve the pellet and recrystallize it on the LN surface to provide better adhesion.

Images of the THz fields were recorded in the LN slab using the reflective imaging geometry. The pump beam is line focused on a bare LN region (without lactose) and the THz field is propagated into the region covered in lactose. The imaging region, shown in Fig. 6-3a, includes both a region with lactose and a region without lactose so that the "signal" (with lactose) and "reference" (without lactose) measurements could be performed simultaneously. Space-time plots of the THz fields in the signal and reference regions are shown in Fig. 6-3b,c. Dispersion plots, shown in Fig. 6-3d,e, are calculated from the space-time plots via a 2D Fourier transform. The interactions between the THz field and the deposited sample are very weak, which results in space-time and dispersion plots that qualitatively appear very similar. There is a very small dip in the signal dispersion intensity at 0.53 THz, indicated by the arrow in Fig. 6-3e, which matches the center frequency of the absorption peak.

We can extract the complex dielectric function of lactose from the dispersion plots using perturbation theory. (See Section 2.4 for more details.) Here, we treat the change in cladding refractive index due to the deposited lactose as the perturbation. The symmetric LN waveguide (air cladding on both sides) is taken as the unperturbed structure. As observed in the LN/EFO hybrid slab, the HR coating does not interact
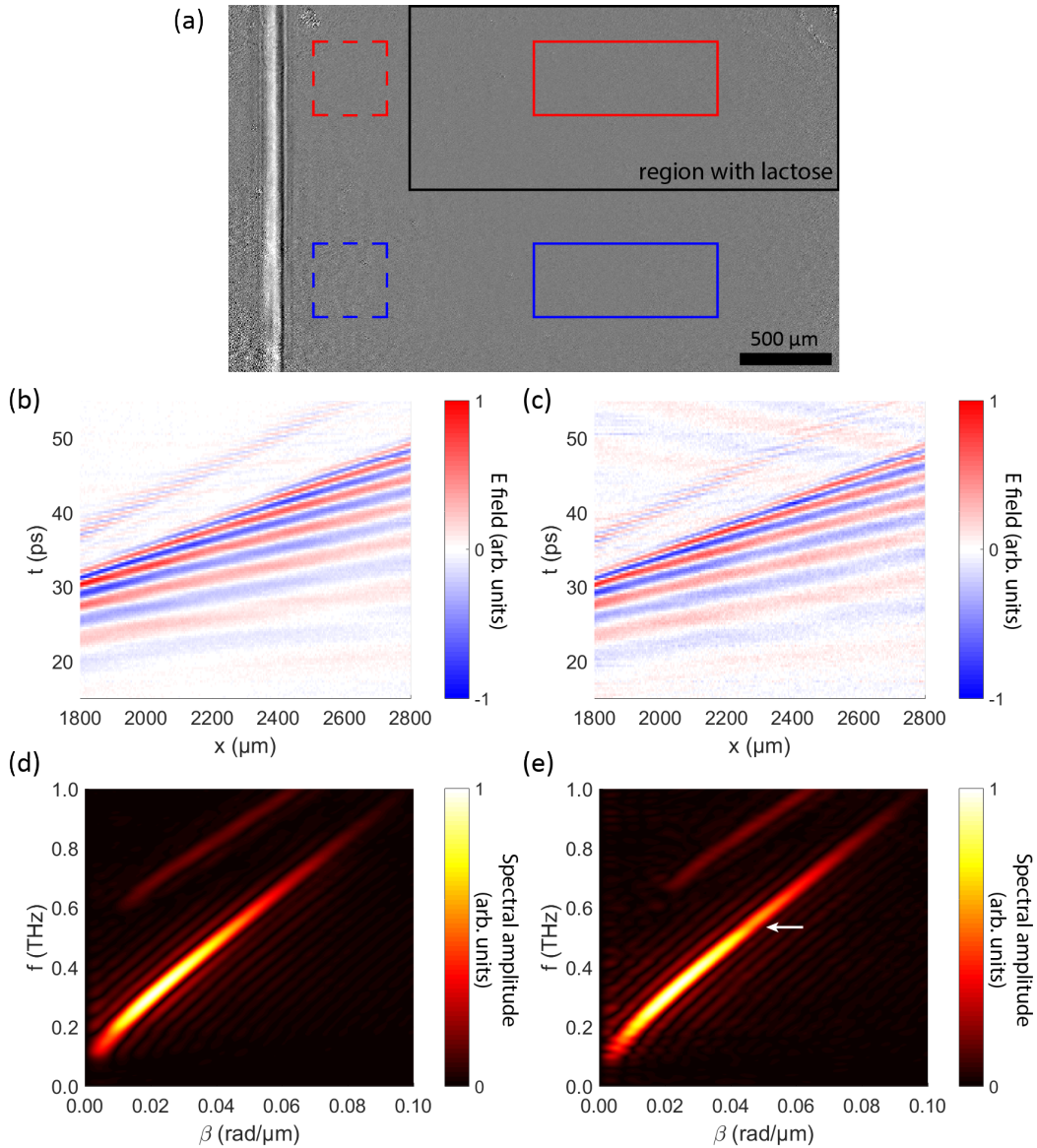
Figure 6-3: **Reflective polariton imaging in a LN slab with lactose deposited.**
(a) Experimental image of the THz fields in the LN slab. The black rectangle indicates
the approximate region where lactose was deposited on top of the waveguide. The
solid boxes indicate the region used the signal (red) and reference (blue) space-time
plots and dispersion. The dashed boxes indicate the regions used to normalized the
THz fields for quantitative comparison. (b,c) Representative space-time plots of the
THz fields in the reference region (b) and the region with lactose (c). The time-
dependent field profile is determined by vertically averaging the THz signal within
the corresponding region. x is the distance away from the line pump. (d,e) Dispersion
plots in the reference region (d) and the region with lactose (e). The dispersion plot
in (e) shows a very faint absorption feature at $0.53\,\mathrm{THz}$ (marked with a white arrow).

with the THz fields and can be ignored. To first order, the shift in propagation constant is proportional to the change in dielectric function in the waveguide cladding. Suppose that the unperturbed mode has propagation constant $\beta^{(0)} = \beta + i\gamma$ and that the perturbation introduces a first-order correction $\beta^{(1)} = \kappa + i\alpha$. Along the propagation direction (z), the waveguide has continuous translational symmetry and the electric field profile $E(x, z)$ can be described as a harmonic wave with propagation constant $\beta + \kappa$ subject to attenuation proportional to $\gamma + \alpha$.

$$E(x, z) = E_0 E_m(x) \exp\left[i(\beta + \kappa) z\right] \exp\left[-(\gamma + \alpha) z\right] \tag{6.1}$$

where $E_m(x)$ is the (normalized) TE mode profile for the unperturbed slab waveguide with confinement along the x-axis. Taking the modulus squared of the Fourier transform of $E(x, z)$ and integrating the THz field over the thickness of the waveguide gives the intensity spectrum

$$\left|\tilde{E}(k)\right|^2 = \frac{|E_0|^2}{[k - (\beta + \kappa)]^2 + (\gamma + \alpha)^2} \left|\int_0^d E_m(x) \ dx\right|^2 \tag{6.2}$$

which yields a Lorentzian function centered at $\beta + \kappa$ with a linewidth given by $\gamma + \alpha$. The real part of the dielectric function for the perturbation leads to a shift in the dispersion to higher wavevectors. We can extract the real part of the dielectric function by comparing the two experimentally measured dispersion plots. The wavevector shift obtained from the experimental dispersion plots is shown in Fig. 6-4a. The imaginary part of the dielectric function leads to an increase in the effective absorption coefficient, which leads to two changes in the dispersion. First, an increase in damping rate leads to a increase in the width of the Lorentzian function. Second, for the same initial THz field strength E_0, the increase in damping also results in a decrease in the spectral intensity. In principle, α could be extracted using either method. However, the linewidth is dominated by absorption in LN (which allows easy extraction of γ) and the experimental resolution is not good enough to reliably resolve α from the change in linewidth. Instead, we must rely on the change in peak intensity to deduce
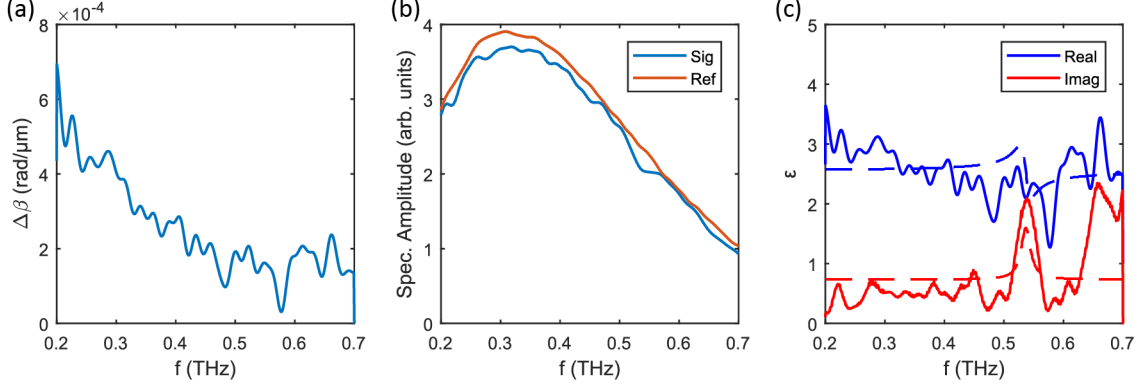
Figure 6-4: **Comparison of TE$_0$ dispersion with and without lactose.** (a) The shift in propagation constant $\Delta\beta$ calculated from the signal and reference dispersion plots. (b) TE$_0$ spectra in the signal and reference regions. There is a small dip in the signal spectrum at $0.53\,\text{THz}$, which corresponds to the well-known absorption feature in lactose. (c) Extracted values for the complex-valued ε. The Lorentzian fit is overlaid. The 6-µm air gap was not included when calculating these values.

α using

$$\frac{\left|\tilde{E}_{\text{sig}}\left(\beta+\kappa\right)\right|^2}{\left|\tilde{E}_{\text{ref}}\left(\beta\right)\right|^2} = \frac{\gamma^2}{\left(\gamma+\alpha\right)^2}\left|\frac{\int_0^d E_m^{\text{sig}}\left(x\right)\ dx}{\int_0^d E_m^{\text{ref}}\left(x\right)\ dx}\right|^2 \tag{6.3}$$

where $\tilde{E}_{\text{sig}}\left(\beta\right)$ and $\tilde{E}_{\text{ref}}\left(\beta+\kappa\right)$ are the peak spectral amplitudes in signal and reference dispersion, respectively. $E_m^{\text{sig}}\left(x\right)$ and $E_m^{\text{ref}}\left(x\right)$ are the TE mode profiles for the (asymmetric) LN waveguide with sample and the (symmetric) LN waveguide without sample, respectively. A brief discussion of the mode profiles and dispersion for an asymmetric slab waveguide is given in the appendix of this chapter. Because we are in the perturbative regime, the ratio of the integrals in Eq. 6.3 is nearly equal to 1 except at frequencies near the mode cutoff frequency. In this analysis, we assumed that the THz field excited by the line-focused pump is identical over the pump region. To correct for variations in the THz fields in the experiment (e.g. due to variations in the pump intensity profile), we normalize the signal and reference spectra using THz spectra taken in a small portion of the imaging region near the excitation region, shown in Fig. 6-3a. The corrected TE$_0$ spectra are shown in Fig. 6-4b.

After $\beta_m^{(1)}$ is determined, the sample permittivity $\varepsilon_{\text{samp}} = \varepsilon + \delta\varepsilon$ can be determined

using

$$\beta_m^{(1)} = \frac{\omega_m^{(0)}}{2v_{\mathrm{gr}}} \frac{\delta\varepsilon}{\varepsilon} f \tag{6.4}$$

where $\omega_m^{(0)}$ is the unperturbed angular frequency, v_{gr} is the group velocity, f is the fill fraction, ε is the unperturbed permittivity ($= 1$), and $\delta\varepsilon$ is the change in permittivity due to the perturbation. Both the real and imaginary parts of the extracted $\varepsilon_{\mathrm{samp}}$ are plotted in Fig. 6-4c. To determine the material parameters for lactose, we fit $\varepsilon_{\mathrm{samp}}$ to a Lorentzian oscillator model of the form

$$\varepsilon_{\mathrm{samp}} = \varepsilon_{\mathrm{r}} + i\varepsilon_{\mathrm{i}} = \varepsilon_\infty + \frac{\sigma\omega_0^2}{\omega_0^2 - \omega^2 + i\omega\Gamma} \tag{6.5}$$

The extracted values are shown in Table 6.1 and the fit is plotted on top of the data shown in Fig. 6-4c. Although the data are noisy, the fit does a good job extracting the center frequency for the lactose resonance. The other parameters are also decently extracted. Interestingly, looking at the the experimentally determined ε_{i} alone would suggest a much larger value for σ than what was extracted. However, ε_{r} does not show any correspondingly large variations near ω_0, so it acts as a penalizing term during the fitting procedure. Discrepancies in the values for ε_∞ and σ may be due to imperfect contact between the LN waveguide and the sample. Previous studies using LN/EFO hybrid slabs noted that there is a small air gap $<10\,\mu\mathrm{m}$ thick between the two slabs [48]. In that study, the gap was much smaller than the THz wavelength and both materials have similar THz refractive indices, so coupling between the THz phonon-polaritons in LN and the magnons in EFO was not significantly hindered. However, in this case coupling to the sample takes place through the evanescent field extending into the cladding. A 6-µm gap between the LN slab and the lactose pellet results in an effective 35% decrease in the fill fraction, which accounts for the discrepancies between the extracted material values and the literature values. The material parameters extracted after accounting for the 6-µm air gap are reported in Table 6.1.

We can also estimate ε_{r} directly from the cutoff frequencies in the experimental dispersion. From Fig. 6-3e, the TE_1 cutoff frequency for the asymmetric slab is

	Extracted values (no air gap)	Extracted values (6-µm air gap)	Literature values
ε_∞	2.5	3.3	3.35
σ	0.031	0.078	0.0524
$\omega_0/2\pi$ (THz)	0.54	0.54	0.5303
$\Gamma/2\pi$ (GHz)	19	37	25.8

Table 6.1: **Extracted material parameters for lactose using a 50 µm thick asymmetric LN waveguide.** Literature values taken from Ref. [140].

0.67 THz. Assuming that the original LN waveguides ($n \approx 5.1$) are 50 µm thick, using Eq. 6.20 we get an approximate refractive index $n \approx 1.6$ ($\varepsilon \approx 2.5$) for lactose which matches with the value determined using perturbation theory ignoring the air gap.

It should be noted that α-lactose monohydrate has a relatively strong THz absorption feature which facilitated extraction of material parameters. Most other samples would show much weaker signals, so this method may only be useful for obtaining a crude estimate of the material parameters, namely the low-frequency dielectric constant, or studies looking at shifts in a clear resonance feature. One way to improve the sensitivity of this method is to use a thinner LN slab, which would increase the sample fill fraction. Another possibility would be to use a photonic crystal structure with slow-light dispersion [141, 142]. Note that this would also increase the contribution to the effective absorption coefficient from LN, so one of the higher-frequency photonic bands (where the LN fill fraction is lower) would need to be used to have any benefit.

6.2   THz spectroscopy using a slot waveguide

In a typical polaritonics experiment, the optical pump beam is polarized along the LN c-axis which excites the TE modes of the waveguide. Although the THz fields can interact with the cladding material through the evanescent field, the coupling to the cladding is very weak because of the low cladding fill fraction. Alternatively, the optical pump could be polarized along the LN b-axis to excite the TM modes which have

a larger cladding fill fraction. However, the generation and detection efficiency for the TM modes is much weaker. This means that although a bare LN waveguide could theoretically be used to measure a sample placed in direct contact with the surface of the waveguide, the sensitivity would be very weak in either case and thus unappealing for most experiments (as shown in the previous section). Various strategies have been employed to try to improve the sensitivity of waveguide-based spectroscopy. In the infrared frequency range, long interaction lengths and group-velocity engineering have been used to increase the sensitivity [141–143]. However, these methods typically require processing areas with dimensions roughly $>100\times$ larger than the target wavelength which makes scaling these techniques to THz frequencies very difficult. An alternate strategy is to use plasmonic structures to localize an electromagnetic field in a small region where the sample is placed. Enhanced sensitivity has been demonstrated in the THz frequency range [42, 57, 144–146], but they relied on a somewhat narrow plasmonic resonance to target a specific frequency range around a known resonance in a sample. Using these techniques to investigate new materials with unknown absorption spectra would be cumbersome and time-consuming because only a small bandwidth could be interrogated at a time.

The slot waveguide is a structure used to localize the electric field in a low-index region over a relatively large bandwidth [135, 136]. The slot waveguide, shown in Fig. 6-5a, is composed to two parallel strips of high-index material with refractive index n_{core} surrounded by a low-index cladding with refractive index n_{clad}. There is a small sub-wavelength gap with width W_{slot} between the two high-index strips. Maxwell's equations require that the component of the electric displacement field $D = \varepsilon E$ that is polarized normal to a surface must be continuous when crossing a dielectric interface. Therefore, at the core/slot interface there is a discontinuity in E where the field strength jumps by a factor of $n_{\mathrm{core}}^2/n_{\mathrm{slot}}^2$, with the larger E field being within the slot. This results in an enhanced electric field in the low-index slot along with increased sensitivity to a sample placed within the slot.

The experimental geometry is shown in Fig. 6-5b. The slot waveguide structure was fabricated in a 50-µm LN slab waveguide (NanoLN) using chemically-assisted fem-
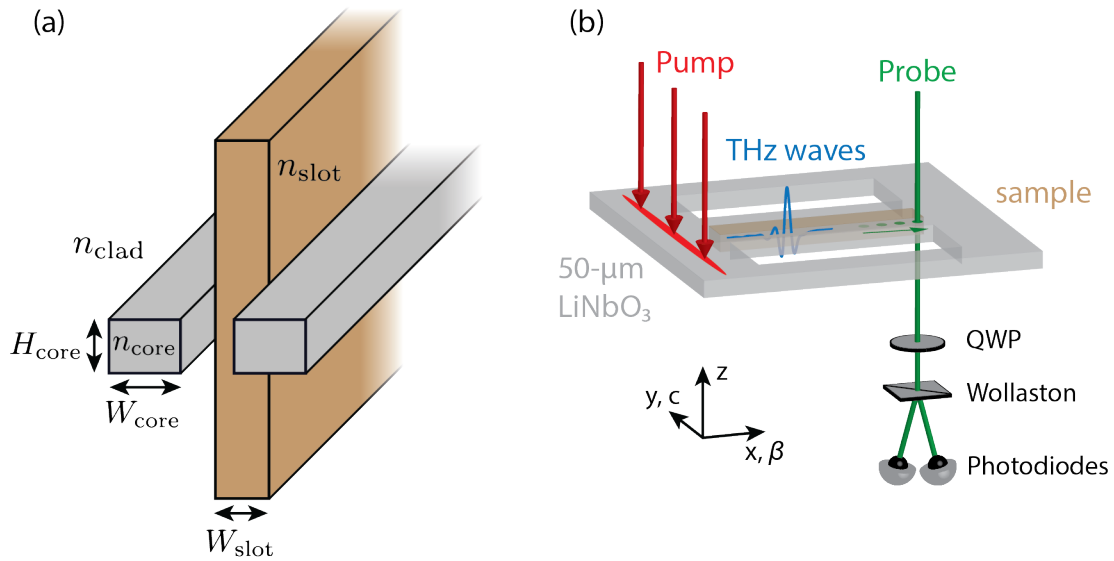
Figure 6-5: **Slot waveguide geometry.** (a) Schematic illustration of the slot waveguide structure. Two parallel strips of material with lateral dimensions W_{core} and H_{core} and refractive index n_{core} are separated by a distance W_{slot}. A slab of sample material with refractive index n_{slot} is inserted between the two strips. The sample slab extends outside of the slot. The entire assembly is surrounded by cladding with refractive index n_{clad}. (b) Schematic illustration of the experimental geometry. The slot waveguide structure is fabricated in a $50\,\mu\mathrm{m}$ thick LN slab waveguide ($H_{\mathrm{core}} = 50\,\mu\mathrm{m}$). A thin slab of sample is inserted into the slot. (The sample height along the z-axis is truncated for clarity.) The optical pump beam is polarized along the LN c-axis and is line-focused outside of the slot waveguide structure, and launches a THz wave that propagates along the x-axis. The optical probe beam passes through one of the LN strips, followed by a quarter-wave plate (QWP) and a Wollaston prism. The probe intensity is measured using balanced photodiodes. The parameters used for the slot waveguide are: $W_{\mathrm{core}} = 50\,\mu\mathrm{m}$, $W_{\mathrm{slot}} = 50\,\mu\mathrm{m}$.

tosecond laser machining [37]. The slot and LN strips were 50 µm wide (W_{slot} = 50 µm, W_{core} = 50 µm). The entire slot waveguide structure was 2.5 mm long. The experiments were performed using the output from a Ti:sapphire laser (center wavelength = 800 nm, pulse duration = 100 fs, repetition rate = 1 kHz). The output was split in a 95:5 ratio into the pump and probe beams. The pump pulses were attenuated to 200 µJ and focused onto the LN slab to a line 100 µm away from the edge of the slot waveguide structure using a 25-cm cylindrical lens. The pump was linearly polarized along the LN c-axis (y-axis in Fig. 6-5b). An optical chopper was used to chop the pump beam at 500 Hz. The THz fields were measured directly within the LN waveguide using methods described elsewhere [36]. The probe beam was frequency-doubled using a β-barium borate (BBO) crystal. The 400-nm output from the BBO was linearly polarized 45° relative to the LN optic axis and was focused into one of the LN strips in the slot waveguide using a 15-cm lens. The probe beam was then passed through a quarter-wave plate and Wollaston prism and the intensities of the two polarization components were measured using balanced photodiodes. A delay stage was used to control the pump-probe delay.

As a test sample, we used α-lactose monohydrate (Sigma-Aldrich, 99% purity, CAS 5989-81-1) due to its strong, sharp absorption peak centered at 0.53 THz which corresponds to a hindered rotation of the lactose molecules in the crystal [138, 139]. The lactose was dissolved in deionized water to make a saturated solution. The solution was then poured into a crystallizing dish and the solvent was allowed to evaporate under ambient conditions to form a ~500 µm thick layer of polycrystalline lactose. Femtosecond laser machining was used to cut a 40 µm by 1.5 mm slice of the lactose. The lactose slab was purposely cut to be slightly smaller than W_{slot} to facilitate inserting the slab into the slot. To load the sample into the slot, the thin lactose slab was placed on a stage with manual x, y, z control. The stage was aligned to the slot and the lactose slab was then gently pushed into the slot using a razor blade.

6.2.1 Experimental results

In order to measure THz absorption due to the inserted sample, the THz fields were measured along the LN strips with the lactose inserted ("signal" experiment) and in a reference experiment using an empty slot waveguide. The probe beam was stepped along the slot waveguide in 25-µm increments. For the reference experiments, the probe started $100\,\mu m$ away from the edge of the slot waveguide. For the experiments with lactose inserted, the probe started at the edge of the lactose slab and scanned over the extent of the filled region.

The reference space-time and dispersion plots are shown in Fig. 6-6a,b. The space-time plot shows a weak THz field with high group velocity and another stronger THz field with low group velocity. The dispersion plot shows features that agree with these observations. Below $0.6\,THz$, the THz fields have nearly linear dispersion that approaches the vacuum light line. In this regime, the THz wavelength ($\lambda \approx 100\,\mu m$ at $0.6\,THz$) is significantly larger than the LN strip dimensions, so the core fill fraction is relatively low and the effective refractive index for the mode is roughly 1. Above $0.6\,THz$, the dispersion plot becomes much more intense and deviates significantly from the vacuum light line. In this regime, the THz wavelength becomes smaller than the LN strip dimensions and the effective refractive index correspondingly increases.

The space-time and dispersion plots with the slot waveguide with the lactose sample inserted are shown in Fig. 6-6c,d. The space-time plot shows features similar to those of the reference space-time plot. In order to better visualize the effect of the lactose slab, a window function was used to isolate the weak, fast-moving THz feature in Fig. 6-6c when calculating the dispersion plot shown in Fig. 6-6d. A dip appears in the dispersion at around $0.53\,THz$, which matches the frequency of the well-known absorption peak in lactose. In addition, the dispersion below $0.6\,THz$ shifts to larger wavevectors corresponding to an increase in effective refractive index.

The absorption spectrum of lactose can be determined by observing how the THz spectrum evolves as it propagates through the slot waveguide. Fig. 6-7a shows the THz spectrum as a function of propagation distance obtained by applying an inverse
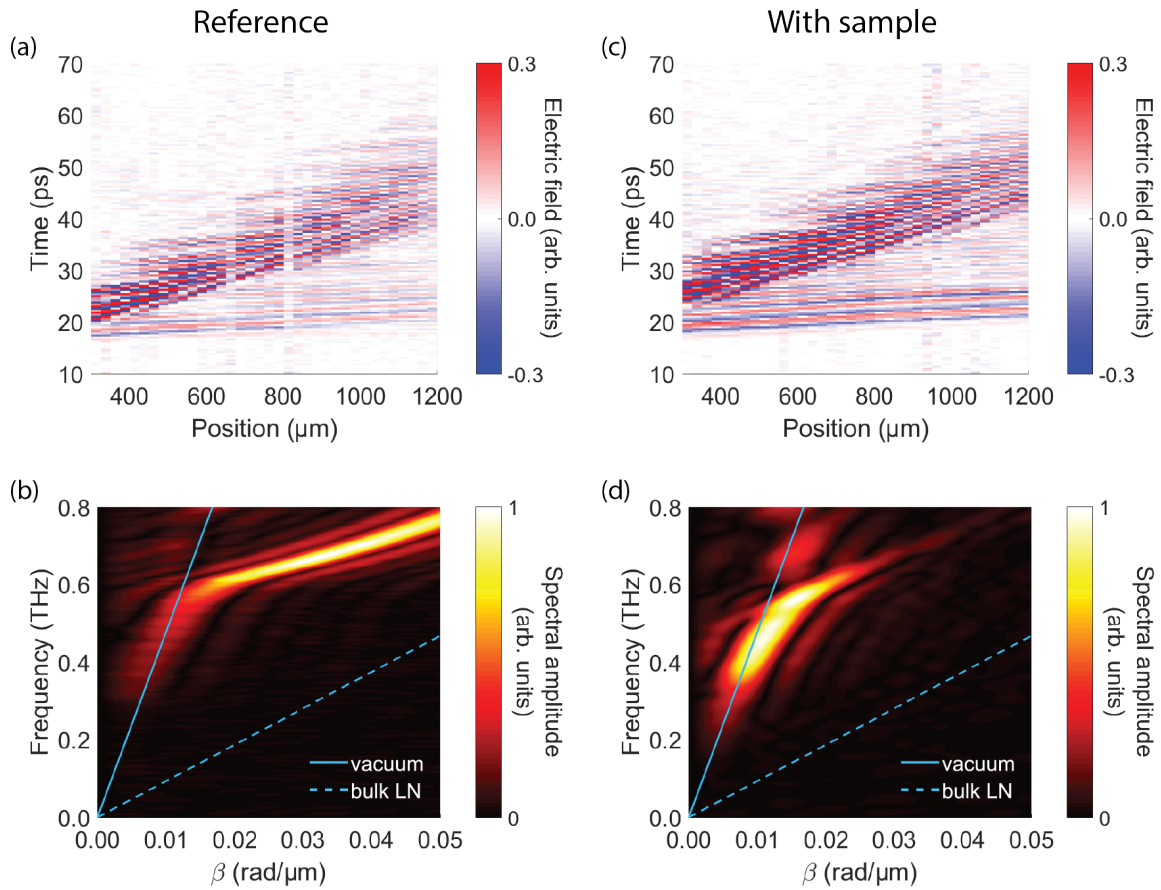
Figure 6-6: **THz field propagation through the slot waveguide.** Representative space-time (a,c) and dispersion (b,d) plots for the slot waveguide measurements. The reference measurements (a,b) were done with an empty slot waveguide. The "signal" measurements (c,d) were done with a lactose slab inserted into the slot.
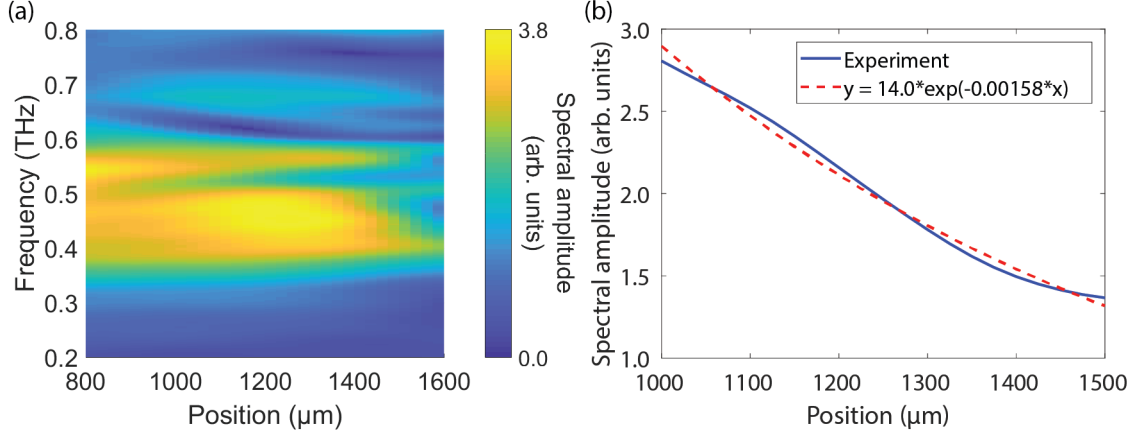
Figure 6-7: **Spectral evolution with lactose inserted into the slot waveguide.** (a) THz spectrum as a function of propagation distance. (b) A slice of the plot in (a) taken at 0.53 THz. The data are fit to an exponental decay, which is overlaid.

Fourier transform to the dispersion shown in Fig. 6-6d along the β-axis. A clear absorption feature appears in the spectrum starting from around 1 mm into the filled slot region and becomes stronger as the propagation distance is increased. Note that in order to facilitate inserting the lactose slab into the slot, the lactose was inserted at a small angle. This results in part of the lactose slab hanging out of the slot, which effectively makes the slot empty at probe positions less than 1 mm. Fig. 6-7b shows the spectral amplitude at 0.53 THz as a function of propagation distance within the filled slot region. There is a clear decrease in spectral amplitude that agrees well with an exponential fit. From the fit, the absorption coefficient α_{slot} was determined to be $30.8 \, \text{cm}^{-1}$.

6.2.2 Extraction of bulk material parameters

We can use perturbation theory to calculate the bulk absorption coefficient α_{bulk} from the experimental absorption coefficient α_{slot} for the sample inserted in the slot. Using a first-order calculation, the increase in absorption coefficient due to the sample is given by (see Section 2.4 for details)

$$\alpha_{\text{slot}} = \frac{\omega}{v_{\text{gr,slot}}} \frac{\varepsilon_{\text{i}}}{\varepsilon_{\text{r}}} f_{\text{slot}} \tag{6.6}$$

where ω is the THz angular frequency, $v_{\mathrm{gr,slot}}$ is the group velocity of the unperturbed slot waveguide, ε_{r} is the unperturbed permittivity in the slot, and f_{slot} is the slot fill fraction. Here, we treat absorption (i.e. $\mathrm{Im}\,(\varepsilon) \equiv \varepsilon_{\mathrm{i}}$) as the perturbation. Similarly, the bulk absorption coefficient is given by

$$\alpha_{\mathrm{bulk}} = \frac{\omega}{v_{\mathrm{ph,bulk}}} \frac{\varepsilon_{\mathrm{i}}}{\varepsilon_{\mathrm{r}}} \tag{6.7}$$

where $v_{\mathrm{ph,bulk}}$ is the bulk phase velocity, and ε_{r} and ε_{i} are the real and imaginary parts of the bulk permittivity, respectively. Using these two equations, we get the formula for calculating the bulk absorption coefficient from the experimental absorption coefficient

$$\frac{\alpha_{\mathrm{slot}}}{\alpha_{\mathrm{bulk}}} = \frac{v_{\mathrm{ph,bulk}}}{v_{\mathrm{gr,slot}}} f_{\mathrm{slot}} \tag{6.8}$$

The group velocity $v_{\mathrm{gr,slot}}$ can be determined from the slope of the experimental dispersion. Note that because we are only treating absorption as the perturbation, the group velocity should be taken for the slot waveguide structure with the sample inserted. From Fig. 6-6d, we get $v_{\mathrm{gr,slot}} = 150\,\mu\mathrm{m/ps}$. The refractive index of lactose is $n_{\mathrm{r}} = 1.86$ [140], so the bulk phase velocity $v_{\mathrm{ph,bulk}} = c/n_{\mathrm{r}} = 161\,\mu\mathrm{m/ps}$.

The fill fraction f is calculated using the definition

$$f_{\mathrm{slot}} = \frac{\langle \mathbf{E}_n^{(0)} | \varepsilon_{\mathrm{r}} | \mathbf{E}_n^{(0)} \rangle_{V_{\mathrm{slot}}}}{\langle \mathbf{E}_n^{(0)} | \varepsilon_{\mathrm{r}} | \mathbf{E}_n^{(0)} \rangle_V} \tag{6.9}$$

where $|\mathbf{E}_n^{(0)}\rangle$ is the electric field mode profile for the unperturbed structure and ε is the (unperturbed) permittivity map. The subscripts denote integration over all space (V) and over the slot region (V_{slot}). To determine $|\mathbf{E}_n^{(0)}\rangle$, we run EM simulations using the finite-different time-domain method using the open-source software MEEP [125]. We use a monochromatic THz source and propagate the simulation until the transient signals die out. The slot waveguide only supports one guided mode at low frequencies ($<0.8\,\mathrm{THz}$), so $|\mathbf{E}_n^{(0)}\rangle$ is taken simply as the electric field pattern at long times. Representative z-polarized THz electric field profiles are shown in Fig. 6-8a,b. Fig. 6-8a shows clear localization of the electric field within the slot. A slice of the

electric field profile through the middle of the structure ($y = 0$) is shown in Fig. 6-8b. Inside the high-index LN strips, the mode follows the typical sinusoidal spatial dependence and in the low-index regions, the electric field decays exponentially. Due to the electric displacement continuity condition, there is a discontinuous jump in the electric field strength at each interface which results in a relatively low electric field strength in the LN strips. This is consistent with the relatively weak THz fields observed in the experiment at lower frequencies. The calculated energy density of the slot waveguide mode is shown in Fig. 6-8c. Due to the large electric field strength in the slot, a significant portion of the energy density is localized within the slot, which results in efficient light-matter interactions. The calculated fill fractions in the slot and in the LN strips are shown in Fig. 6-8d. In the region between 0.35 THz and 0.50 THz, f_{slot} is approximately 50%, indicating efficient coupling to the sample placed in the slot in that frequency range. On the other hand, the LN fill fraction f_{LN} is quite low ($<10\%$). Above 0.50 THz, f_{slot} drops and f_{LN} increases rapidly. This behavior is consistent with the experimental dispersion where the effective refractive index is nearly unity at low frequencies and rapidly increases at frequencies above 0.6 THz.

In order to calculate the bulk absorption coefficient, we return to Eq. 6.8 and plug in the corresponding values ($v_{\text{ph,bulk}} = 161\,\mu\text{m/ps}$, $v_{\text{gr,slot}} = 150\,\mu\text{m/ps}$, $f_{\text{slot}} = 0.537 \times 0.8 = 0.427$). Note that the values for f_{slot} in Fig. 6-8d should be multiplied by 0.8 to account for the fact that the slot is $50\,\mu\text{m}$ wide while the inserted lactose slab is only $40\,\mu\text{m}$ wide. This gives a peak bulk absorption coefficient $\alpha_{\text{bulk}} = 65.1\,\text{cm}^{-1}$, which agrees very well with the literature value $\alpha = 66.84\,\text{cm}^{-1}$ [140].

Fig. 6-9a shows the calculated values for α_{bulk} for a range of frequencies around 0.53 THz. α_{bulk} can be converted to an imaginary refractive index n_{i} using the relationship

$$\alpha_{\text{bulk}} = \frac{4\pi n_{\text{i}}}{\lambda_0} \tag{6.10}$$

where λ_0 is the vacuum wavelength. The calculated values for n_{i} are shown in Fig.
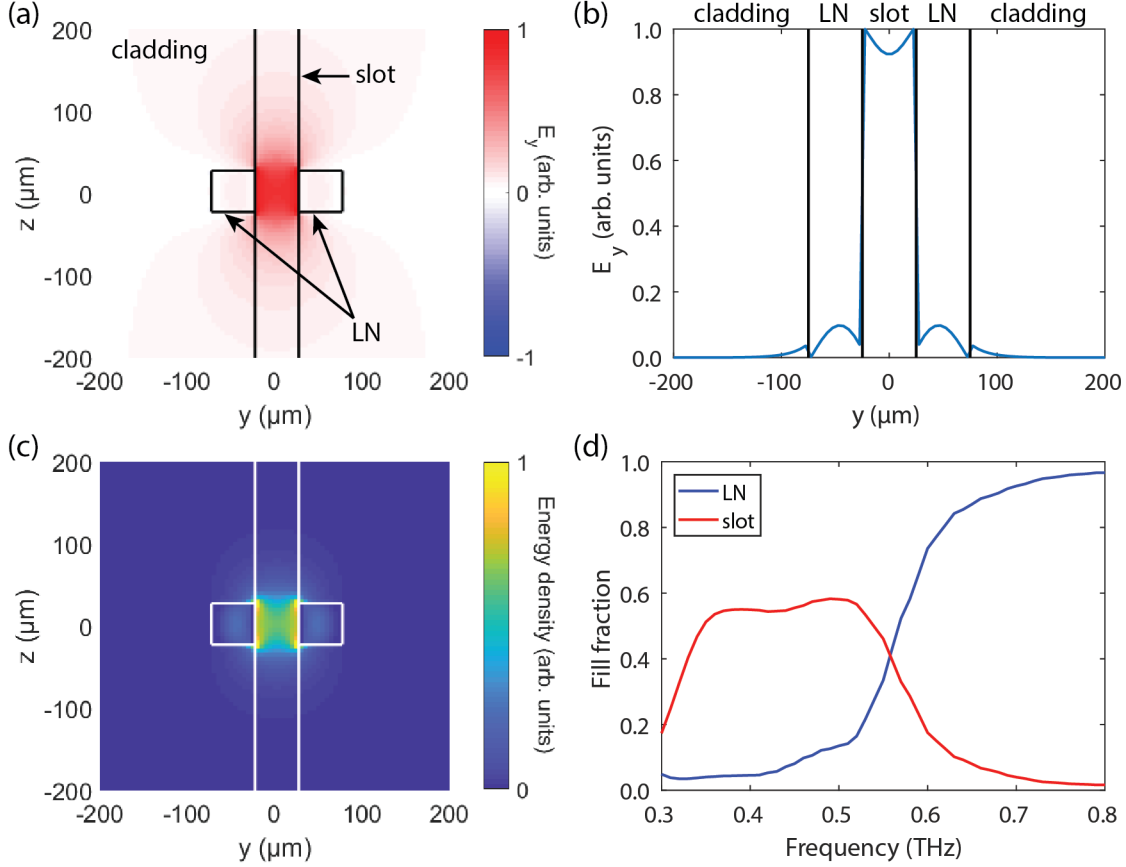
Figure 6-8: **Fill fraction calculation.** (a) Simulated E_y field profile at $0.53\,\text{THz}$. The black lines indicate the dielectric interfaces of the slot waveguide cross-section. The refractive index of the slot region was $n_{\text{slot}} = 1.86$. Because the sample used in our experiments was semi-infinitely long along the z-axis, the slot region extended infinitely along the z-axis as opposed to only containing the region between the two LN strips. (b) THz field profile along a horizontal slice through the center of the structure ($z = 0$) extracted from (a). The vertical black lines indicate the slot/LN and LN/cladding interfaces. (c) Calculated energy density profile for the EM mode shown in (a). The white lines indicate the dielectric interfaces of the slot waveguide cross-section. All field components were included when calculating the energy distribution. (d) Calculated fill fractions in LN (blue) and in the slot (red).

6-9b. We can fit n_{i} to the Lorentzian oscillator model using the equation

$$\varepsilon\left(\omega\right) = \left[n_{\text{r}}\left(\omega\right) + in_{\text{i}}\left(\omega\right)\right]^2 = \varepsilon_\infty + \frac{\sigma\omega_0^2}{\omega_0^2 - \omega^2 + i\omega\Gamma} \tag{6.11}$$

where ε_∞ is the high-frequency permittivity, ω_0 is the resonance frequency of the oscillator, Γ is the damping rate, and σ is the oscillator strength. The extracted
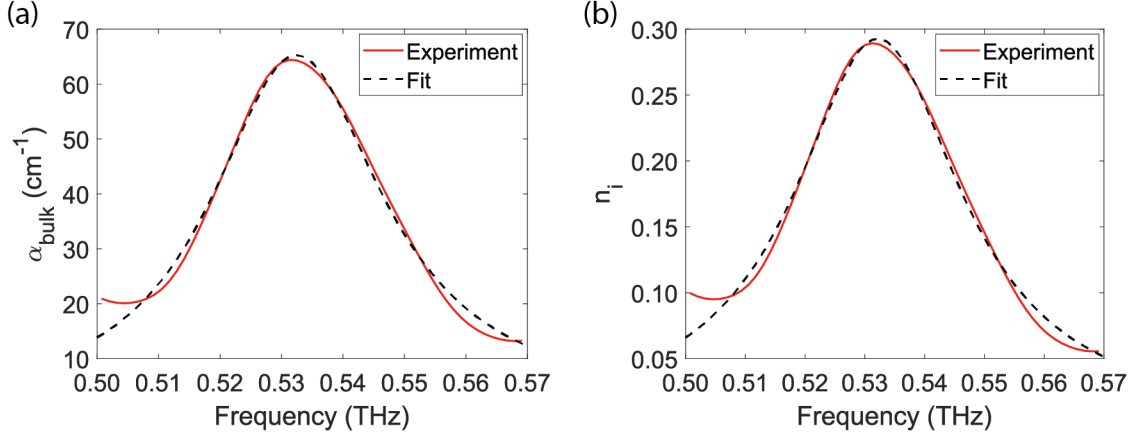
Figure 6-9: **Extracting parameters for bulk lactose.** (a) Values for α_{bulk} calculated using Eq. 6.8. (b) Values for imaginary refractive index n_i calculated using Eq. 6.10. The Lorentzian fit (dashed line) using the parameters output by the iterative procedure is also plotted in (a) and (b).

values are given in Table 6.2. Literature values are also tabulated for comparison. The fit recovers values that agree quite well with literature values.

It should be noted that lactose is a well-studied material in the THz frequency range, so the material parameters (notably the high-frequency permittivity ε_∞) are readily available and could be used for the calculation. For an novel material, ε_∞ is not necessarily known beforehand so there would be no value for $v_{\text{ph,bulk}}$ to use in Eq. 6.8 to calculate α_{bulk} from α_{slot}. To extract ε_∞ without prior knowledge, we use the following iterative process.

1. Choose an initial guess $\varepsilon_\infty^{(1)} > 1$.

2. Calculate α_{bulk} using $v_{\text{ph,bulk}} = \dfrac{c}{\sqrt{\varepsilon_\infty}}$.

3. Calculate n_i from α_{bulk} using Eq. 6.8 and fit to Eq. 6.11.

4. Calculate the refined value $\varepsilon_\infty^{(n+1)}$ as the average value between $\varepsilon_\infty^{(n)}$ and the value for ε_∞ output by the fit.

5. Repeat steps 2–4 until $\varepsilon_\infty^{(n)}$ converges with the output from the fit.

Starting with an initial guess $\varepsilon_\infty^{(1)} = 2.0$ ($n_r = 1.4$, $v_{\text{ph,bulk}} = 210\,\mu\text{m/ps}$), this procedure converges after 5 iterations to $\varepsilon_\infty = 3.3$, which agrees well with the literature

144

	Extracted values (using literature ε_∞)	Extracted values (using iterative procedure)	Literature values
ε_∞	3.35*	3.3	3.35
σ	0.054	0.055	0.0524
$\omega_0/2\pi$ (THz)	0.53	0.53	0.5303
$\Gamma/2\pi$ (GHz)	34	34	25.8

Table 6.2: **Extracted material parameters for lactose using a LN slot waveguide.** Literature values taken from Ref. [140]. * indicates that the parameter was fixed to this value during fitting.

value. The material parameters output by the iterative procedure are given in Table 6.2.

6.3 Summary and future directions

In this chapter, we discussed two techniques that improve the capabilities of the polaritonics platform for compact THz spectroscopy.

The first method uses an HR-coated LN slab to facilitate imaging the THz fields as they interact with a sample that is incompatible with the usual polarization gating imaging geometry. The technique was used to image magnon-polaritons in a hybrid LN/EFO hybrid slab. The measured dispersion showed an avoided crossing indicative of strong coupling between the THz-frequency phonon-polaritons in LN and the quasi-antiferromagnetic magnon mode in EFO, as reported before. The technique was also used to measure the dielectric function of α-lactose monohydrate. Perturbation theory was used to extract the complex dielectric function of lactose. Although the sensitivity is poor, the technique could be used to extract the center frequency of a material resonance and also provide a rough estimate for the refractive index. In general, this technique could be leveraged to observe the THz fields in a hybrid waveguide as they interact with a strcture, e.g. observing magnon-polaritons that are confined within a cavity or are scattered off of a structure.

The second method uses a slot waveguide to localize the THz electric field inside a low-index region for improved coupling to a sample. A thin slab of α-lactose monohydrate was inserted into the slot and the absorption spectrum was measured over

a relatively large bandwidth with good sensitivity. The bulk absorption spectrum was calculated using perturbation theory and fit to a Lorentzian oscillator model to yield material parameters that agree very well with literature. The fitting procedure does not depend on any prior knowledge about the sample, so it could be used to characterize novel materials. These results open up a lot of potential for compact THz spectroscopy, especially in cases where specialized sample environments make it difficult to use a traditional THz-TDS setup, e.g. samples located inside the bore of a cryomagnet.

Lastly, the slot waveguide structure is particularly compatible with the TREx method described in Chapter 5 and has the potential to enable compact nonlinear THz experiments. Although the TREx method can generate THz electric field strengths up to $175 \, \text{kV/cm}$ at the TREx focus, the field strength rapidly diminishes as the fields diverge which limits the interaction length between the THz fields and a potential sample. Furthermore, $175 \, \text{kV/cm}$ is the average field strength measured in the LT slab. The field strength at the LT/air interface for the TE_0 mode at $0.7 \, \text{THz}$ is about half of the maximum value. This means that a sample placed at the surface of the LT slab would experience around $85 \, \text{kV/cm}$ which generally is too low to efficiently drive nonlinear behavior in many materials of interest. The slot waveguide address both of these problems. Fig. 6-10a shows one possible configuration for a compact nonlinear THz experiment using TREx excitation together with a slot waveguide. The TREx method is used with only half of the echelon mirror illuminated so that the pump beam is shaped into a series of half-rings that excite a converging THz field in a thin LT crystal. The pump half-rings are positioned so that the THz fields focus into the slot waveguide. A nonlinear crystal is inserted into the slot and an optical probe beam is used to read out the nonlinear response of the sample. In order to estimate the THz electric field strengths in the slot, an FDTD simulation of the proposed geometry was performed and the peak electric field strength was recorded along the center of the slot waveguide. Fig. 6-10b shows the extracted field strengths. The peak field strength is approximately $100 \, \text{kV/cm}$ right at the entrance of the slot waveguide and it diminishes to about $60 \, \text{kV/cm}$ over $200 \, \mu\text{m}$ of propagation. Potential samples that
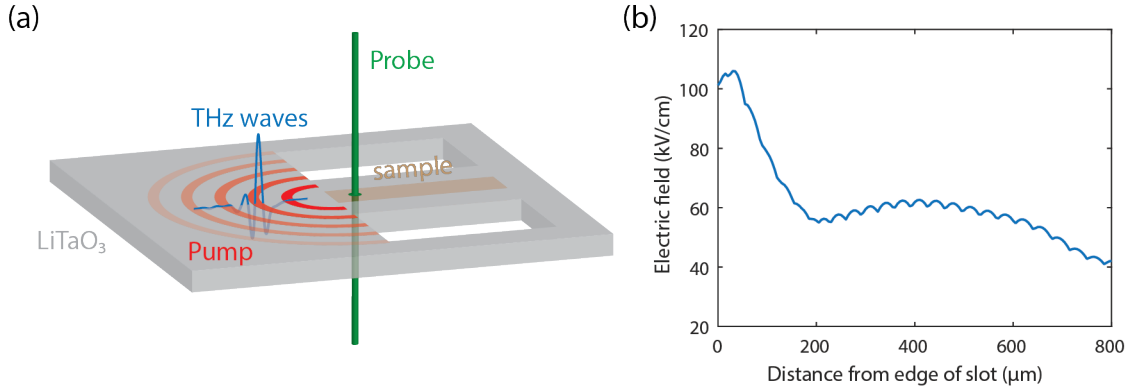
Figure 6-10: **Integrated nonlinear THz spectroscopy using the polaritonics platform.** (a) Schematic illustration of a potential nonlinear THz experimental geometry. The TREx pump half-rings are used to excite a converging THz field that focuses into the slot waveguide that is laser machined in a thin LT slab. A sample (e.g. nonlinear crystal) is inserted into the slot. An optical probe is used to read out the nonlinear response of the sample. (b) Plot of the maximum THz electric field strength within the slot.

should show a nonlinear response at these field strengths include nonlinear crystals such as ZnTe [147] and β-barium borate [148] and also monolayer transition metal dichalcogenides [149]. The decrease in peak field strength is due to strong dispersion of the slot waveguide. This suggests that using the TREx method with a narrowband pumping scheme, such as chirp-and-delay [35], would maintain a high field level for a longer propagation distance. Note that the nonlinear THz-induced sample response may be measured optically, as shown in Fig. 6-10a, or by measurement of a coherent THz signal emitted in a direction out of the waveguide plane. In these cases the path length in the sample may be unimportant, and it could be possible to irradiate the sample with THz fields excited via two sets of TREx pump half-rings that focus from both sides. This would increase the field strength and also allow for the selection of an optimized THz electric or magnetic field component as described earlier.

6.4 Appendix: TE modes of an asymmetric dielectric waveguide

In the reflective imaging geometry, the cladding on one side of the waveguide is replaced with the sample. In some cases (e.g. EFO), both the LN and sample slabs have similar refractive indices, so the hybrid slab should be treated as a single waveguide with increased thickness. However, in most cases the sample has a much lower refractive index than the LN slab, so we treat the structure as an asymmetric slab waveguide. Here, we will assume that the high-index core with refractive index n_{core} is surrounded by an air cladding (refractive index $n_{\text{air}} = 1$) on one side and some homogeneous sample (refractive index n_{samp}) on the other side. The refractive index profile, shown in Fig. 6-11a, is given by

$$n\left(x\right) = \begin{cases} n_{\text{core}} & 0 \leq x \leq d \\ n_{\text{air}} & x < 0 \\ n_{\text{samp}} & x > d \end{cases} \tag{6.12}$$

where $n_{\text{core}} > n_{\text{samp}} > n_{\text{air}}$.

To solve for the TE mode profiles and mode dispersion, we follow a procedure similar to that described in Section 3.2.1 for a symmetric waveguide. We start by writing the general form of the $E_y\left(x\right)$ given by Maxwell's equations. For guided modes, the electric field profile is sinusoidal within the high-index core and decays exponentially in the low-index cladding.

$$E_y\left(x\right) = \begin{cases} A\cos\left(hx\right) + B\sin\left(hx\right) & 0 \leq x \leq d \\ C\exp\left(q_{\text{air}}x\right) & x < 0 \\ D\exp\left(-q_{\text{samp}}x\right) & x > d \end{cases} \tag{6.13}$$
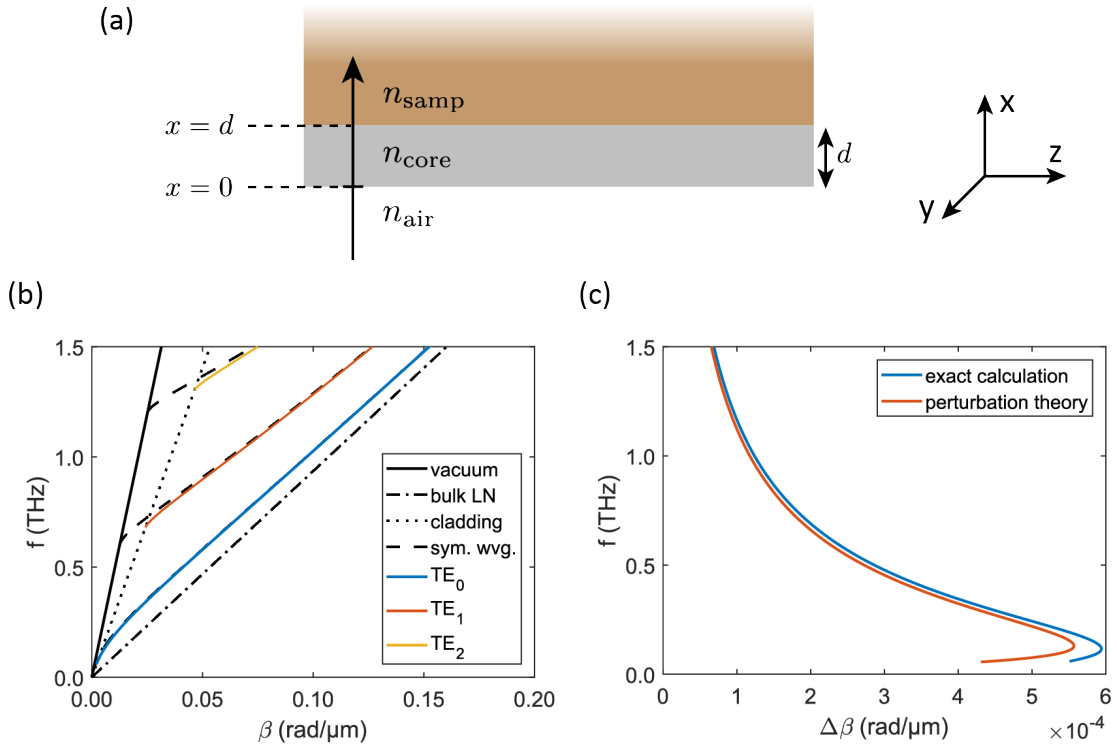
Figure 6-11: **The asymmetric dielectric slab waveguide.** (a) Refractive index profile for the asymmetric waveguide. (b) Calculated TE dispersion curves for an asymmetric 50-µm LN slab waveguide where $n_{samp} = 1.7$. The dispersion for a symmetric 50-µm LN slab waveguide (with air cladding on both sides) is also plotted (black dashed lines) for reference. (c) Calculated wavevector shift (blue line) for the TE_0 mode in (b) for an asymmetric slab waveguide relative to a symmetric waveguide. The values calculated from first-order perturbation theory (orange line) are also plotted for comparison.

where h, q_{air}, and q_{samp} are related to the propagation constant β by

$$\beta^2 = n_{core}^2 k_0^2 - h^2 = n_{air}^2 k_0^2 + q_{air}^2 = n_{samp}^2 k_0^2 + q_{samp}^2 \qquad (6.14)$$

This puts constraints on the possible values of β for the guided modes.

$$n_{samp}^2 k_0^2 < \beta < n_{core}^2 k_0^2 \qquad (6.15)$$

By invoking the field continuity conditions at each dielectric interface, we get the following functions for $E_y(x)$, $H_x(x)$, and $H_z(x)$.

$$E_y(x) = C \begin{cases} \cos(hx) + \dfrac{q_{air}}{h} \sin(hx) & 0 < x < d \\ \exp(q_{air}x) & x < 0 \\ \left[\cos(hd) + \dfrac{q_{air}}{h} \sin(hd)\right] \exp\left[-q_{samp}(x-d)\right] & x > d \end{cases} \qquad (6.16)$$

$$H_x(x) = \dfrac{\beta C}{\omega \mu_0} \begin{cases} \cos(hx) + \dfrac{q_{air}}{h} \sin(hx) & 0 < x < d \\ \exp(q_{air}x) & x < 0 \\ \left[\cos(hd) + \dfrac{q_{air}}{h} \sin(hd)\right] \exp\left[-q_{samp}(x-d)\right] & x > d \end{cases} \qquad (6.17)$$

$$H_z(x) = -\dfrac{iC}{\omega \mu_0} \begin{cases} -h \sin(hx) + q_{air} \cos(hx) & 0 < x < d \\ q_{air} \exp(q_{air}x) & x < 0 \\ -q_{samp} \left[\cos(hd) + \dfrac{q_{air}}{h} \sin(hd)\right] \exp\left[-q_{samp}(x-d)\right] & x > d \end{cases}$$
$$\qquad (6.18)$$

Using these equations, we get the characteristic equation

$$\tan(hd) = \frac{h(q_{air} + q_{samp})}{h^2 - q_{air}q_{samp}} \qquad (6.19)$$

Note that setting $q_{air} = q_{samp}$ recovers the characteristic equation (Eq. 3.22) for the symmetric waveguide. Using this equation, we can numerically solve for the dispersion $\beta(\omega)$. A representative dispersion plot for an asymmetric waveguide is shown in

Fig. 6-11b. Compared to the dispersion for a symmetric waveguide, the asymmetric waveguide dispersion is very similar. In general, there is a slight increase in the propagation constant β due to the increase in cladding refractive index. The cutoff frequencies for the TE modes are also increased. The difference in TE_0 propagation constant $\Delta\beta$ between the symmetric and asymmetric waveguides is plotted in Fig. 6-11c.

The cutoff frequencies for the modes can be found by setting β to its minimum value ($\beta = n_{\mathrm{samp}}\omega/c$) and plugging into Eq. 6.19. This gives the equation

$$f_{\mathrm{cutoff},m} = \frac{c}{2\pi d\sqrt{n_{\mathrm{core}}^2 - n_{\mathrm{samp}}^2}} \left[m\pi + \arctan\left(\sqrt{\frac{n_{\mathrm{samp}}^2 - n_{\mathrm{air}}^2}{n_{\mathrm{core}}^2 - n_{\mathrm{samp}}^2}} \right) \right] \qquad (6.20)$$

where m is an integer denoting the TE_m waveguide modes. Note that compared to Eq. 3.23 for a symmetric waveguide, there is an additional $\arctan(\cdot)$ term that contributes a small increase to the cutoff frequencies. This causes the TE_0 mode to have a nonzero cutoff frequency, unlike for a symmetric waveguide where the TE_0 cutoff frequency is always 0.

The asymmetric waveguide dispersion can also be estimated from perturbation theory. (See Section 2.4 for details.) The first-order shift in wavevector $\beta_m^{(1)}$ is given by

$$\beta_m^{(1)} = \frac{\omega_m}{2v_{\mathrm{gr}}} \frac{\delta\varepsilon}{\varepsilon} f_{\mathrm{clad}} \qquad (6.21)$$

where ω is the angular frequency, v_{gr} is the group velocity of the unperturbed mode at ω_m, $\delta\varepsilon$ is the change in cladding permittivity, ε is the unperturbed cladding permittivity, and f_{clad} is the cladding fill fraction. The calculated $\beta_m^{(1)}$ is compared against the values from an exact calculation in Fig. 6-11c. There is excellent agreement between the two plots. At low frequencies, there is moderate disagreement between the calculated values. This is because f_{clad} rapidly increases near the cutoff frequency, so the perturbation theory calculation should be carried out to higher orders for the calculation to converge. At higher frequencies f_{clad} is quite small, so first-order perturbation theory is sufficient.

Bibliography

[1] J. B. Baxter and G. W. Guglietta, "Terahertz Spectroscopy," *Analytical Chemistry*, vol. 83, no. 12, pp. 4342–4368, 2011.

[2] A. I. McIntosh, B. Yang, S. M. Goldup, M. Watkinson, and R. S. Donnan, "Terahertz spectroscopy: A powerful new tool for the chemical sciences?" *Chemical Society Reviews*, vol. 41, no. 6, pp. 2072–2082, 2012.

[3] T. Kampfrath, K. Tanaka, and K. A. Nelson, "Resonant and nonresonant control over matter and light by intense terahertz transients," *Nature Photonics*, vol. 7, no. 9, pp. 680–690, 2013.

[4] J. El Haddad, B. Bousquet, L. Canioni, and P. Mounaix, "Review in terahertz spectral analysis," *TrAC Trends in Analytical Chemistry*, vol. 44, pp. 98–105, 2013.

[5] P. Salén *et al.*, "Matter manipulation with extreme terahertz light: Progress in the enabling THz technology," *Physics Reports*, vol. 836, pp. 1–74, 2019.

[6] E Pickwell and V. Wallace, "Biomedical applications of terahertz technology," *Journal of Physics D: Applied Physics*, vol. 39, no. 17, R301, 2006.

[7] K. Fukunaga and M. Picollo, "Terahertz spectroscopy applied to the analysis of artists' materials," *Applied Physics A*, vol. 100, pp. 591–597, 2010.

[8] P. U. Jepsen, D. G. Cooke, and M. Koch, "Terahertz spectroscopy and imaging–Modern techniques and applications," *Laser & Photonics Reviews*, vol. 5, no. 1, pp. 124–166, 2011.

[9] L. Afsah-Hejri, P. Hajeb, P. Ara, and R. J. Ehsani, "A Comprehensive Review on Food Applications of Terahertz Spectroscopy and Imaging," *Comprehensive Reviews in Food Science and Food Safety*, vol. 18, no. 5, pp. 1563–1621, 2019.

[10] A. Mitsuishi, "Progress in far-infrared spectroscopy: Approximately 1890 to 1970," *Journal of Infrared, Millimeter, and Terahertz Waves*, vol. 35, pp. 243–281, 2014.

[11] P. R. Smith, D. H. Auston, and M. C. Nuss, "Subpicosecond photoconducting dipole antennas," *IEEE Journal of Quantum Electronics*, vol. 24, no. 2, pp. 255–260, 1988.

[12] D. H. Auston and K. Cheung, "Coherent time-domain far-infrared spectroscopy," *JOSA B*, vol. 2, no. 4, pp. 606–612, 1985.

[13] D. Auston and A. Glass, "Optical generation of intense picosecond electrical pulses," *Applied Physics Letters*, vol. 20, no. 10, pp. 398–399, 1972.

[14] L Xu, X.-C. Zhang, and D. Auston, "Terahertz beam generation by femtosecond optical pulses in electro-optic materials," *Applied Physics Letters*, vol. 61, no. 15, pp. 1784–1786, 1992.

[15] J. Hebling, G. Almasi, I. Z. Kozma, and J. Kuhl, "Velocity matching by pulse front tilting for large-area THz-pulse generation," *Optics Express*, vol. 10, no. 21, pp. 1161–1166, 2002.

[16] K.-L. Yeh, M. C. Hoffmann, J Hebling, and K. A. Nelson, "Generation of 10 μJ ultrashort terahertz pulses by optical rectification," *Applied Physics Letters*, vol. 90, no. 17, p. 171 121, 2007.

[17] H Hirori, A Doi, F Blanchard, and K Tanaka, "Single-cycle terahertz pulses with amplitudes exceeding 1 MV/cm generated by optical rectification in $LiNbO_3$," *Applied Physics Letters*, vol. 98, no. 9, p. 091 106, 2011.

[18] S. Fleischer, Y. Zhou, R. W. Field, and K. A. Nelson, "Molecular orientation and alignment by intense single-cycle THz pulses," *Physical Review Letters*, vol. 107, no. 16, p. 163 603, 2011.

[19] S. Fleischer, R. W. Field, and K. A. Nelson, "Commensurate two-quantum coherences induced by time-delayed THz fields," *Physical Review Letters*, vol. 109, no. 12, p. 123 603, 2012.

[20] J. Lu, Y. Zhang, H. Y. Hwang, B. K. Ofori-Okai, S. Fleischer, and K. A. Nelson, "Nonlinear two-dimensional terahertz photon echo and rotational spectroscopy in the gas phase," *Proceedings of the National Academy of Sciences*, vol. 113, no. 42, pp. 11 800–11 805, 2016.

[21] P. Zalden *et al.*, "Molecular polarizability anisotropy of liquid water revealed by terahertz-induced transient orientation," *Nature Communications*, vol. 9, no. 1, pp. 1–7, 2018.

[22] M. Sajadi, M. Wolf, and T. Kampfrath, "Transient birefringence of liquids induced by terahertz electric-field torque on permanent molecular dipoles," *Nature Communications*, vol. 8, no. 1, pp. 1–9, 2017.

[23] P. Gaal, K. Reimann, M. Woerner, T. Elsaesser, R. Hey, and K. H. Ploog, "Nonlinear terahertz response of n-type GaAs," *Physical Review Letters*, vol. 96, no. 18, p. 187 402, 2006.

[24] G Sharma *et al.*, "Time-resolved terahertz spectroscopy of free carrier nonlinear dynamics in semiconductors," *IEEE Photonics Journal*, vol. 2, no. 4, pp. 578–592, 2010.

[25] H Wen, M Wiczer, and A. Lindenberg, "Ultrafast electron cascades in semiconductors driven by intense femtosecond terahertz pulses," *Physical Review B*, vol. 78, no. 12, p. 125 203, 2008.

[26] X. Li *et al.*, "Terahertz field–induced ferroelectricity in quantum paraelectric $SrTiO_3$," *Science*, vol. 364, no. 6445, pp. 1079–1082, 2019.

[27] H Yamakawa *et al.*, "Terahertz-field-induced polar charge order in electronic-type dielectrics," *Nature Communications*, vol. 12, no. 1, p. 953, 2021.

[28] S. Baierl *et al.*, "Nonlinear spin control by terahertz-driven anisotropy fields," *Nature Photonics*, vol. 10, no. 11, pp. 715–718, 2016.

[29] S. Schlauderer *et al.*, "Temporal and spectral fingerprints of ultrafast all-coherent spin switching," *Nature*, vol. 569, no. 7756, pp. 383–387, 2019.

[30] J. Shi *et al.*, "Intrinsic 1T' phase induced in atomically thin 2H-MoTe$_2$ by a single terahertz pulse," *Nature Communications*, vol. 14, no. 1, p. 5905, 2023.

[31] T. Feurer, N. S. Stoyanov, D. W. Ward, J. C. Vaughan, E. R. Statz, and K. A. Nelson, "Terahertz Polaritonics," *Annual Review of Materials Research*, vol. 37, no. 1, pp. 317–350, 2007.

[32] R. M. Koehl and K. A. Nelson, "Coherent optical control over collective vibrations traveling at lightlike speeds," *The Journal of Chemical Physics*, vol. 114, no. 4, pp. 1443–1446, 2001.

[33] T Feurer, J. C. Vaughan, and K. A. Nelson, "Spatiotemporal coherent control of lattice vibrational waves," *Science*, vol. 299, no. 5605, pp. 374–377, 2003.

[34] T Feurer, J. C. Vaughan, T Hornung, and K. A. Nelson, "Typesetting of terahertz waveforms," *Optics Letters*, vol. 29, no. 15, pp. 1802–1804, 2004.

[35] Z. Chen, X. Zhou, C. A. Werley, and K. A. Nelson, "Generation of high power tunable multicycle teraherz pulses," *Applied Physics Letters*, vol. 99, no. 7, p. 071 102, 2011.

[36] Q. Wu, C. A. Werley, K.-H. Lin, A. Dorn, M. G. Bawendi, and K. A. Nelson, "Quantitative phase contrast imaging of THz electric fields in a dielectric waveguide," *Optics Express*, vol. 17, no. 11, pp. 9219–9225, 2009.

[37] P. Sivarajah, C. A. Werley, B. K. Ofori-Okai, and K. A. Nelson, "Chemically assisted femtosecond laser machining for applications in LiNbO$_3$ and LiTaO$_3$," *Applied Physics A*, vol. 112, no. 3, pp. 615–622, 2013.

[38] X. Zhou *et al.*, "One-step precise machining of terahertz microstructures on chip-scale lithium niobate via laser dispersion engineering," *Materials Today Physics*, vol. 35, p. 101 102, 2023.

[39] C. A. Werley *et al.*, "Time-resolved imaging of near-fields in THz antennas and direct quantitative measurement of field enhancements," *Optics Express*, vol. 20, no. 8, pp. 8551–8567, 2012.

[40] S. M. Teo *et al.*, "Visualization of guided and leaky wave behaviors in an indium tin oxide metallic slab waveguide," *Optics Express*, vol. 23, no. 11, pp. 14 876–14 896, 2015.

[41] Q. Zhang *et al.*, "Surface enhancement of THz wave by coupling a subwavelength LiNbO$_3$ slab waveguide with a composite antenna structure," *Scientific Reports*, vol. 7, no. 1, p. 17 602, 2017.

[42] R. Wang *et al.*, "Conversion from terahertz-guided waves to surface waves with metasurface," *Optics Express*, vol. 26, no. 24, pp. 31 233–31 243, 2018.

[43] B. K. Ofori-Okai, P. Sivarajah, C. A. Werley, S. M. Teo, and K. A. Nelson, "Direct experimental visualization of waves and band structure in 2D photonic crystal slabs," *New Journal of Physics*, vol. 16, no. 5, p. 053 003, 2014.

[44] P. Sivarajah, B. K. Ofori-Okai, S. M. Teo, C. A. Werley, and K. A. Nelson, "The homogenization limit and waveguide gradient index devices demonstrated through direct visualization of thz fields," *New Journal of Physics*, vol. 17, no. 1, p. 013 013, 2015.

[45] P. Sivarajah, A. A. Maznev, B. K. Ofori-Okai, and K. A. Nelson, "What is the Brillouin zone of an anisotropic photonic crystal?" *Physical Review B*, vol. 93, no. 5, p. 054 204, 2016.

[46] H. Xiong *et al.*, "Topological valley transport of terahertz phonon–polaritons in a $LiNbO_3$ chip," *ACS Photonics*, vol. 8, no. 9, pp. 2737–2745, 2021.

[47] C. Pan *et al.*, "Direct visualization of light confinement and standing wave in THz Fabry-Perot resonator with Bragg mirrors," *Optics Express*, vol. 25, no. 9, pp. 9768–9777, 2017.

[48] P. Sivarajah *et al.*, "THz-frequency magnon-phonon-polaritons in the collective strong-coupling regime," *Journal of Applied Physics*, vol. 125, no. 21, p. 213 103, 2019.

[49] Q. Zhang *et al.*, "Cavity-cavity coupling based on a terahertz rectangular sub-wavelength waveguide," *Journal of Applied Physics*, vol. 126, no. 6, 2019.

[50] J. Wang *et al.*, "Topologically tuned terahertz confinement in a nonlinear photonic chip," *Light: Science & Applications*, vol. 11, no. 1, p. 152, 2022.

[51] B. Zhang *et al.*, "THz band-stop filter using metamaterials surfaced on $LiNbO_3$ sub-wavelength slab waveguide," *Optics Express*, vol. 23, no. 12, pp. 16 042–16 051, 2015.

[52] W. Zhao *et al.*, "On-chip plasmon-induced transparency in THz metamaterial on a $LiNbO_3$ subwavelength planar waveguide," *Optics express*, vol. 27, no. 5, pp. 7373–7383, 2019.

[53] R. Wang *et al.*, "Broadband on-chip terahertz asymmetric waveguiding via phase-gradient metasurface," *ACS Photonics*, vol. 6, no. 7, pp. 1774–1779, 2019.

[54] C. A. Werley, K. A. Nelson, and C. R. Tait, "Direct visualization of terahertz electromagnetic waves in classic experimental geometries," *American Journal of Physics*, vol. 80, no. 1, pp. 72–81, 2012.

[55] Y. Lu *et al.*, "Propagation of THz pulses in rectangular subwavelength dielectric waveguides," *Journal of Applied Physics*, vol. 123, no. 22, 2018.

[56] Y. Lu *et al.*, "Time-resolved imaging of mode-conversion process of terahertz transients in subwavelength waveguides," *Frontiers of Physics*, vol. 14, pp. 1–5, 2019.

[57] R. Wang *et al.*, "Enhanced on-chip terahertz sensing with hybrid metasurface/lithium niobate structures," *Applied Physics Letters*, vol. 114, no. 12, p. 121 102, 2019.

[58] N. S. Stoyanov, D. W. Ward, T. Feurer, and K. A. Nelson, "Direct visualization of phonon-polariton focusing and amplitude enhancement," *The Journal of Chemical Physics*, vol. 117, no. 6, pp. 2897–2901, 2002.

[59] K.-H. Lin, C. A. Werley, and K. A. Nelson, "Generation of multicycle terahertz phonon-polariton waves in a planar waveguide by tilted optical pulse fronts," *Applied Physics Letters*, vol. 95, no. 10, p. 232, 2009.

[60] J. C. Maxwell, "III. On Physical Lines of Force," *Philosophical Magazine*, vol. 23, no. 151, pp. 12–24, 1861.

[61] O. C. Rømer, "Démonstration touchant le mouvement de la lumière," *Journal des Sçavans*, vol. 20, pp. 233–236, 1676.

[62] H. Fizeau, "Sur une expérience relative à la vitesse de propagation de la lumière," *Comptes rendus de l'Académie des Sciences*, vol. 29, 1849.

[63] O. Heaviside, *Electromagnetic Theory*. London, UK: The Electrician, 1912.

[64] J. D. Joannopoulos, S. G. Johnson, J. N. Winn, and R. D. Meade, *Molding the flow of light*. Princeton, NJ: Princeton University Press, 2008.

[65] S. Mukamel, *Principles of Nonlinear Optics and Spectroscopy*. New York, NY: Oxford University Press, 1995.

[66] L. D. Landau and E. M. Lifshitz, "Theory of the dispersion of magnetic permeability in ferromagnetic bodies," *Physikalische Zeitschrift der Sowjetunion*, vol. 8, p. 153, 1935.

[67] T. Gilbert and J. Kelly, "Anomalous rotational damping in ferromagnetic sheets," *Conference on Magnetism and Magnetic Materials*, p. 253, 1955.

[68] T. L. Gilbert, "A phenomenological theory of damping in ferromagnetic materials," *IEEE transactions on magnetics*, vol. 40, no. 6, pp. 3443–3449, 2004.

[69] M. C. Gutzwiller, "Moon-Earth-Sun: The oldest three-body problem," *Reviews of Modern Physics*, vol. 70, no. 2, p. 589, 1998.

[70] C. Cohen-Tannoudji, B. Diu, and F. Laloe, *Quantum Mechanics*. Weinheim, Germany: Wiley-VCH, 1986, vol. 2.

[71] G. Gaeta, *Perturbation Theory: Mathematics, Methods and Applications*. New York, NY: Springer Nature, 2022.

[72] J. S. Townsend, *A Modern Approach to Quantum Mechanics*. Melville, NY: University Science Books, 2012.

[73] K. Yee, "Numerical solution of initial boundary value problems involving Maxwell's equations in isotropic media," *IEEE Transactions on antennas and propagation*, vol. 14, no. 3, pp. 302–307, 1966.

[74] R. Courant, K. Friedrichs, and H. Lewy, "Über die partiellen Differenzengleichungen der mathematischen Physik," *Mathematische annalen*, vol. 100, no. 1, pp. 32–74, 1928.

[75] R. R. Bate, D. D. Mueller, and J. E. White, *Fundamentals of Astrodynamics.* New York, NY: Dover Publications, 1971.

[76] F. R. Moulton, *An introduction to celestial mechanics.* Chelmsford, MA: Courier Corporation, 1970.

[77] J.-P. Berenger, "A perfectly matched layer for the absorption of electromagnetic waves," *Journal of computational physics*, vol. 114, no. 2, pp. 185–200, 1994.

[78] S. G. Johnson, "Notes on perfectly matched layers (PMLs)," *arXiv preprint arXiv:2108.05348*, 2021.

[79] K. Huang, "Lattice vibrations and optical waves in ionic crystals," *Nature*, vol. 167, no. 4254, pp. 779–780, 1951.

[80] A. S. Barker and R Loudon, "Response functions in the theory of raman scattering by vibrational and polariton modes in dielectric crystals," *Reviews of Modern Physics*, vol. 44, no. 1, p. 18, 1972.

[81] D. L. Mills and E Burstein, "Polaritons: The electromagnetic modes of media," *Reports on Progress in Physics*, vol. 37, no. 7, p. 817, 1974.

[82] T. P. Dougherty, G. P. Wiederrecht, and K. A. Nelson, "Impulsive stimulated Raman scattering experiments in the polariton regime," *JOSA B*, vol. 9, no. 12, pp. 2179–2189, 1992.

[83] A. Barker Jr and R Loudon, "Dielectric properties and optical phonons in $LiNbO_3$," *Physical Review*, vol. 158, no. 2, p. 433, 1967.

[84] A. Barker Jr, A. Ballman, and J. Ditzenberger, "Infrared study of the lattice vibrations in $LiTaO_3$," *Physical Review B*, vol. 2, no. 10, p. 4233, 1970.

[85] R. H. Lyddane, R. Sachs, and E Teller, "On the polar vibrations of alkali halides," *Physical Review*, vol. 59, no. 8, p. 673, 1941.

[86] E. H. Korte and A. Röseler, "Infrared reststrahlen revisited: Commonly disregarded optical details related to n<1," *Analytical and Bioanalytical Chemistry*, vol. 382, no. 8, pp. 1987–1992, 2005.

[87] R. W. Boyd, *Nonlinear Optics.* Cambridge, MA: Academic Press, 2008.

[88] R. W. Boyd, "Order-of-magnitude estimates of the nonlinear optical susceptibility," *Journal of Modern Optics*, vol. 46, no. 3, pp. 367–378, 1999.

[89] K. Reimann, "Table-top sources of ultrashort THz pulses," *Reports on Progress in Physics*, vol. 70, no. 10, p. 1597, 2007.

[90] H. Hafez *et al.*, "Intense terahertz radiation and their applications," *Journal of Optics*, vol. 18, no. 9, p. 093 004, 2016.

[91] D. A. Kleinman, "Theory of second harmonic generation of light," *Physical Review*, vol. 128, no. 4, p. 1761, 1962.

[92] R. C. Miller and A Savage, "Temperature dependence of the optical properties of ferroelectric $LiNbO_3$ and $LiTaO_3$," *Applied Physics Letters*, vol. 9, no. 4, pp. 169–171, 1966.

[93] G. Francois, "cw measurement of the optical nonlinearity of ammonium dihydrogen phosphate," *Physical Review*, vol. 143, no. 2, p. 597, 1966.

[94] D. H. Auston, K. Cheung, J. Valdmanis, and D. Kleinman, "Cherenkov radiation from femtosecond optical pulses in electro-optic media," *Physical Review Letters*, vol. 53, no. 16, p. 1555, 1984.

[95] I. Tamm and I. Frank, "Coherent radiation of fast electrons in a medium," *Doklady Akademii Nauk SSSR*, vol. 14, no. 3, pp. 107–112, 1937.

[96] I. Frank and I. Tamm, "Coherent visible radiation of fast electrons passing through matter," in *Selected Papers*, Springer, 1991, pp. 29–35.

[97] B. K. Ofori-Okai, P. Sivarajah, W. R. Huang, and K. A. Nelson, "THz generation using a reflective stair-step echelon," *Optics Express*, vol. 24, no. 5, pp. 5057–5068, 2016.

[98] S. Kurtz and F. Robinson, "A physical model of the electro-optic effect," *Applied Physics Letters*, vol. 10, no. 2, pp. 62–65, 1967.

[99] M. Veithen, X. Gonze, and P. Ghosez, "First-principles study of the electro-optic effect in ferroelectric oxides," *Physical review letters*, vol. 93, no. 18, p. 187 401, 2004.

[100] I. Kaminow and E. Turner, "Electrooptic light modulators," *Applied optics*, vol. 5, no. 10, pp. 1612–1628, 1966.

[101] I. Kaminow and W. Johnston Jr, "Quantitative determination of sources of the electro-optic effect in $LiNbO_3$ and $LiTaO_3$," *Physical Review*, vol. 160, no. 3, p. 519, 1967.

[102] R. C. Jones, "A New Calculus for the Treatment of Optical Systems I. Description and Discussion of the Calculus," *Journal of the Optical Society of America*, vol. 31, no. 7, pp. 488–493, 1941.

[103] C. A. Werley, Q. Wu, K.-H. Lin, C. R. Tait, A. Dorn, and K. A. Nelson, "Comparison of phase-sensitive imaging techniques for studying terahertz waves in structured $LiNbO_3$," *Journal of the Optical Society of America B*, vol. 27, no. 11, pp. 2350–2359, 2010.

[104] C. A. Werley, S. M. Teo, B. K. Ofori-Okai, P. Sivarajah, and K. A. Nelson, "High-resolution, low-noise imaging in THz polaritonics," *IEEE Transactions on Terahertz Science and Technology*, vol. 3, no. 3, pp. 239–247, 2013.

[105] B. S. Dastrup, E. R. Sung, F. Wulf, C. Saraceno, and K. A. Nelson, "Enhancement of THz generation in $LiNbO_3$ waveguides via multi-bounce velocity matching," *Light: Science & Applications*, vol. 11, no. 1, pp. 1–8, 2022.

[106] J. Hebling, K.-L. Yeh, M. C. Hoffmann, and K. A. Nelson, "High-power THz generation, THz nonlinear optics, and THz nonlinear spectroscopy," *IEEE Journal of Selected Topics in Quantum Electronics*, vol. 14, no. 2, pp. 345–353, 2008.

[107] H. Y. Hwang *et al.*, "A review of non-linear terahertz spectroscopy with ultrashort tabletop-laser pulses," *Journal of Modern Optics*, vol. 62, no. 18, pp. 1447–1479, 2015.

[108] J. Lu, X. Li, Y. Zhang, H. Y. Hwang, B. K. Ofori-Okai, and K. A. Nelson, "Two-dimensional spectroscopy at terahertz frequencies," *Multidimensional Time-Resolved Spectroscopy*, pp. 275–320, 2019.

[109] T. Elsaesser, K. Reimann, and M. Woerner, *Concepts and Applications of Nonlinear Terahertz Spectroscopy*. New York, NY: Morgan & Claypool Publishers, 2019.

[110] F. X. Kärtner, "Terahertz accelerator based electron and x-ray sources," *Terahertz Science and Technology*, vol. 13, no. 1, pp. 22–31, 2020.

[111] S.-W. Huang, E. Granados, W. R. Huang, K.-H. Hong, L. E. Zapata, and F. X. Kärtner, "High conversion efficiency, high energy terahertz pulses by optical rectification in cryogenically cooled lithium niobate," *Optics Letters*, vol. 38, no. 5, pp. 796–798, 2013.

[112] W. R. Huang *et al.*, "Highly efficient terahertz pulse generation by optical rectification in stoichiometric and cryo-cooled congruent lithium niobate," *Journal of Modern Optics*, vol. 62, no. 18, pp. 1486–1493, 2015.

[113] J. A. Fülöp *et al.*, "Efficient generation of THz pulses with 0.4 mJ energy," *Optics Express*, vol. 22, no. 17, pp. 20 155–20 163, 2014.

[114] K. Ravi *et al.*, "Theory of terahertz generation by optical rectification using tilted-pulse-fronts," *Optics express*, vol. 23, no. 4, pp. 5253–5276, 2015.

[115] K. Ravi, W. R. Huang, S. Carbajo, X. Wu, and F. Kärtner, "Limitations to THz generation by optical rectification using tilted pulse fronts," *Optics Express*, vol. 22, no. 17, pp. 20 239–20 251, 2014.

[116] K. Ravi, B. K. Ofori-Okai, K. A. Nelson, and F. X. Kärtner, "Analysis of terahertz generation by beamlet superposition," *Optics Express*, vol. 27, no. 19, pp. 26 547–26 568, 2019.

[117] L Pálfalvi, J. Fülöp, G Almási, and J Hebling, "Novel setups for extremely high power single-cycle terahertz pulse generation by optical rectification," *Applied Physics Letters*, vol. 92, no. 17, 2008.

[118] M. Tsubouchi, K. Nagashima, F. Yoshida, Y. Ochi, and M. Maruyama, "Contact grating device with Fabry–Perot resonator for effective terahertz light generation," *Optics Letters*, vol. 39, no. 18, pp. 5439–5442, 2014.

[119] Y Avetisyan, A Makaryan, V Tadevosyan, and M Tonouchi, "Design of a multi-step phase mask for high-energy terahertz pulse generation by optical rectification," *Journal of Infrared, Millimeter, and Terahertz Waves*, vol. 38, pp. 1439–1447, 2017.

[120] L. Pálfalvi *et al.*, "Numerical investigation of a scalable setup for efficient terahertz generation using a segmented tilted-pulse-front excitation," *Optics Express*, vol. 25, no. 24, pp. 29 560–29 573, 2017.

[121] P. S. Nugraha *et al.*, "Demonstration of a tilted-pulse-front pumped plane-parallel slab terahertz source," *Optics Letters*, vol. 44, no. 4, pp. 1023–1026, 2019.

[122] M. C. Hoffmann, K.-L. Yeh, J. Hebling, and K. A. Nelson, "Efficient terahertz generation by optical rectification at 1035 nm," *Optics Express*, vol. 15, no. 18, pp. 11 706–11 713, 2007.

[123] L Guiramand, J. Nkeck, X Ropagnol, T Ozaki, and F Blanchard, "Near-optimal intense and powerful terahertz source by optical rectification in lithium niobate crystal," *Photonics Research*, vol. 10, no. 2, pp. 340–346, 2022.

[124] F. G. Back and H. Lowen, "The basic theory of varifocal lenses with linear movement and optical compensation," *Journal of the Optical Society of America*, vol. 44, no. 9, pp. 684–691, 1954.

[125] A. F. Oskooi, D. Roundy, M. Ibanescu, P. Bermel, J. D. Joannopoulos, and S. G. Johnson, "MEEP: a flexible free-software package for electromagnetic simulations by the FDTD method," *Computer Physics Communications*, vol. 181, no. 3, pp. 687–702, 2010.

[126] A. Buzády *et al.*, "Refractive index and absorption coefficient of undoped and Mg-doped lithium tantalate in the terahertz range," *Journal of Infrared, Millimeter, and Terahertz Waves*, vol. 38, pp. 963–971, 2017.

[127] A. Bruner, D. Eger, M. B. Oron, P. Blau, M. Katz, and S. Ruschin, "Temperature-dependent Sellmeier equation for the refractive index of stoichiometric lithium tantalate," *Optics Letters*, vol. 28, no. 3, pp. 194–196, 2003.

[128] M. C. Hoffmann and J. A. Fülöp, "Intense ultrashort terahertz pulses: Generation and applications," *Journal of Physics D: Applied Physics*, vol. 44, no. 8, p. 083 001, 2011.

[129] S. B. Bodrov, A. A. Murzanev, Y. A. Sergeev, Y. A. Malkov, and A. N. Stepanov, "Terahertz generation by tilted-front laser pulses in weakly and strongly nonlinear regimes," *Applied Physics Letters*, vol. 103, no. 25, p. 251 103, 2013.

[130] X. Wu *et al.*, "Terahertz generation in lithium niobate driven by Ti:sapphire laser pulses and its limitations," *Optics Letters*, vol. 39, no. 18, pp. 5403–5406, 2014.

[131] D Ashkenasi, M Lorenz, R Stoian, and A Rosenfeld, "Surface damage threshold and structuring of dielectrics using femtosecond laser pulses: The role of incubation," *Applied Surface Science*, vol. 150, no. 1-4, pp. 101–106, 1999.

[132] D. Bryan, R. Gerson, and H. Tomaschke, "Increased optical damage resistance in lithium niobate," *Applied Physics Letters*, vol. 44, no. 9, pp. 847–849, 1984.

[133] P Peier, H Merbold, V Pahinin, K. A. Nelson, and T Feurer, "Imaging of THz waves in 2D photonic crystal structures embedded in a slab waveguide," *New Journal of Physics*, vol. 12, no. 1, p. 013 014, 2010.

[134] D. W. Ward, J. D. Beers, T Feurer, E. R. Statz, N. S. Stoyanov, and K. A. Nelson, "Coherent control of phonon-polaritons in a terahertz resonator fabricated with femtosecond laser machining," *Optics Letters*, vol. 29, no. 22, pp. 2671–2673, 2004.

[135] V. R. Almeida, Q. Xu, C. A. Barrios, and M. Lipson, "Guiding and confining light in void nanostructure," *Optics Letters*, vol. 29, no. 11, pp. 1209–1211, 2004.

[136] Q. Xu, V. R. Almeida, R. R. Panepucci, and M. Lipson, "Experimental demonstration of guiding and confining light in nanometer-size low-refractive-index material," *Optics Letters*, vol. 29, no. 14, pp. 1626–1628, 2004.

[137] D. Wood, J. Remeika, and E. Kolb, "Optical spectra of rare-earth orthoferrites," *Journal of Applied Physics*, vol. 41, no. 13, pp. 5315–5322, 1970.

[138] S. Saito, T. M. Inerbaev, H. Mizuseki, N. Igarashi, R. Note, and Y. Kawazoe, "First principles calculation of terahertz vibrational modes of a disaccharide monohydrate crystal of lactose," *Japanese Journal of Applied Physics*, vol. 45, no. 11L, p. L1156, 2006.

[139] D. Allis, A. Fedor, T. Korter, J. Bjarnason, and E. Brown, "Assignment of the lowest-lying THz absorption signatures in biotin and lactose monohydrate by solid-state density functional theory," *Chemical Physics Letters*, vol. 440, no. 4-6, pp. 203–209, 2007.

[140] R. Peretti *et al.*, "THz-TDS time-trace analysis for the extraction of material and metamaterial parameters," *IEEE Transactions on Terahertz Science and Technology*, vol. 9, no. 2, pp. 136–149, 2018.

[141] W.-C. Lai, S. Chakravarty, X. Wang, C. Lin, and R. T. Chen, "On-chip methane sensing by near-IR absorption signatures in a photonic crystal slot waveguide," *Optics Letters*, vol. 36, no. 6, pp. 984–986, 2011.

[142] Z.-F. Wu *et al.*, "Investigation of a slow-light enhanced near-infrared absorption spectroscopic gas sensor, based on hollow-core photonic band-gap fiber," *Sensors*, vol. 18, no. 7, p. 2192, 2018.

[143] L. Tombez, E. J. Zhang, J. S. Orcutt, S. Kamlapurkar, and W. M. Green, "Methane absorption spectroscopy on a silicon photonic chip," *Optica*, vol. 4, no. 11, pp. 1322–1325, 2017.

[144] R. Singh, W. Cao, I. Al-Naib, L. Cong, W. Withayachumnankul, and W. Zhang, "Ultrasensitive terahertz sensing with high-Q Fano resonances in meta-surfaces," *Applied Physics Letters*, vol. 105, no. 17, 2014.

[145] D.-K. Lee *et al.*, "Highly sensitive and selective sugar detection by terahertz nano-antennas," *Scientific Reports*, vol. 5, no. 1, p. 15 459, 2015.

[146] B. Han, Z. Han, J. Qin, Y. Wang, and Z. Zhao, "A sensitive and selective terahertz sensor for the fingerprint detection of lactose," *Talanta*, vol. 192, pp. 1–5, 2019.

[147] M. Cornet, J. Degert, E. Abraham, and E. Freysz, "Terahertz-field-induced second harmonic generation through Pockels effect in zinc telluride crystal," *Optics Letters*, vol. 39, no. 20, pp. 5921–5924, 2014.

[148] J. Chen, P. Han, and X.-C. Zhang, "Terahertz-field-induced second-harmonic generation in a beta barium borate crystal and its application in terahertz detection," *Applied Physics Letters*, vol. 95, no. 1, 2009.

[149] T. G. Pedersen, "Exciton stark shift and electroabsorption in monolayer transition-metal dichalcogenides," *Physical Review B*, vol. 94, no. 12, p. 125 424, 2016.